2014

Indirect and direct methods for measuring a dynamic throat diameter in a solid rocket motor

Lauren Colbaugh

INDIRECT AND DIRECT METHODS FOR MEASURING A DYNAMIC THROAT DIAMETER IN A SOLID ROCKET MOTOR

by

LAUREN COLBAUGH

A THESIS

Submitted in partial fulfillment of the requirements
for the degree of Master of Science in Engineering
in
The Department of Mechanical and Aerospace Engineering
to
The School of Graduate Studies
of
The University of Alabama in Huntsville

HUNTSVILLE, ALABAMA

2014

In presenting this thesis in partial fulfillment of the requirements for a master's degree from The University of Alabama in Huntsville, I agree that the Library of this University shall make it freely available for inspection. I further agree that permission for extensive copying for scholarly purposes may be granted by my advisor or, in his/her absence, by the Chair of the Department or the Dean of the School of Graduate Studies. It is also understood that due recognition shall be given to me and to The University of Alabama in Huntsville in any scholarly use which may be made of any material in this thesis.

Lauren Calbaugh 12/10/14

(student signature) (date)

THESIS APPROVAL FORM

Submitted by Lauren Colbaugh in partial fulfillment of the requirement for the degree of Master of Science in Mechanical Engineering and accepted on behalf of the Faculty of the School of Graduate Studies by the thesis committee.

We, the undersigned members of the Graduate Faculty of The University of Alabama in Huntsville, certify that we have advised and/or supervised the candidate on the work described in this thesis. We further certify that we have reviewed the thesis manuscript and approve it in partial fulfillment of the requirements for the degree of Master of Science in Mechanical Engineering.

Robert A Frederick 3/10/14 Committee Chair
(Date)

12/3/14

12/3/14

Department Chair

College Dean

Graduate Dean

ABSTRACT
The School of Graduate Studies
The University of Alabama in Huntsville

Degree Master of Science in Engineering College/Dept. Mechanical and Aerospace Engineering.

Name of Candidate Lauren Colbaugh
Title Indirect and Direct Methods for Measuring a Dynamic Throat Diameter in a Solid Rocket Motor.

In a solid rocket motor, nozzle throat erosion is dictated by propellant composition, throat material properties, and operating conditions. Throat erosion has a significant effect on motor performance, so it must be accurately characterized to produce a good motor design. In order to correlate throat erosion rate to other parameters, it is first necessary to know what the throat diameter is throughout a motor burn. Thus, an indirect method and a direct method for determining throat diameter in a solid rocket motor are investigated in this thesis. The indirect method looks at the use of pressure and thrust data to solve for throat diameter as a function of time. The indirect method's proof of concept was shown by the good agreement between the ballistics model and the test data from a static motor firing. The ballistics model was within 10% of all measured and calculated performance parameters (e.g. average pressure, specific impulse, maximum thrust, etc.) for tests with throat erosion and within 6% of all measured and calculated performance parameters for tests without throat erosion. The direct method involves the use of x-rays to directly observe a simulated nozzle throat erode in a dynamic environment; this is achieved with a dynamic calibration standard. An image processing algorithm is developed for extracting the diameter dimensions from the x-ray intensity digital images. Static and dynamic tests were conducted. The measured diameter was compared to the known diameter in the calibration standard. All dynamic test results were within +6% / -7% of the actual diameter. Part of the edge detection method consists of dividing the entire x-ray image by an average pixel value, calculated from a set of pixels in the x-ray image. It was found that the accuracy of the edge detection method depends upon the selection of the average pixel value area and subsequently the average pixel value. An average pixel value sensitivity analysis is presented. Both the indirect method and the direct method prove to be viable approaches to determining throat diameter during solid rocket motor operation.

Abstract Approval: Committee Chair
Department Chair
Graduate Dean

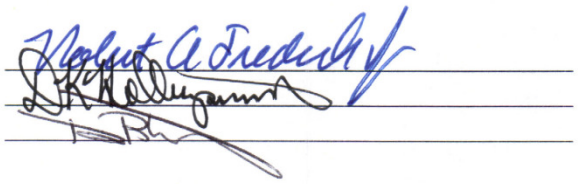

ACKNOWLEDGMENT

I would like to thank Dr. Frederick for serving as my advisor and Dr. Nelson and Dr. Frendi for serving on my committee. Thank you to Dan Jones for providing several semesters worth of test data and thank you to Matthew Denny and Joe Buckley for helping me collect x-ray data. Thank you to Mark Wells for drawing up and machining the calibration standard for me. Thank you to my mom and dad who encouraged me to pursue this endeavor. And thank you to John Colbaugh, who I met along the way.

TABLE OF CONTENTS

PAGE

LIST OF FIGURES

FIGURE PAGE

LIST OF TABLES

TABLE PAGE

LIST OF SYMBOLS

a_0	temperature coefficient (in/s)(psia)$^{-n}$
A_b	propellant surface area (in^2)
A_e	exit area (in^2)
A_t	throat area (in^2)
c^*	characteristic velocity (ft/s)
c_f	thrust coefficient
D_e	exit diameter (in)
D_{ID}	propellant grain inside diameter (in)
D_{OD}	propellant grain outside diameter (in)
D_t	throat diameter (in)
F	thrust (lbf)
F_{actual}	measured thrust (lbf)
F_{calc}	calculated thrust (lbf)
I	intensity at the detector (kV)
I_0	intensity at the source (kV)
k	ratio of specific heats
$\dot{m}_n$	mass flow rate at nozzle throat (lbm/s)
$\dot{m}_p$	mass flow rate into motor (lbm/s)
M	magnification
M.F.	magnification factor
M_2	exit Mach number

n	burning rate coefficient
P_c	chamber pressure (psia)
P_2	exit pressure (psia)
P_3	ambient pressure (psia)
$\dot{r}$	propellant burn rate (in/s)
$\dot{r}_{throat}$	throat erosion rate (in/s)
SDD	source-to-detector distance (in)
SOD	source-to-object distance (in)
T_b	propellant temperature (^{o}F)
T_{0b}	propellant reference temperature (^{o}F)
x	linear distance (in)
ε	nozzle area ratio
ε_{calc}	calculated nozzle area ratio
ε_{guess}	guessed nozzle area ratio
μ	linear attenuation coefficient (1/in)
ρ_p	propellant density (lbm/ft^3)
σ_p	temperature sensitivity coefficient (1/^{o}F)

CHAPTER 1

Introduction

1.1 Nature and Scope of Problem

Solid rocket motor chamber pressure and thrust depends strongly on the nozzle throat area. High heat loads necessitate using ablative materials for the nozzle throat. This study compares an indirect and a direct method of continuously determining nozzle throat area change during the static operation of a solid rocket motor. The indirect method uses chamber pressure and thrust measurements of a static motor firing to calculate throat diameter. The direct method uses real-time x-ray radiography to measure the throat diameter of a dynamic calibration standard during a simulated static test fire with throat erosion.

There are several ways to determine if throat erosion has occurred in a solid rocket motor. The first is simply to measure the throat before and after test to see if the throat diameter changed. The second way requires both chamber pressure and thrust to be measured during the test. The thrust divided by the chamber pressure is proportional to the nozzle throat area. Plotting thrust divided by chamber pressure yields either a sloped trace or a relatively flat trace. A sloped trace is an indication that throat erosion occurred while a relatively flat trace is an indication that it did not. Figure 1-1 shows the test results from

two G138 solid rocket motor tests, one with throat erosion (left) and one without (right). Notice that during steady state, the thrust over pressure plot increases linearly for the case with throat erosion. Thrust over pressure behavior during transient start-up and shut-down can be ignored.

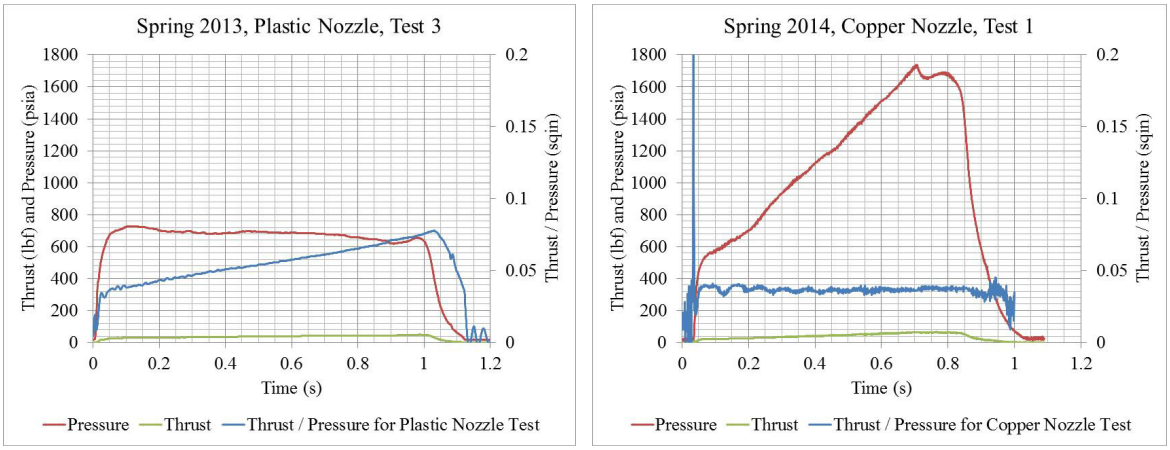

Figure 1-1 G138 Tests with Throat Erosion (Left); without Throat Erosion (Right)

1.2 Literature Review – Throat Erosion

1.2.1 Ballistics Basics

This subsection familiarizes the reader with the equations in a ballistics model and how a model is correlated to test data. The ballistics model is a tool used in the development of a solid rocket motor. During preliminary analysis, a ballistics model typically assumes no throat erosion. For the purposes of this subsection, the same assumption is made.

A ballistics model takes a set of inputs, performs multiple calculations, and then outputs chamber pressure and thrust as a function of time. After a ballistics model is developed, it should be correlated and anchored to test data. An anchored model can then be used to make new pressure and thrust predictions by changing model inputs.

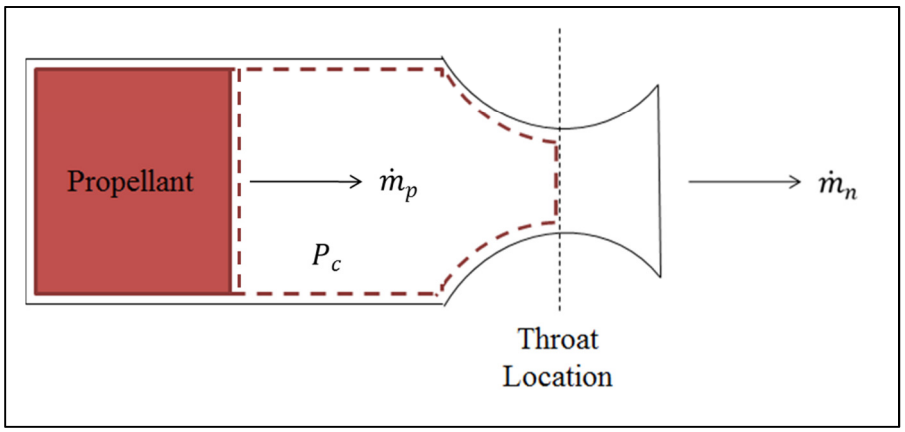

Figure 1-2 Mass Flow Balance in a Solid Rocket Motor

For steady state operation, the mass flow of the propellant into the motor is given by:

$$\dot{m}_p = \rho_p A_b \dot{r} \tag{1-1}$$

The mass flow is balanced with the mass flow rate at the nozzle throat, given by:

$$\dot{m}_n = \frac{P_c A_t}{c^*} \tag{1-2}$$

Equating Equation (1-1) to Equation (1-2) and using a modified form of St. Roberts' Law to describe the propellant burn rate:

$$\dot{r} = P_c^n a_0 e^{\sigma_p (T_b - T_{0b})} \tag{1-3}$$

Yields the steady state chamber pressure:

$$P_c = \left[\rho_p a_0 e^{\sigma_p (T_b - T_{0b})} c^* \frac{A_b}{A_t}\right]^{\frac{1}{1-n}} \quad \textbf{(1-4)}$$

The derivation of Equation (1-3) from St. Robert's Law is provided in Appendix A.

The influence of throat area on chamber pressure is evident in this equation. For a given value of n and assuming all other variables on the right-hand-side are known (which is a good assumption), one can see the impact of throat area on chamber pressure in Figure 1-3. For example, for n equal to 0.25, a 10% increase in throat area results in a 12% decrease in chamber pressure. This cannot be ignored or considered negligible. It is therefore important for the analyst to include throat erosion in a high-fidelity ballistics model.

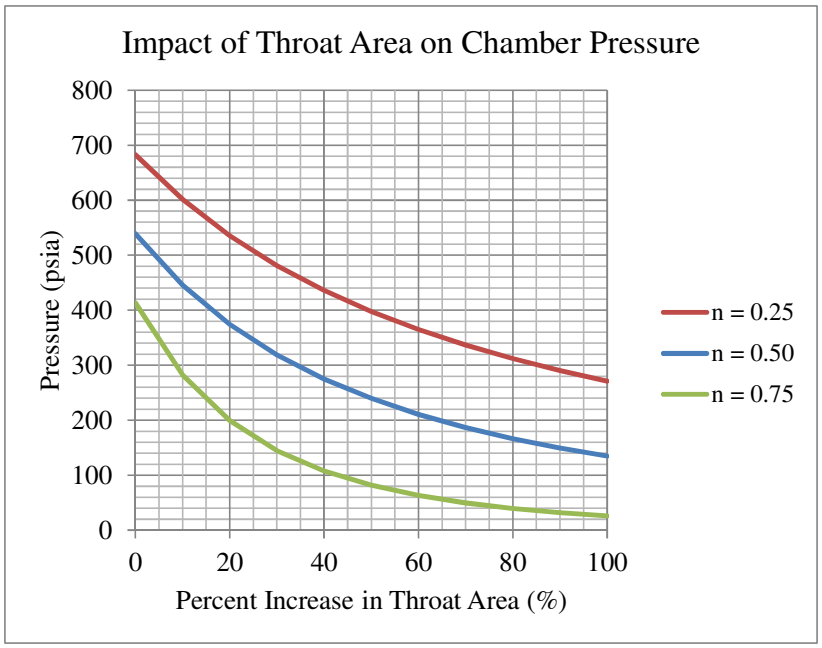

Figure 1-3 Impact of Throat Area on Chamber Pressure

During preliminary analysis, all of the variables in Equation (1-4) are assumed constant or known. This includes the throat area (A_t). A relationship between web and propellant surface area is developed in Appendix B. For the purposes of this ballistics model, an empirically-derived web versus surface area relationship is used.

Within the ballistics model, thrust is calculated as:

$$\boldsymbol{F = P_c A_t c_f} \tag{1-5}$$

To show that thrust divided by chamber pressure is proportional to throat area, Equation (1-5) is rearranged into this form:

$$\frac{F}{P_c}\left(\frac{1}{c_f}\right) = A_t \tag{1-6}$$

The thrust coefficient is a calculated value and an important part of the throat erosion analysis, discussed further in Section 2.2. It is a function of the ratio of specific heats, the pressure ratio, and the area ratio:

$$c_f = f(k, P_c/P_3, \varepsilon) \tag{1-7}$$

The area ratio (ε) is the nozzle exit area divided by the throat area:

$$\varepsilon = \frac{A_e}{A_t} \tag{1-8}$$

It is clear from Equation (1-8) that throat erosion - which causes a change in throat area - will cause a change in the area ratio as well. Like the chamber pressure equation, Equation (1-5) shows another important performance parameter's dependence on throat area. Again, throat area is sometimes considered constant in the thrust equation during preliminary analysis; once throat erosion is incorporated, the throat area is updated at each time step in the model. A ballistics model is only useful if it is correlated to test data (that is, the model generates pressure and thrust curves similar to test data, given the same input parameters).

1.2.2 Papers about Throat Erosion

It is clear from Figure 1-3 that throat erosion significantly influences motor performance. There is extensive literature about what causes throat erosion in a solid rocket motor. There is a consensus that multiple factors contribute to throat erosion. The most prominent factors are propellant composition, throat material properties, and chamber pressure.

Klager [1] observed a correlation between throat erosion rate (of a graphite throat) and the mass fractions of the oxidizing combustion products with aluminized solid propellants. Propellants with larger quantities of water and carbon dioxide in the combustion gases had higher throat erosion rates. Klager provides correlations between 1) rate of throat area change and mole fractions of oxidants, 2) rate of throat area change and mole fractions of just water, 3) rate of throat area change and oxygen balance (a term the author adopted to describe any remaining oxygen after theoretical complete combustion), 4) rate of throat area change and oxygen balance ratio, and finally 5) available oxygen and rate of corrosion.

All correlations are linear and proportional. The best-fit correlation from Klager's work is shown in Figure 1-4. The data labels indicate different propellant compositions that the author tested. Because the mass fractions of all of the combustion products depend on the propellant composition, Klager, Thakre [2], Evans [3], and others agree that throat erosion rate is a function of propellant composition. Figure 1-4 is from Klager's work; it

clearly shows that propellant compositions that leave more oxygen available after combustion results in higher throat erosion rates.

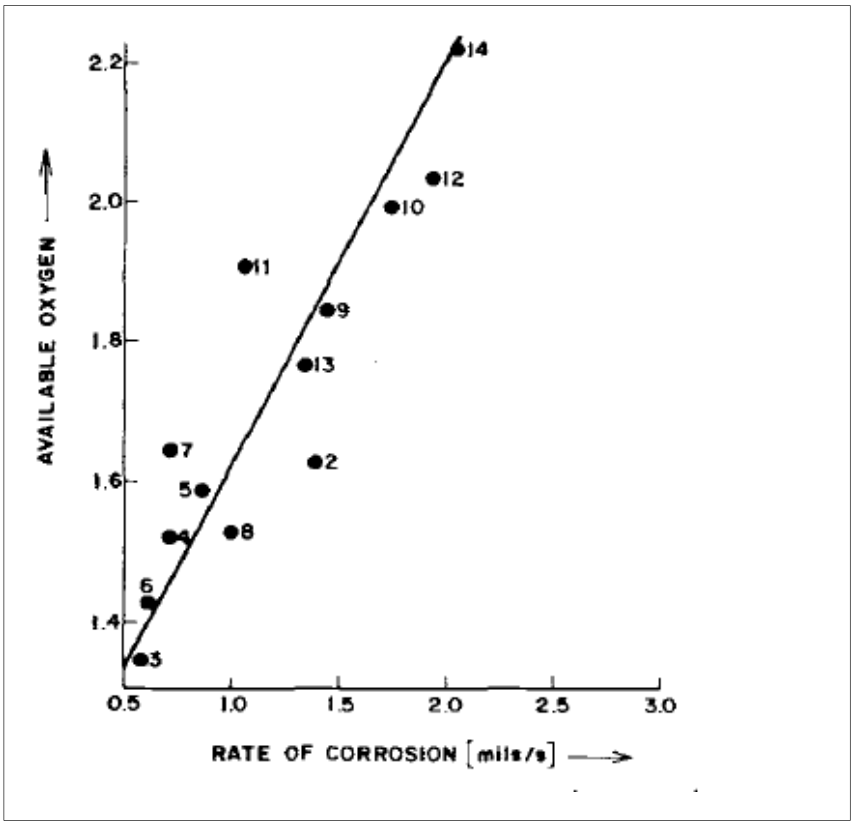

Figure 1-4 Average Linear Rate of Corrosion with Increasing Available Oxygen

Throat erosion rate also depends on how well the throat material resists erosion. A common throat material is carbon-carbon composite or graphite material. Graphite has low density, high strength, good thermal stability, low thermal conductivity, and low ablation rate [4]. All of these factors make graphite a good candidate for a solid rocket motor throat material. There is extensive literature on graphite performance in solid rocket motor applications, such as [5]. Klager observed that, with all other factors the

same, a denser graphite throat resisted erosion better than a less dense graphite throat. The time-pressure trace in Figure 1-5, from Klager's work, illustrates this correlation.

Notice that the pressure in the motor with the ATJ graphite nozzle decreased faster than the motor with the ZT graphite nozzle. The steeper decline is an indication that the less dense ATJ throat erodes faster – or has a higher throat erosion rate – than the denser ZT throat. The throat diameter in the ATJ motor increases faster, resulting in lower chamber pressure and longer burn duration.

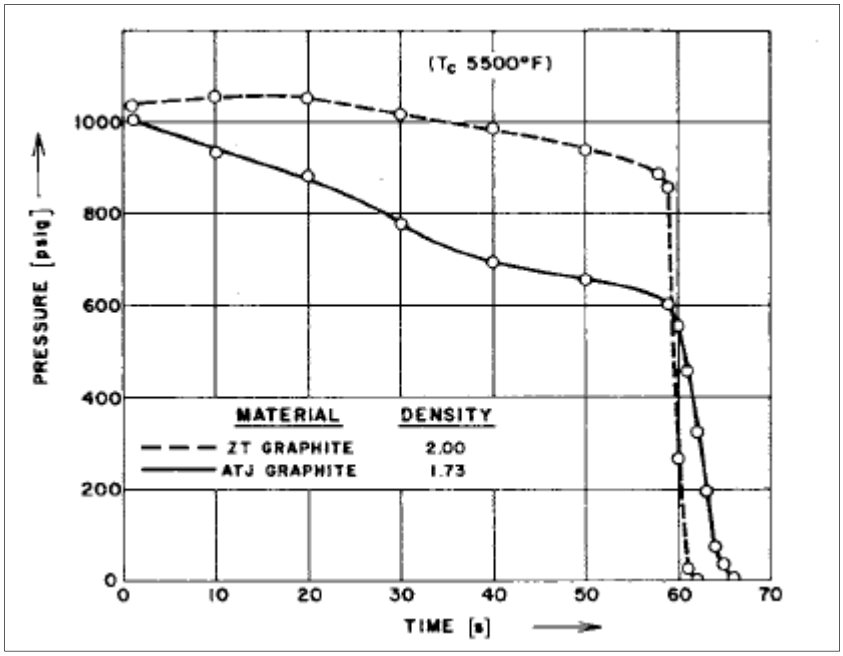

Figure 1-5 Compare Throat Erosion Rate of Graphite with Varying Density

Finally there is chamber pressure. Throughout the literature review, it became apparent that there exists a strong function between erosion rate and chamber pressure and that throat erosion rate increases with chamber pressure [3,6]. Evans [3] provides an empirically-derived equation for throat erosion rate as a function of chamber pressure

alone for a graphite nozzle, shown in Figure 1-6. Target chamber pressures were 500, 750, and 1,000 psia (3.45, 5.17, and 6.89 MPa) and initial throat diameter was 0.5 inch (1.27 cm). For reference, the G138 nominal operating pressure is about 700 psia with an initial throat diameter of 0.18 inch. Evans noted that the increase of erosion rate was solely due to the increase in heat transfer rates at higher pressure conditions.

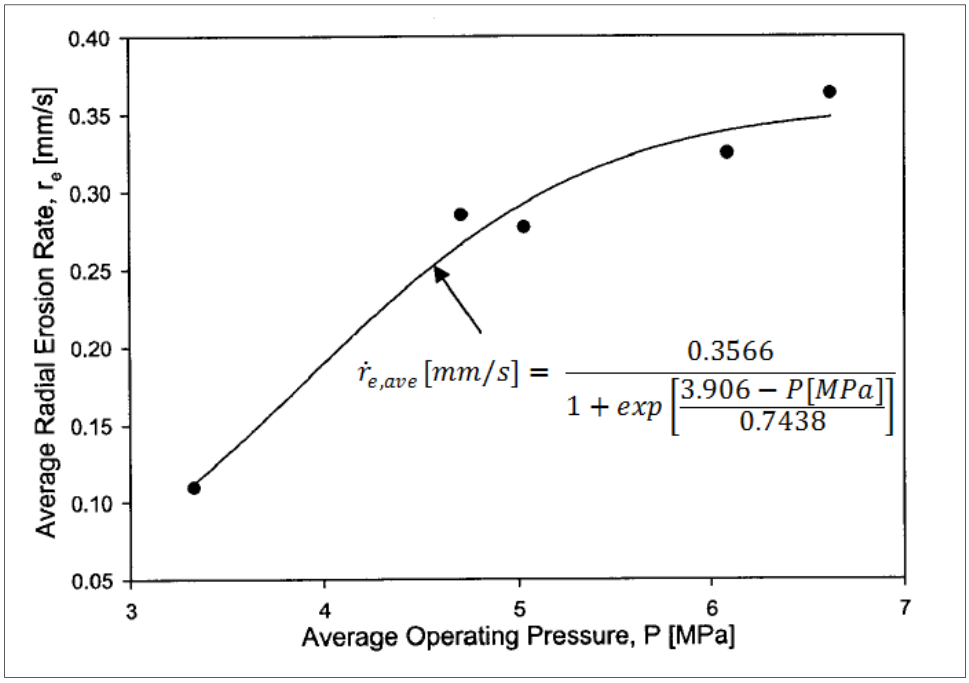

Figure 1-6 Correlation of Measured Average Erosion Rates with Chamber Pressure

In order to develop a throat erosion rate relationship, one must know the rate at which the throat area changes as a function of time and chamber pressure during motor operation. Part of the literature review included researching what others have done to determine throat diameter during motor operation. Klager [1] briefly mentioned an indirect method of using a computer program to determine throat area at regular intervals during a firing. No details were provided regarding how the computer program worked. Real-time

radiography is another method (a direct method) for determining throat diameter during motor operation. Literature that covered this topic is discussed in Section 1.3.2.

1.3 Literature Review – Real Time X-ray Radiography

Real-time x-ray radiography allows for the observation of internal surfaces and features as a function of time in a solid rocket motor. This section first familiarizes the reader with some x-ray basics gleaned from the literature review. Topics include components of a typical x-ray setup, how x-rays are produced, x-ray detectors, the Beer-Lambert Law, and x-ray magnification.

Following the x-ray basics, a literature review of the direct method is presented. Papers about the use of x-rays to observe changes in a solid rocket motor, specifically throat erosion, are discussed. The paper most relevant to the direct method is thoroughly reviewed.

1.3.1 X-ray Basics

Digital radiography is x-ray photography but without film. In place of film, a digital detector is used to capture and measure x-ray intensity. This intensity is stored digitally and allows for almost immediate viewing of the image. Five essential items are needed to take a digital radiograph: an x-ray generator (or source), an x-ray detector, a subject to scan, a computer to collect and store data, and an x-ray booth to operate safely. A typical setup of these components is shown in Figure 1-7. A more detailed discussion of the x-ray generator and detector is provided in the following two sections.

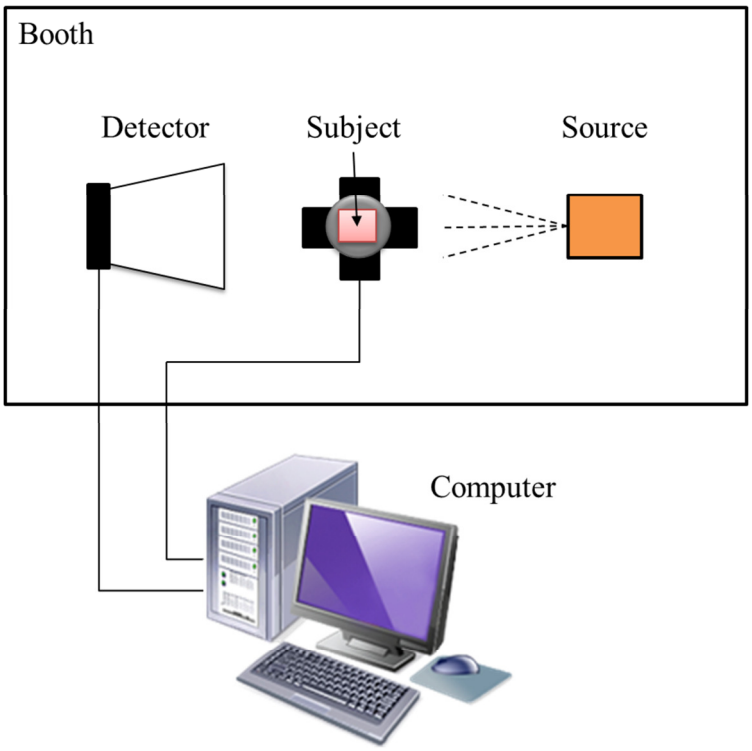

Figure 1-7 Typical X-ray Setup

X-ray Generator (Source)

The filament x-ray tube, which is the most common type used today, must have three things:

1) A source of electrons
2) A high accelerating voltage
3) A metal target.

In the case of a filament x-ray tube, shown in Figure 1-8 [7], the major components are a target (anode) and a heated filament (cathode) that emits electrons. A high potential is developed between the filament and the anode. Electrons leave the filament and

accelerate toward the anode. Upon striking the anode, the kinetic energy of the electron is converted into heat and x-rays. Most of the kinetic energy of the electrons striking the target is converted into heat; less than 1% is transformed into x-rays [8].

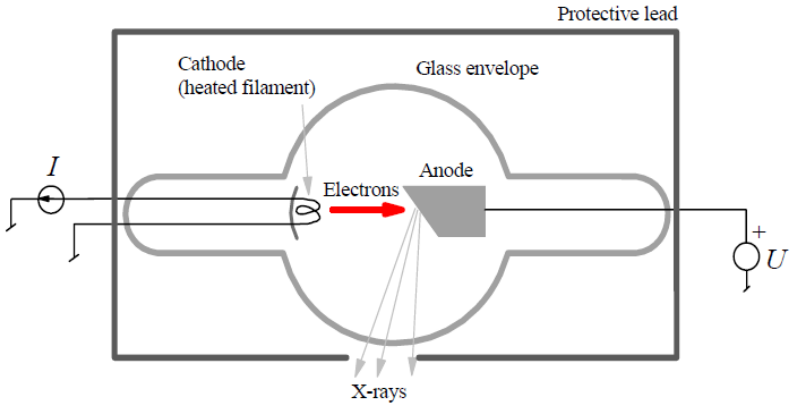

Figure 1-8 Filament X-ray Tube Schematic

It became apparent early in the literature review process that an x-ray system is often identified by its energy source, for example a 100 kilovolt (kV) system. Throughout the literature review, energies ranged from 150 kV (for medical, low dosage applications) to 15 MV (for large diameter solid rocket motors that require high penetrating energies).

X-ray Detector

The x-ray detector has evolved from film to today's more common flat panel detector. The flat panel detector (FPD) was the most common type of detector referenced in the literature. It is typically placed opposite of the x-ray generator, with the subject in between. A coating on the detector converts the incident X-ray photons to visible light with intensity proportional to that of the incident radiation. The captured digital image is divided into M x N pixels. In place of a FPD, a charge-coupled device (CCD) camera

mounted to the back of an image intensifier can also be used. The image intensifier converts the radiation to visible light and focuses the image onto the CCD camera lens.

Beer-Lambert Law

As an x-ray passes through a material the intensity of the beam is attenuated – or lessened – by some amount. A material's ability to attenuate is described by its linear attenuation coefficient (LAC), a value which is dependent on the material density and the initial x-ray intensity leaving the x-ray generator. For the purposes of creating an x-ray prediction, the LAC is simply found in a lookup table for the specified material. The relationship that describes the attenuation of a beam is given by the Beer-Lambert equation [9,10,11]:

$$\boldsymbol{I = I_0 exp\left[\sum_i (-\mu_i x_i)\right]} \qquad \textbf{(1-9)}$$

Where I_0 is the x-ray intensity leaving the x-ray generator, I is the x-ray intensity measured by the detector, μ is the LAC, and x is a linear distance over which the LAC is applied. Figure 1-9 illustrates each element of Equation (1-9) for a single x-ray beam that passes through an object with a circular cross-section. It is ultimately Equation (1-9) that is used to model the x-ray intensity distribution that arrives at each pixel on the x-ray detector.

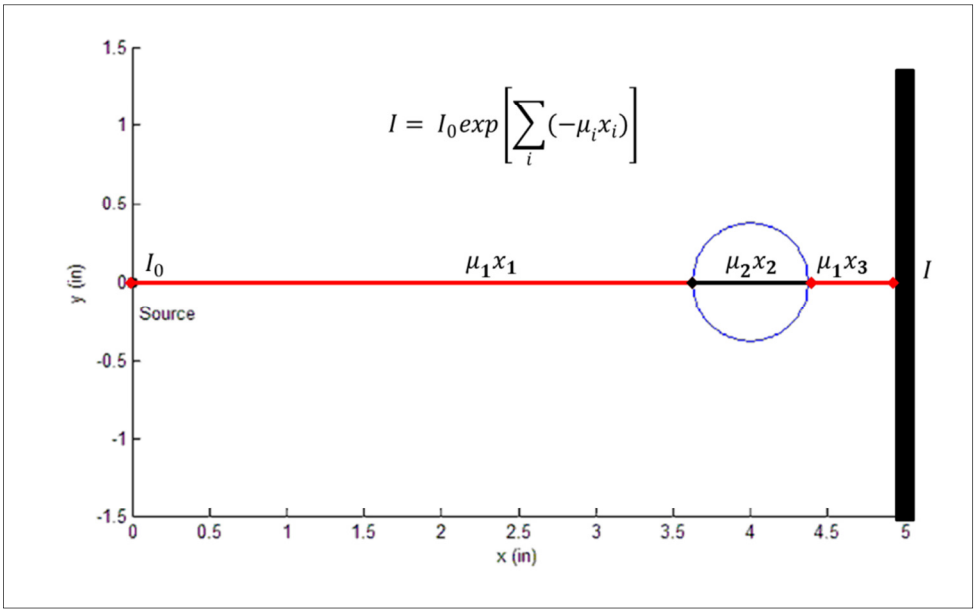

Figure 1-9 Illustration of Variables in Beer-Lambert Equation

X-ray Magnification

To accurately measure distances in an x-ray image, it is important to understand what x-ray magnification is and how it can influence results. The best way to describe x-ray magnification is with a picture, as shown in Figure 1-10. X-ray magnification occurs because the x-ray beam diverges from the x-ray source [12]. It is clear that a measurement taken from an x-ray image (In) must be corrected to obtain the desired measurement (Out).

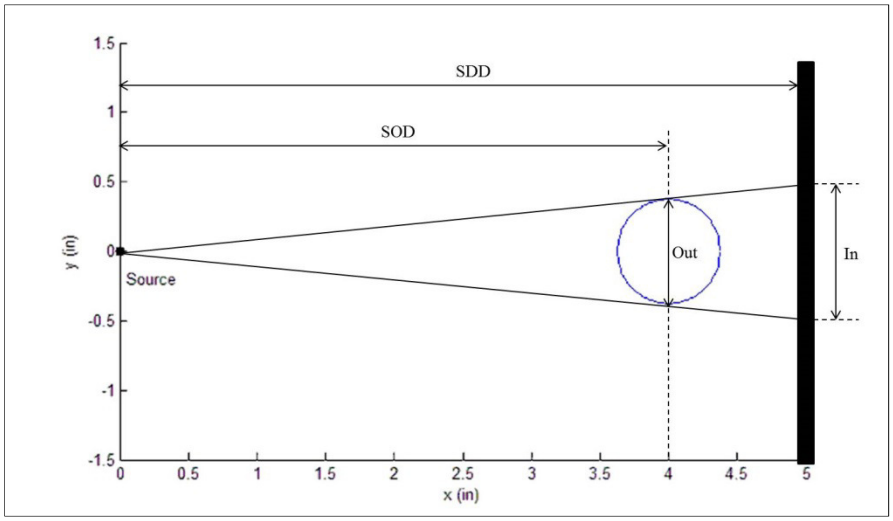

Figure 1-10 X-ray Magnification

Fortunately, the source-to-object (SOD) and the source-to-detector (SDD) distances are typically known. The concept of similar triangles is used to calculate the desired distance (Out). The following equation can be used to correct for magnification (M):

$$\boldsymbol{M = \frac{In}{Out} = \frac{SDD}{SOD}} \qquad \textbf{(1-10)}$$

Calibration marks or known features in an object can be used to calculate a magnification factor.

1.3.2 X-ray Papers about Throat Erosion

The literature review revealed multiple papers about the use of x-rays in solid rocket motor applications. The papers could be divided into two categories: papers about the use of x-rays in a static environment and papers about the use of x-rays in a dynamic environment. Static environments were typically for non-destructive evaluation of solid rocket motors – that is, x-rays were used to look for defects in solid propellant [13,14,15] or for de-bonds in the insulation-to-propellant interface [16,17].

The dynamic environments discussed in the papers focused on the propellant burn surface in the motor [18] or the propagation of a crack in the propellant [19] or the accumulation of slag near the nozzle [20,21].

There were two papers [3,22] about the use of x-rays to observe throat erosion in a solid rocket motor application – the most relevant papers to the current research topic. Both papers were written by the same primary authors (Brian Evans and Kenneth Kuo) about the same test setup. The objectives of Evans' and Kuo's research were to understand the processes that cause throat erosion and to develop a method to mitigate it. They used a 325 kV X-ray tube with a CCD camera/Image Intensifier system to capture images of the nozzle contour during solid rocket motor simulations and test fires. They were able to deduce instantaneous erosion rate with the x-ray data and correlate the erosion rate to pressure, mass fractions of oxidizing species, and other parameters. Figure 1-11 [22]

shows a pressure-time trace from the article, with the corresponding throat diameter of the G-90 graphite nozzle.

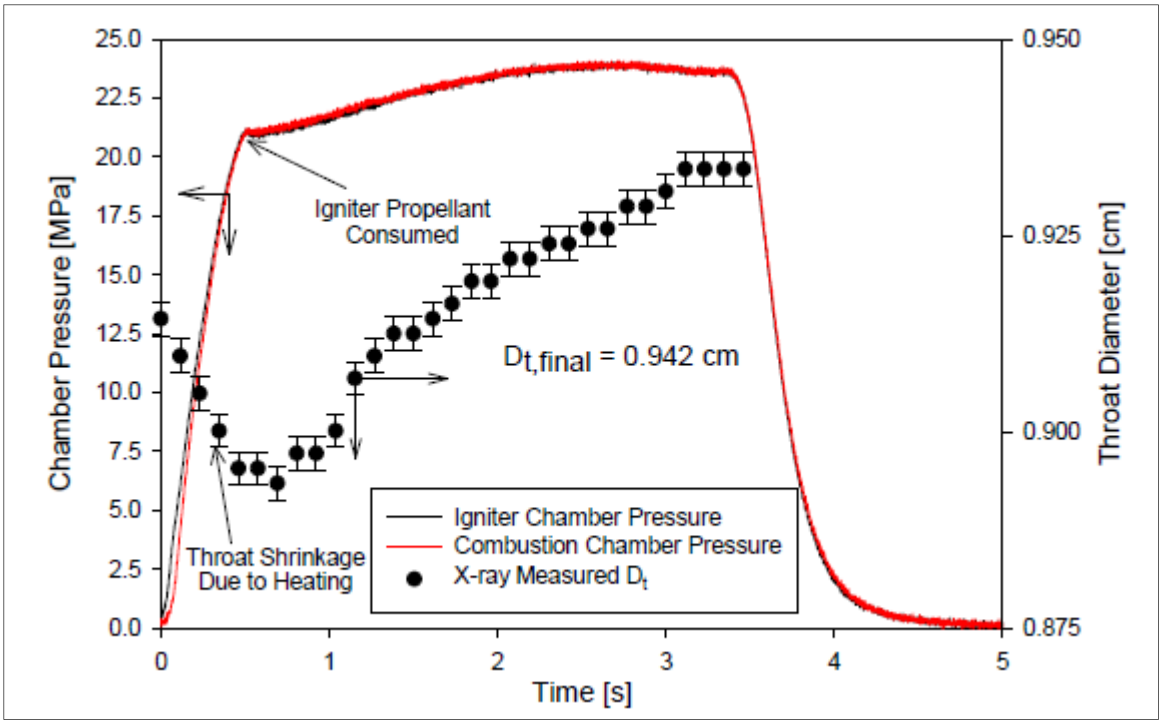

Figure 1-11 Pressure-Time Trace with Instantaneous Throat Diameter Measurements

An error bar is shown on each throat diameter measurement in Figure 1-11. Although the authors thoroughly explain their objectives, method of approach, and results, they do not discuss the error bars - how the bar magnitude was calculated or if the magnitude was arbitrarily selected. This is significant because the error bars indicate the accuracy of their method for measuring instantaneous throat diameter with x-ray imaging. They do not discuss their method for extracting dimensions from the x-ray images.

Another interesting feature in Figure 1-11is the initial dip in throat diameter (during the first second of burn). The authors talk about this feature in both of their reports [3, 22].

They explain that the rapid rise in chamber pressure induced rapid heating of the throat material, such that the throat actually contracted during ramp-up. Following the initial contraction, thermochemical erosion takes over and starts removing throat material until the end of burn.

The literature was also reviewed for methods in analyzing x-ray intensity data. The most relevant article looked at locating a burning propellant surface from simulated x-ray intensity data [23]. An x-ray of a solid propellant grain was first simulated using the Beer-Lambert Law, similar to Ravindran's method [24]. A minimum-value approach was used to locate the edge of the propellant surface in the intensity data. The authors explain that the inner edge of the bore is the longest ray path through the object and therefore coincides with the minimum intensity in the x-ray data. Figure 1-12 [23] illustrates the two minimum intensity locations (identified as m_1 and m_2). The number of pixels between m_1 and m_2 is calculated, multiplied by pixel height, and then multiplied by a magnification factor to determine the propellant surface location. The authors investigated two techniques for determining the pixel location of m_1 and m_2: computer edge detection and operator-selected edges. The computer method did not consistently locate the minimum values (due to the occurrences of sequential pixels at the minimum value), while the manual method located the propellant surface to within 1 pixel of the true position. This is equivalent to plus or minus 5 percent of the minimum radius measured. It is important to note that both methods described in the article used simulated x-ray data, which did not simulate noise.

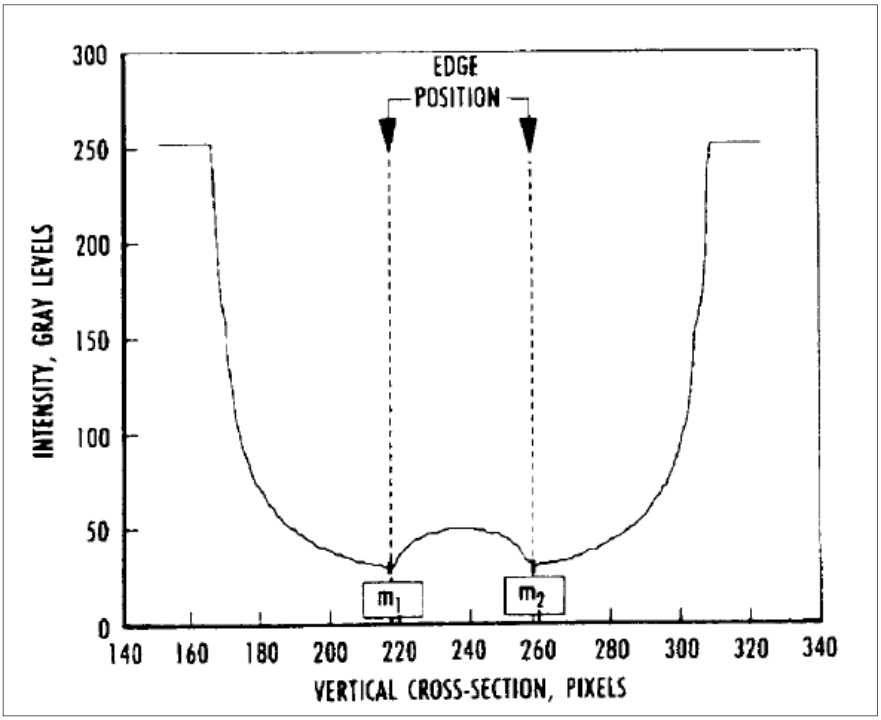

Figure 1-12 Minimum-Value Approach for Locating Propellant Surface

It is also worthwhile to mention that there was a paper that talked about measuring throat erosion rate with a means other than x-rays. Karthikeyan [25] investigated the use of ultrasound to measure throat erosion rate in a solid rocket motor.

1.4 Literature Assessment

Multiple factors influence throat erosion rate: propellant composition, throat material properties, and chamber pressure. Work has been done to correlate throat erosion rate to these factors. There are two ways to determine throat diameter as a function of time; the first way is to calculate it from test data, which can be considered an indirect way. Klager [1], for example, mentioned a computer program that determines throat area at regular intervals during a firing. Unfortunately, Klager not go into detail about how the

computer program works. The second way is to actually observe the throat in real-time and calculate the throat diameter from the x-ray image; this can be considered a direct method.

There is extensive literature on the use of x-rays with solid rocket motors in static and dynamic environments. X-ray setups have been very useful in nondestructive assessments of solid rocket motor manufacturing. X-ray setups have also been used to observe dynamic events such as propellant surfaces receding and propellant flaws propagating. Evans' and Kuo's work is most relevant to this thesis; they used real-time radiography to measure throat erosion in a solid rocket motor. They included error bands around their throat diameter measurements but did not explain how they were calculated. Evans and Kuo also provided insight into the initial contraction of the throat diameter that was observed during ramp-up.

Frederick [23] provided valuable insight into methods for determining edge location from x-ray intensity data. Undoubtedly, the focus in any future work should be on locating the pixel locations to the left and right of the small hump in the intensity data and correlating that value to an actual, known diameter. The authors acknowledge that noise in the x-ray intensity data would affect both edge detection methods.

1.5 Method of Investigation

Two methods for determining throat diameter are investigated – an indirect method and a direct method. The indirect method is discussed in the next chapter where a computer

program is developed that calculates throat diameter from a set of pressure and thrust data. Instantaneous chamber pressure and instantaneous throat erosion rate are plotted and a linear curve-fit is applied. This chamber pressure/erosion rate relationship is then incorporated into the ballistics model and validated with G138 sub-scale motor test data. It is important to note that the throat erosion equation that is developed in this thesis is a function of chamber pressure only:

$$\dot{r}_{throat} = f(P_c) \tag{1-11}$$

Propellant composition is not investigated in this thesis because these variables were held constant during G138 testing. Although throat material properties are not included in Equation (1-11), two throat materials are investigated in this thesis: the vendor-provided plastic nozzle and the UAH-supplied copper nozzle. Throat erosion was not observed in the copper nozzle test but is provided in the G138 test matrix because it proves useful for anchoring the model and validating the computer program. In the indirect method, throat diameter is always calculated to within some tolerance of the true diameter during motor operation.

The direct method uses real-time digital radiography to capture images of a Dynamic Calibration Standard that simulates throat erosion. Elements such as source-to-object distance, kV value, and erosion rate are varied in the test setup to determine if throat diameter measurement accuracy is affected.

1.6 Summary of Results

The result of the indirect method is a computer program that iteratively solves for throat diameter from a set of pressure and thrust data. This tool is very useful for developing empirically-derived throat erosion rate equations in the current and other solid rocket motor applications. The throat erosion rate equation developed in this thesis – which is a function of chamber pressure only – is limited due to the consistent operating pressure in the G138 test data. A stronger function could be developed if test data with a range of operating pressures was available. Nonetheless, the throat erosion rate equation developed in this thesis was incorporated into the ballistics model. Further confidence in the indirect method was gained when the same ballistics model showed good correlation to all of the G138 test data (i.e. for tests with and tests without throat erosion). Another validation of the indirect method is to actually observe a throat diameter changing in real-time. This realization led to an investigation of a direct method for determining throat diameter.

In the direct method, a process is developed for calibrating and extracting diameter dimensions from x-ray intensity data. Source-to-object distance, kV value, and diameter size were investigated. Factors that affect measurement accuracy are the magnification factor, average pixel value, and CCD camera frame rate, and table speed. The static magnification factor curve is useful for estimating dynamic magnification factors.

CHAPTER 2

Approach – Indirect Method

The purpose of this chapter is to develop and implement the indirect method for determining throat erosion rate. The indirect method requires pressure and thrust data from a static test fire. The UAH Propulsion Research Center has conducted multiple tests with the G138 hobby rocket motor. The test setup, motor, and test matrix are discussed. The analysis strategy determines throat diameter as a function of time from a set of pressure and thrust data. Throat erosion rate is found from the calculated throat diameter as a function of time. Following the analysis strategy, a linear chamber pressure/erosion equation is developed. This equation is incorporated into the ballistics model. With this pressure/erosion equation, the model shows good correlation to the test data.

2.1 Test Description

The test setup for the G138 motor is very simple. It is shown in Figure 2-1. The test setup consists of the G138 motor (discussed in the next section), a cradle to hold the motor, a Honeywell pressure transducer to measure chamber pressure, and a Sensotec load cell to measure thrust. The cradle, pressure transducer, and load cell are identified

as 1, 2, and 3 respectively in Figure 2-1 [26]. The pressure data, thrust data, and pre and post-test throat measurements from this test setup were used in Section 2.3.

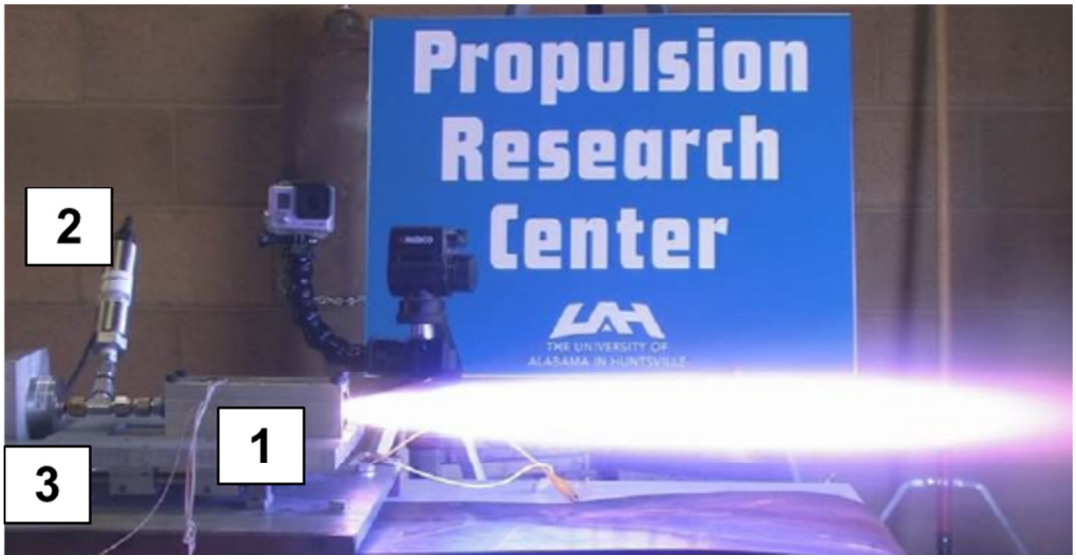

Figure 2-1 G138 Static Test Fire at UAH's Propulsion Research Center

2.1.1 G138 Motor

The G138 motor is an Aerotech hobby rocket motor that produces an average of 31 lbf of thrust. An exploded view of the motor is shown in Figure 2-2. This motor consists of a single, center-perforated solid fuel grain. The grain has an outside diameter of 0.95 inches, a bore diameter of 0.275 inches, and length of 3.902 inches. The forward closure is threaded into the aluminum motor case to contain the hot combustion gases during operation. The G138 motor is delivered with a plastic nozzle that has an initial throat diameter of 0.18 inches. Table 2-1 lists the G138 motor specifications [27], provided by the vendor.

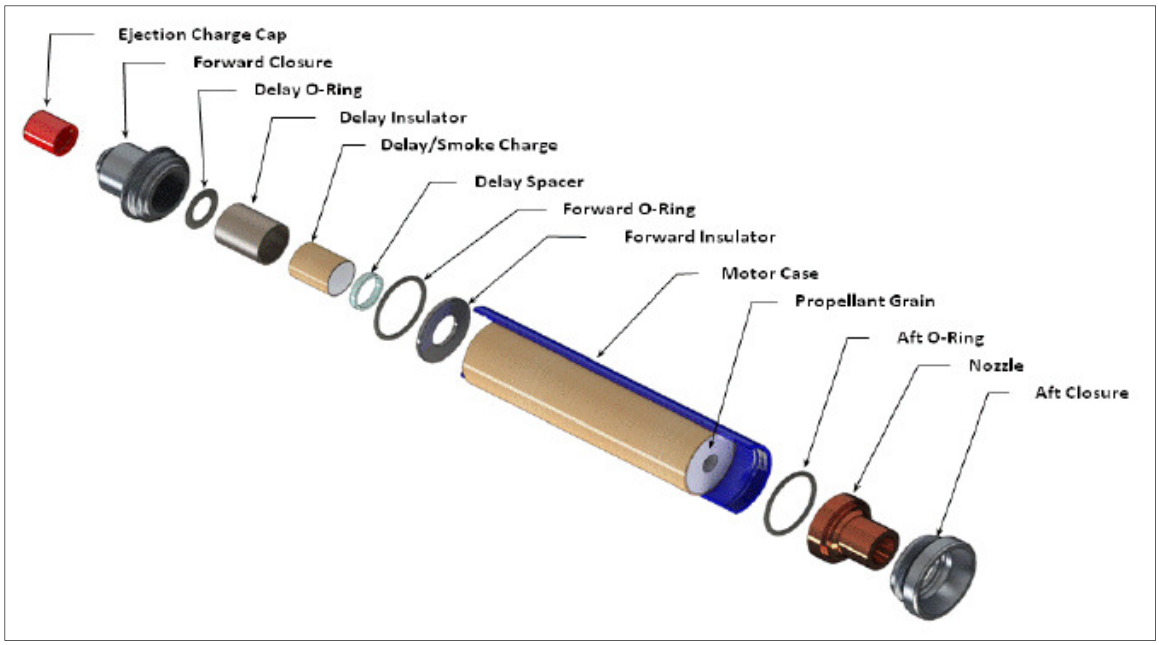

Figure 2-2 Exploded View of the G138 Hobby Rocket Motor

Table 2-1 G138 Motor Specifications

Motor Specification	Value	Units
Total Impulse	35	lbf-s
Propellant Mass	0.15	lbm
Loaded Mass	0.34	lbm
Motor Diameter	1.14	inch
Burn Time	1.1	s
Peak Thrust	43	lbf
Motor Length	4.875	inch
Delivered Specific Impulse	227.6	s

2.1.2 G138 Test Matrix

UAH testing has included static test fires at UAH's Propulsion Research Center and flight tests. The ballistics model was correlated to the four static tests shown in Table 2-2. Ballistics model correlation is discussed more in Section 2.3. A unique identifier for

each test is shown in the first column. The following discussions and figures refer to these identifiers.

Table 2-2 G138 Test Matrix

Test Identifier	Test Date	Nozzle Material	Pressure & Thrust Data Available?	Pre-Test Diameter	Post-Test Diameter
Spring 2013, Plastic	4/12/13	Plastic	Yes	0.18”	0.25”
Spring 2014, Plastic 1	3/14/14	Plastic	Yes	0.18”	0.25”
Spring 2014, Copper	3/26/14	Copper	Yes	0.18”	0.18”
Spring 2014, Plastic 2	4/11/14	Plastic	Yes	0.18”	0.25”

Pressure and thrust data are available for all four tests; this is important because these data are needed for the indirect method. Notice that the Spring 2014 Copper test did not have throat erosion. In fact, this test was conducted so that motor performance with a relatively constant throat diameter could be analyzed. The UAH students used a copper nozzle that was dimensionally identical to the plastic nozzle. The difference between tests with and tests without throat erosion (that is, tests with plastic nozzles and tests with copper nozzles, respectively) is shown in Figure 2-3. Thrust divided by pressure is plotted for each test in the G138 Test Matrix. Notice the flat trace for the copper nozzle test.

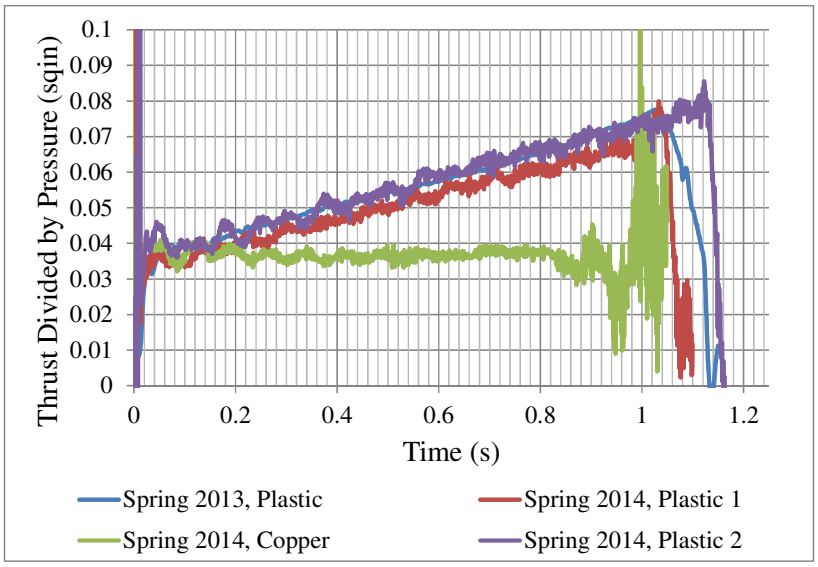

Figure 2-3 Thrust Divided by Pressure for Four G138 Tests

2.2 Analysis Strategy

A function was written in Matlab that takes in six inputs and outputs a single value. The six inputs are chamber pressure, its corresponding thrust value, ratio of specific heats, area ratio guess, exit diameter, and ambient pressure. The function takes these inputs, performs multiple calculations (some are iterative), and outputs a calculated area ratio:

$$\boldsymbol{\varepsilon_{calc} = f(P_c, F_{actual}, k, \varepsilon_{guess}, D_e, P_3)} \qquad \textbf{(2-1)}$$

Notice that the area ratio sent into the function is a guess. It is ultimately the area ratio that is adjusted within the code until the calculated thrust is within some tolerance of the actual thrust value ($\boldsymbol{F_{actual}}$). If the area ratio is within the tolerance, the function is done and outputs the area ratio that corresponds to the pressure and thrust inputs. Thus for a

given set of pressure and thrust data, the area ratio can be calculated at every time step. The throat diameter is calculated from the area ratio. The flow diagram is shown in Figure 2-4.

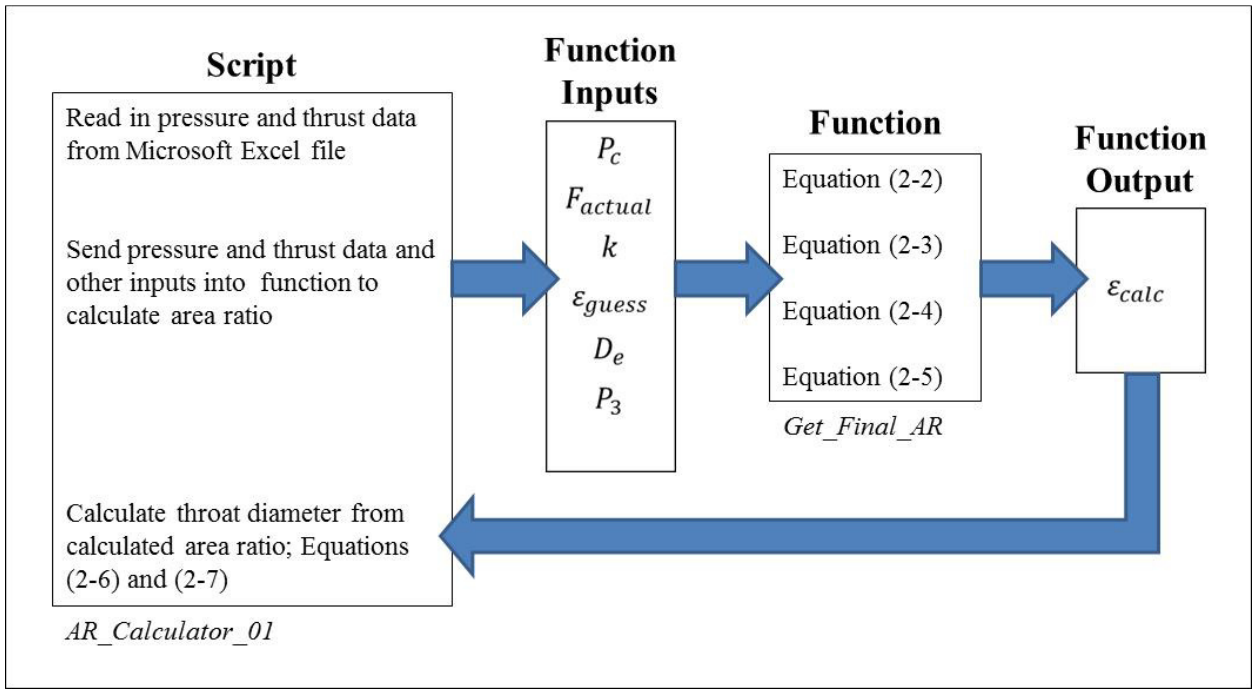

Figure 2-4 Flow Diagram for Calculating Throat Diameter from Pressure and Thrust Data

The first step in the function is to iteratively solve for the exit Mach number (M_2) according to the isentropic nozzle flow Equation (2-2). Exit Mach number is incrementally increased until the right-hand side is within some user-defined tolerance of the left-hand side. Note that the left-hand side is the initial area ratio guess:

$$\varepsilon_{guess} = \frac{1}{M_2}\sqrt{\left\{\frac{1+[(k-1)/2]M_2^2}{1+[(k-1)/2]}\right\}^{(k+1)/(k-1)}} \quad \textbf{(2-2)}$$

Once exit Mach number is determined, the pressure ratio P_2/P_c can be calculated:

$$\frac{P_2}{P_c} = \left[1+\frac{k-1}{2}M_2^2\right]^{-k/(k-1)} \quad \textbf{(2-3)}$$

This pressure ratio is needed to calculate the thrust coefficient, shown in Equation (2-4). Again, note that the area ratio here is the initial guess that was sent into the function.

$$c_f = \sqrt{\frac{2k^2}{k-1}\left(\frac{2}{k+1}\right)^{(k+1)/(k-1)}\left[1-\left(\frac{P_2}{P_c}\right)^{(k-1)/k}\right]} + \frac{P_2 - P_3}{P_c}\varepsilon_{guess} \quad \textbf{(2-4)}$$

Finally, a thrust value is calculated:

$$F_{calc} = P_c A_t c_f \quad \textbf{(2-5)}$$

The calculated thrust value is compared to the actual, measured thrust value that was sent into the function. If the calculated thrust value is within some user-defined tolerance of the measured thrust, than the area ratio for this time step is known. The following two equations are used to calculate throat diameter (D_t) from the area ratio:

$$\varepsilon = \frac{A_e}{A_t} \tag{2-6}$$

$$D_t = \sqrt{\frac{4}{\pi} A_t} \tag{2-7}$$

If the calculated thrust value is not within tolerance of the measured thrust, then a new guess for area ratio is generated and the process is repeated starting at Equation (2-2). It is important to note that the final area ratio for this time step is the initial guess for the next time step. For example, for a data set with 10 Hz data: if the area ratio at time step t = 1.2 seconds is 6.0, than at t = 1.3 seconds, the initial area ratio guess is 6.0. This is a good assumption that reduces computation time. Also note that for each time step, the other function inputs (that is, ratio of specific heats, exit diameter, and ambient pressure) are assumed constant.

There are two instances where the user specifies a tolerance; these instances occur in iterative loops. The first instance is when the exit Mach number is found iteratively, per Equation (2-2). The loop stops iterating once the right-hand-side (RHS) of Equation (2-2) is within 2% of the area ratio guess. The second instance of a user-defined tolerance is for the calculated thrust. The loop (and function) is done once the calculated thrust is within 5% of the measured thrust.

All four sets of test data (refer to Table 2-2) were sent through the Matlab function. In addition to the pressure and thrust data files, Table 2-3 lists the other four function inputs that were used. User-defined tolerances are also provided.

Table 2-3 Function Inputs for each Plastic Nozzle Test

Code Name	Description	Value	Units
gamma	Ratio of specific heats	1.2	-
AR	Initial area ratio guess	6	-
De	Nozzle exit diameter	0.441	in
P3	Ambient pressure	14.7	psia
AR_tolerance	User-defined tolerance for finding exit Mach number	2	%
Thrust_tolerance	User-defined tolerance for finding calculated thrust	5	%

2.3 Results and Discussion

Figure 2-5 shows the function output for each test. The bold, horizontal line indicates the initial throat diameter measurement (0.18 inches). The dashed, horizontal line indicates the final throat diameter measurement (0.25 inches).

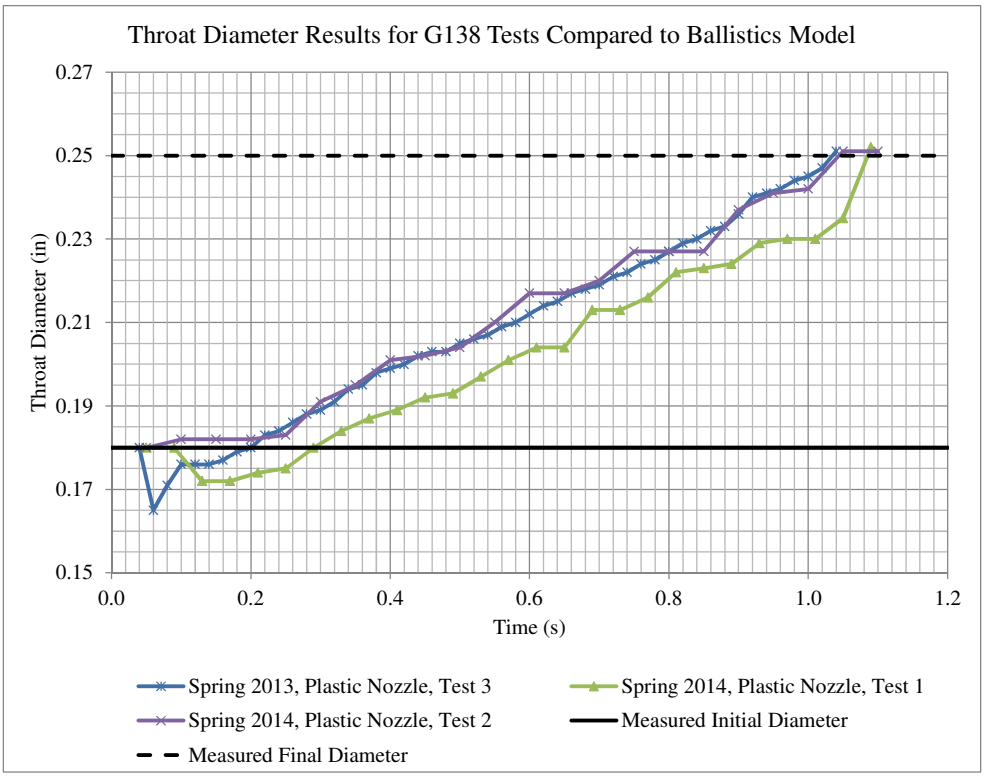

Figure 2-5 Throat Diameter for Three G138 Tests – Indirect Method

Notice that the Spring 2013 Test 3 and the Spring 2014 Test 1 both dip below the initial throat diameter line (Spring 2014 Test 2 stays relatively constant during this time.) There are two possible explanations for this dip: the first is the motor is ramping up to choked, steady state flow during this time. The equations in the Function block in Figure 2-4 assume choked, steady state flow. Another explanation for the initial dip in Figure 2-5 is from Evans and Kuo's work; they observed this same behavior and contributed it to the rapid rise in chamber pressure which induces rapid heating of the throat material, ultimately causing an initial contraction of the throat. Following the initial contraction, thermochemical erosion takes over and the throat diameter begins to increase.

Throat erosion rate is calculated as the change in distance divided by the change in time at each time step. Change in distance is half of the change in throat diameter:

$$\frac{1}{2}[(D_t)_i - (D_t)_{i-1}] \quad \textbf{(2-8)}$$

Chamber pressure and erosion rate are finally plotted in Figure 2-6. An initial assessment revealed a vertical spread in the data around a narrow pressure range. To address this, the average pressure and average erosion rate were calculated for each test. For example, the points shown for the Spring 2014, Plastic Nozzle, Test 2 occurred from 0.25 to 0.85 seconds (data during transient conditions were ignored). The average pressure from 0.25 to 0.85 seconds was calculated. The average erosion rate from 0.25 to 0.85 seconds was calculated. The average pressure and average erosion rate for each test are plotted as the red diamonds in Figure 2-6. A linear curve-fit (anchored at (0, 0)) is shown through the time-averaged data.

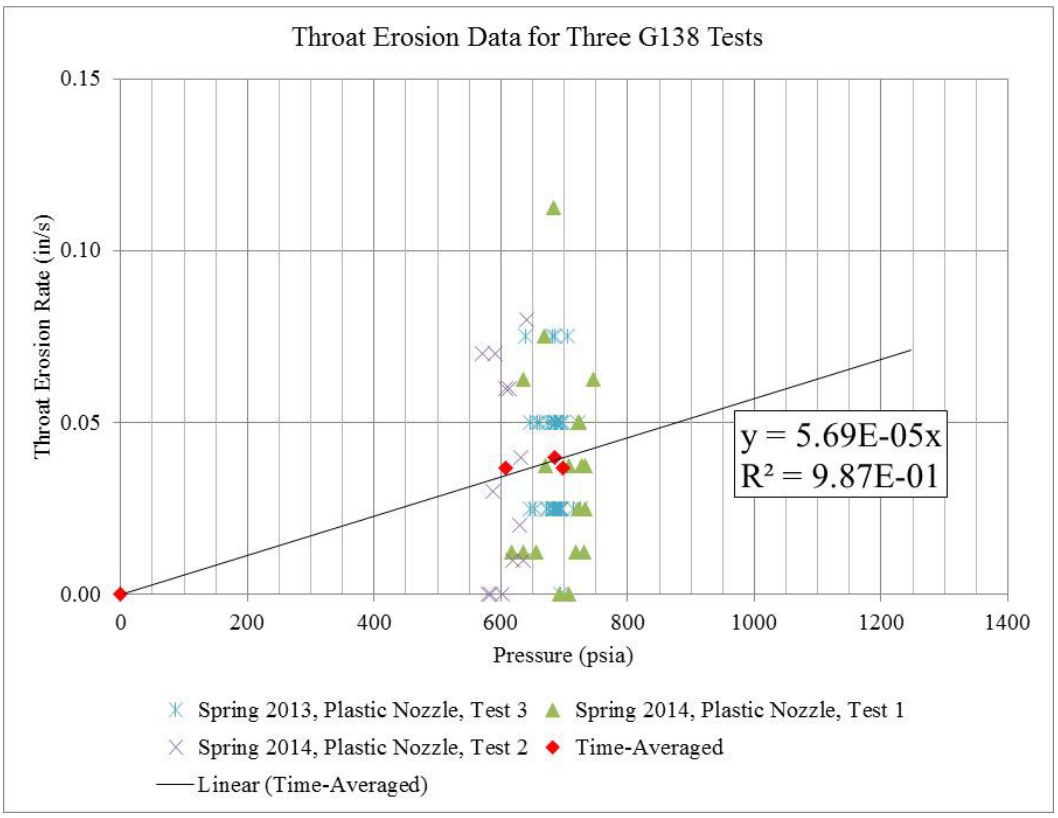

Figure 2-6 Linear Curve-Fit for Chamber Pressure/Erosion Rate Relationship

The equation in Figure 2-6 was incorporated into the ballistics model so that throat diameter is updated at each time step. Figure 2-7 and Figure 2-8 show the ballistics model output compared to the three G138 tests that had throat erosion.

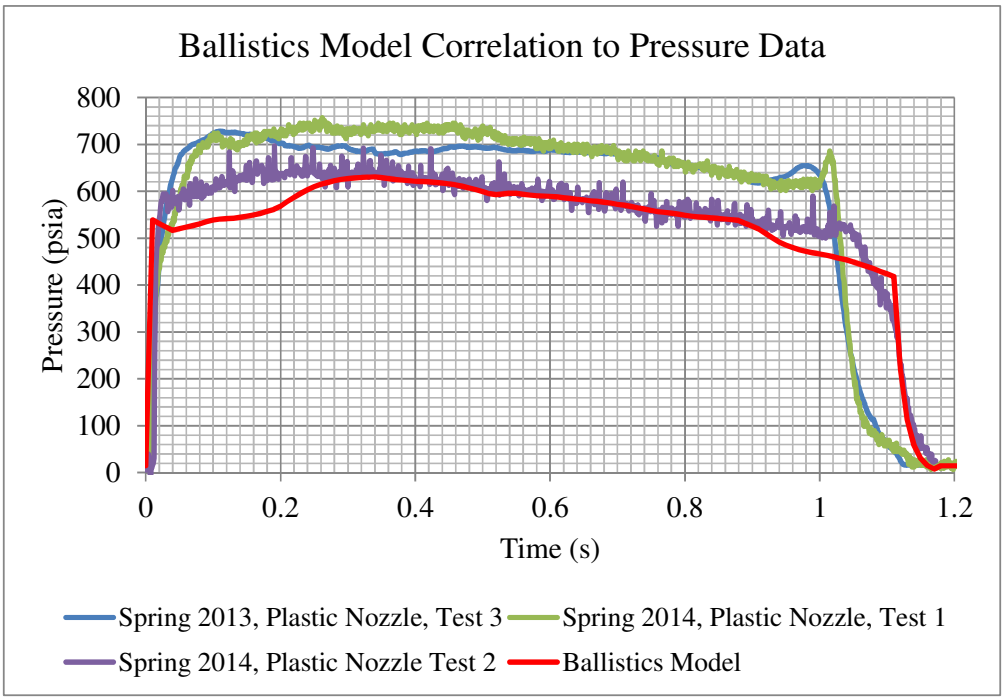

Figure 2-7 Ballistics Model Correlation to Pressure Data, with Throat Erosion

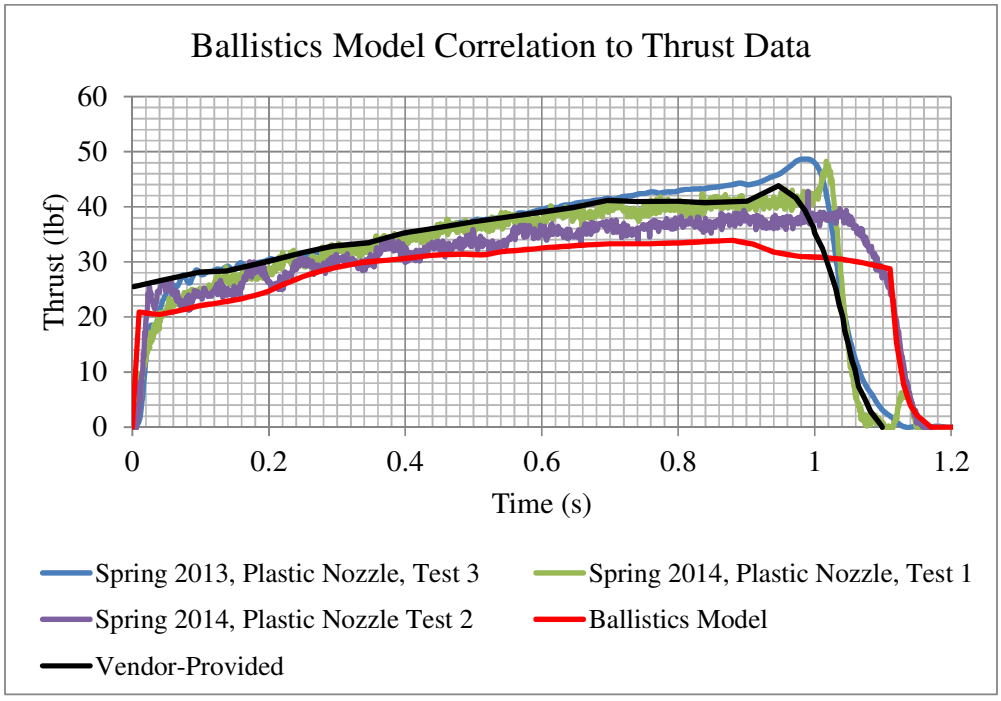

Figure 2-8 Ballistics Model Correlation to Thrust Data, with Throat Erosion

Notice in Figure 2-8 that the vendor-provided thrust curve is also included. The ballistics model correlates well with Spring 2014, Plastic Nozzle, Test 2 from about 0.3 to 0.9 seconds. The dip in pressure at the beginning and near the end of burn is due to the web versus area relationship in the model; recall that the web versus area relationship was derived from the copper nozzle test (refer to Appendix B). Because there were dips in the pressure trace during the copper nozzle test, any predictions the ballistics model generates will also have dips at the same web locations. The ballistics model thrust trace is on the low side of the test envelope, but is considered within family.

After a visual assessment of the pressure and thrust curves, it is important to evaluate the model's capability by comparing some key performance parameters. Table 2-5 shows the comparison between the ballistics model outputs and the Spring 2014, Plastic Nozzle, Test 2 results. As expected, the ballistics model underperforms relative to the test data – all parameters are within 10% of the test data.

Table 2-4 Comparison of Ballistics Model to Plastic Nozzle Test

Performance Parameter	Ballistics Model	Plastic Nozzle Test*	Percent Difference
Maximum Pressure	644	697	-7.6%
Average Pressure	570	583	-2.3%
Maximum Thrust	35	38	-9.4%
Average Thrust	30	33	-7.6%
Specific Impulse	215.0	233.7	-8.0%
Total Impulse	33.0	35.3	-6.5%

* Values are from Spring 2014, Plastic Nozzle, Test 2

To strengthen the correlation between the model and the test results, four items are identified for future work: 1) derive a new web versus area relationship from a plastic nozzle test and incorporate it into the ballistics model; 2) update model to trigger the start of throat erosion (currently, throat erosion begins at time t=0 in the model); 3) investigate characteristic velocity (c^*) efficiency of this propellant; and 4) update linear curve-fit to a power-fit in Figure 2-6, like Evan's correlation in Figure 1-6.

Figure 2-9 shows the ballistics model results for throat diameter compared to the throat diameters that were calculated with the indirect method. It is clear the slope of the red curve correlates very well with the slopes of the test data. Incorporating the throat erosion trigger in the model (discussed in the previous paragraph) would shift the red curve to the right, bringing the ballistics model right in-family with the test results. This means the chamber pressure/erosion rate relationship that was derived from the test data is sufficient for the scope of this work.

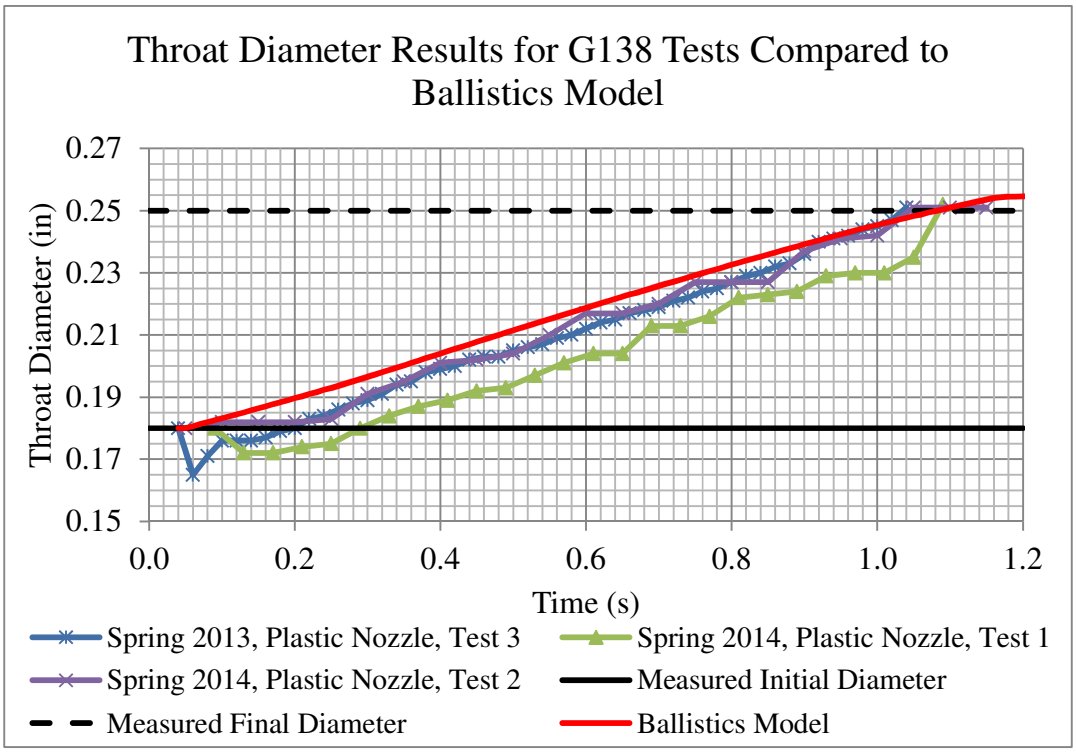

Figure 2-9 Ballistics Model Output Compared to Indirect Method

Ideally, the same ballistics model should accurately predict rocket performance for cases when throat erosion is not present, as in the Spring 2014 Copper nozzle test. Throat erosion was set to zero in the model. Figure 2-10 and Figure 2-11 show the ballistics model output compared to the pressure and thrust test data, respectively.

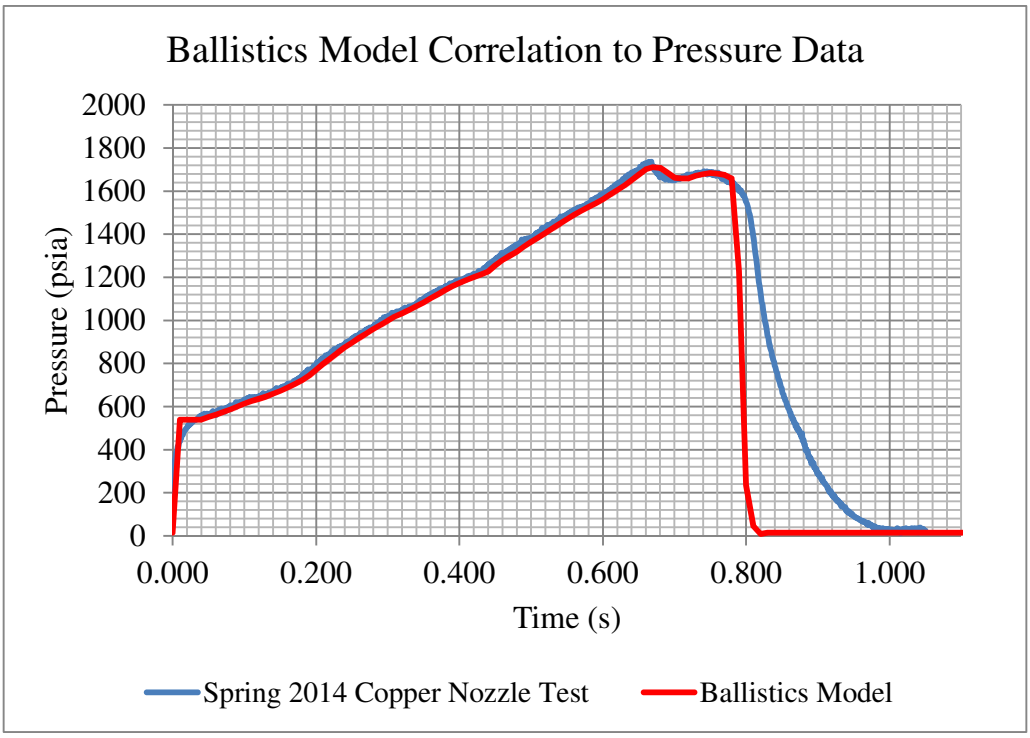

Figure 2-10 Ballistics Model Correlation to Pressure Data, No Throat Erosion

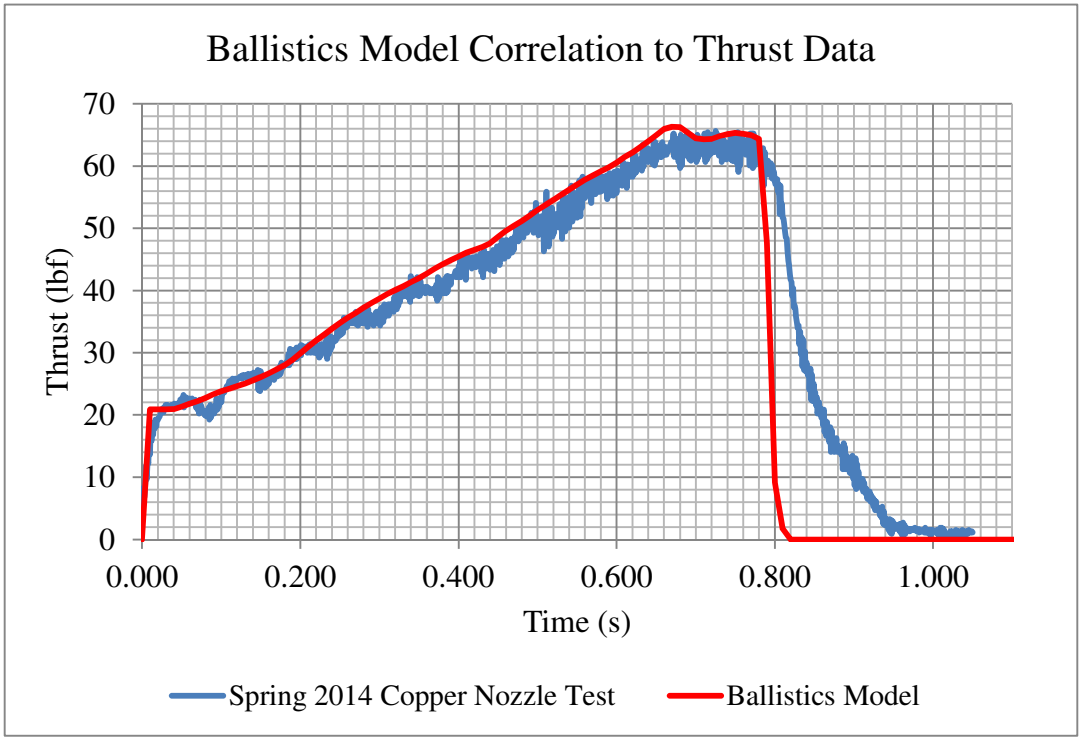

Figure 2-11 Ballistics Model Correlation to Thrust Test Data, No Throat Erosion

Visually, the ballistics model correlates well with the test data. In both the pressure and the thrust plots, the ballistics model shows a steep drop-off at about 0.8 seconds. The reason for this is that the ballistics model does not account for any effluent mass flowing out of the motor after burnout. The steep drop off is really an indication of when the last of the solid propellant is consumed in the motor.

After a visual assessment of the pressure and thrust curves, it is important to evaluate the model's capability by comparing some key performance parameters. Table 2-5 shows the comparison between the ballistics model outputs and the Copper Nozzle Test.

Table 2-5 Comparison of Ballistics Model to Copper Nozzle Test

Performance Parameter	Ballistics Model	Copper Nozzle Test	Percent Difference
Maximum Pressure	1711	1737	-1.5%
Average Pressure	1154	1155	-0.1%
Maximum Thrust	66	66	1.0%
Average Thrust	45	42	5.3%
Specific Impulse	228.1	216.4	5.4%
Total Impulse	35.1	33.2	5.6%

Due to the model's slight over-prediction of average thrust, total impulse and specific impulse are also high. All other performance parameters show good correlation to the test data (within 5%).

The indirect method for determining throat diameter and thus throat erosion rate produces reasonable results. The same ballistics model accurately predicts for cases with throat erosion and for cases without throat erosion. Thus the pressure/erosion rate equation

developed in this section is believable for the scope of this analysis. It is important to note that the equation is limited by the pressure range that the test data covered – recall the relatively flat pressure traces (that is, constant pressure) in the plastic nozzle tests. The analyst must understand that this limitation exists and must take it into account when generating pressure and thrust predictions.

One limitation of the indirect method is that throat diameter is solved for iteratively. Basically when a calculated thrust value is within some user-defined tolerance of the measured thrust value, the area ratio (and thus the throat diameter) is declared to be 'known' at that time step. The computer program then moves on to the next time step to repeat the process at that new time step. The fact that there is a user-defined tolerance in the indirect method is an acknowledgement that some amount of inaccuracy is acceptable, which motivates the investigation of a more direct method.

CHAPTER 3

Approach – Direct Method

The literature revealed that real-time x-ray transmission can be used as a direct method to observe time-dependent changes inside a solid rocket motor. The purpose of this chapter is to investigate how different elements of the current x-ray test setup affect the measurement accuracy of a simulated throat diameter.

In order to develop a method for analyzing x-ray data, it was necessary to simulate an x-ray image of an object representative of the throat section of a solid rocket motor. A repeatable process for extracting the diameter from the transmitted x-ray image was developed. Actual x-ray images of a dynamic calibration standard were collected. The process for extracting throat diameters from each image was tested to determine the accuracy of the direct method. X-ray images were collected in both static and dynamic environments to determine how motion during continuous x-ray imaging affected the results.

This chapter is made up of four parts. First, the x-ray transmission simulation is described, followed by the analysis strategy for extracting throat diameters from an x-ray image. Then the test setup, equipment, and test matrix used to obtain x-ray images is provided. Finally, the experimental results are presented and discussed.

3.1 X-ray Transmission Simulation

In order to gain a better understanding of how to analyze x-ray data, it was desirable to simulate an x-ray image of an object with user-defined dimensions – a dynamic calibration standard in this case. The cross-section of each step in the calibration standard is represented as two concentric circles where the large circle is the outside diameter of the standard. The small circle represents the inside diameter.

This is assumed to be a 2D problem; thus the x-ray detector is represented as a single column of pixels. The number of pixels and the pixel area height are defined by the user. Each x-ray beam is treated as a vector that extends from the x-ray generator to each pixel on the detector. The x-ray generator is treated as a point source and coincides with the origin of the coordinate frame. The positive x-axis extends from the point source toward the object and detector. The user can also define the source-to-object and the object-to-detector distances.

Figure 3-1 illustrates the setup for this problem. In this example, the detector is 4.0 inches from the source and the object is 1.0 inch from the detector. The object is just over 1.0 inch in diameter (blue circle) with a 0.18 inch inner bore (red circle). For the

purposes of visualization, the detector is represented with 11 pixels in Figure 3-1. In reality, the detector has 1024 vertical pixels which is a user-input in the simulation.

After the object geometry and the test setup are established in the simulation, LAC values are assigned to different regions. For the purposes of this simulation, there are two regions of interest: Region 1 is the environment in which the calibration standard resides (typically air) and Region 2 is the calibration standard material (acrylic in this case). It is important to note that the inner bore of the calibration standard is air and is thus assigned the same LAC value as Region 1. LAC values are determined empirically and are a function of both material density and the x-ray intensity leaving the source. Linear attenuation coefficients for air and acrylic that were used in the simulation are provided in Appendix D. Note that the simulation updates each Region's LAC value based on the user-defined x-ray intensity leaving the source.

The x-ray prediction simulation is designed to determine the linear distances that each x-ray beam passes through and through which regions it passes. Given that the object is represented by two concentric circles (in a 2D plane), there exist a finite number of possible solutions for each line that extends from the source to the detector. Figure 3-1 illustrates three solution possibilities, shown in the column of numbers on the right side of the figure. For example, the top right number (0) indicates that there are zero solutions for the x-ray that extends from the source to that pixel; the ray does not intersect any of the circles. The third number (2) indicates that there are two solutions for the x-ray that extends from the source to that pixel; the ray intersects only the largest circle in two

locations. Intersection points are highlighted in each circle's respective color: blue for the large circle and red for the small one. The maximum number of solutions (4) is shown at the middle pixel location where the x-ray beam passes through both circles.

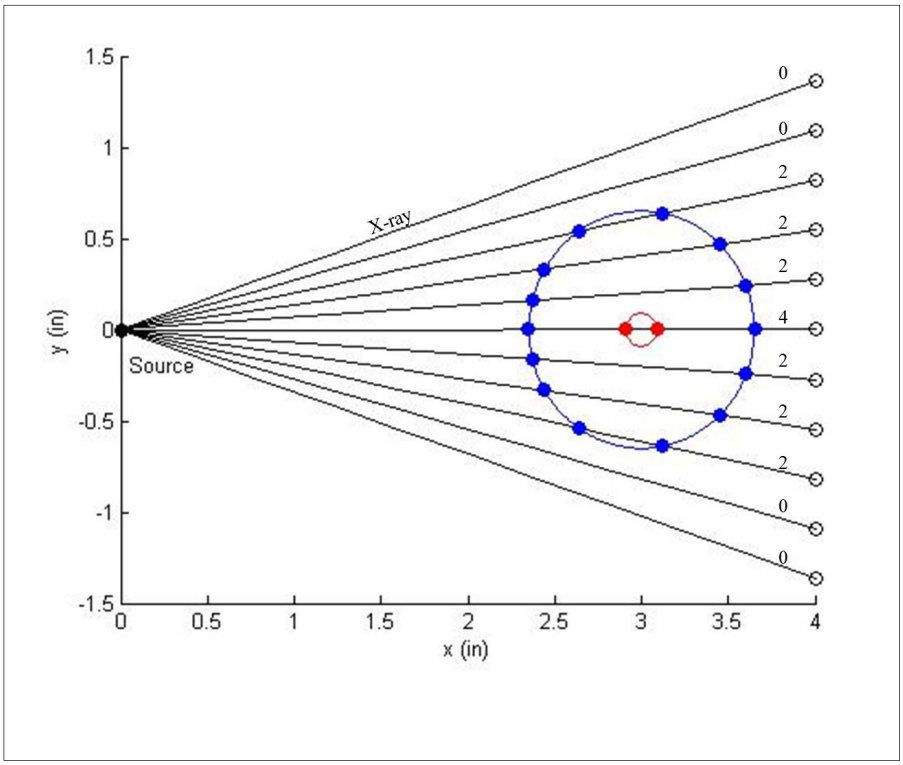

Figure 3-1 Finite Number of Solutions at Each Pixel

There are two other solution possibilities that are not shown in Figure 3-1; they are solutions 1 and 3. Solution 1 is an indication that the x-ray intersects the large circle at its tangent. Solution 3 is an indication that the x-ray intersects the large circle, then the small circle at its tangent, and finally exits the large circle.

The number of solutions at each pixel is an indicator of which regions the x-ray passes. For example, a pixel with 2 solutions means the x-ray can only pass through the large

circle and never passes through the small circle. With this type of logic and the known (x, y) locations of each intersection solution, the intensity at each pixel is calculated using the Beer-Lambert equation, discussed in Section 1.3.1.

Once the intensity at each pixel is known, a linear grayscale color map is applied and displayed. The values in Table 3-1 were input into the simulation. Figure 3-2 shows the simulation outputs.

Table 3-1 X-ray Simulation Input Table for Grayscale Images

Input Variable	Description	Value	Units
X_source_object	Distance from source to object	3	inch
X_object_detector	Distance from object to detector	1	inch
I_initial	X-ray intensity leaving the source	200	kV
D2	Large diameter	1.3	inch
D3	Small diameter	0.18	inch
Region1_LAC	Region 1 material and LAC	'Air' (LAC = 3.77E-04)	1/inch
Region2_LAC	Region 2 material and LAC	'Plexiglass' (LAC = 4.06E-01)	1/inch
N_vert_pixels	Number of vertical pixels	11 (Left); 1024 (Right)	-
Pixel_area_height	Total pixel area height	3	inch

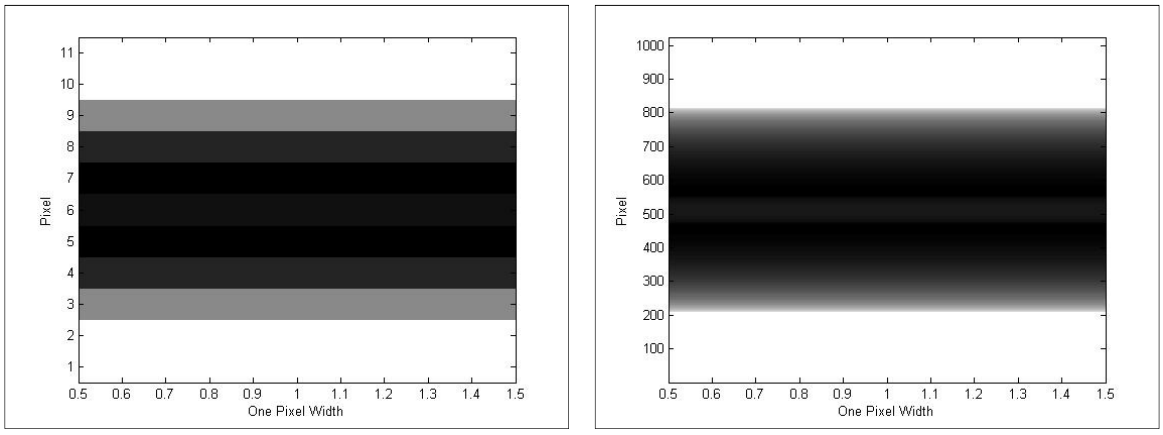

Figure 3-2 X-ray Simulation Grayscale Images with 11 Pixels (Left) and 1024 Pixels (Right)

Because this is assumed as a 2D problem, the width of the grayscale images is that of one pixel. The y-axis is the vertical column of pixels on the detector. The only difference between the left and right image in Figure 3-2 is the number of vertical pixels; together they illustrate how the number of pixels affects the image resolution.

The simulation also outputs a graph of intensity versus pixel, like that shown in Figure 3-3. The intensity versus pixel graph is very useful for extracting the inner diameter, which is discussed in the next section.

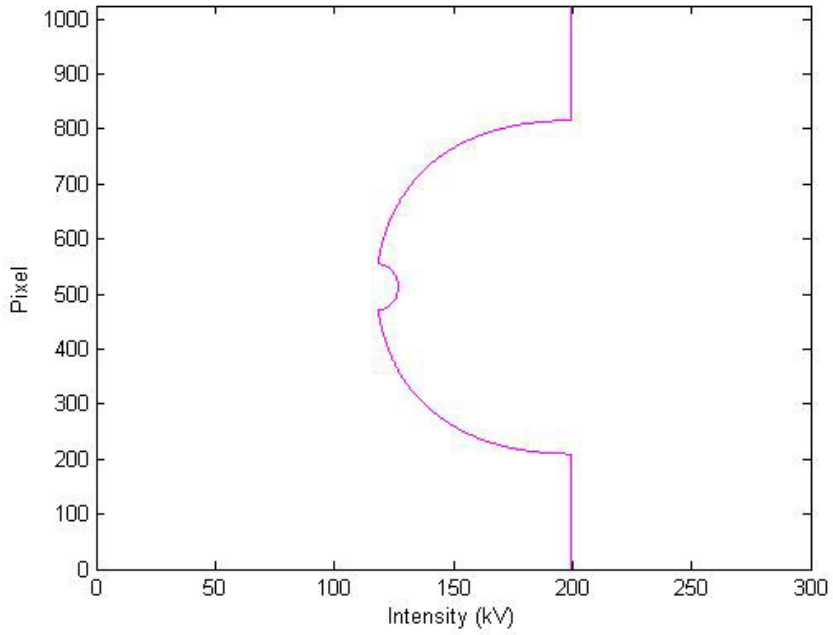

Figure 3-3 Intensity versus Pixel Graph

3.2 Analysis Strategy

The left side of Figure 3-4 shows the cross-section of the calibration standard in a notional test setup, where the source-to-detector distance is 4 inches. The right side of Figure 3-4 shows how the features in the intensity versus pixel graph correspond to the

two inside diameters of the standard. The top and bottom tangent locations in the cross-section view correspond to the two discontinuities (on each side of the small hump) in the intensity graph. For the remainder of this thesis the two discontinuities and the small hump are referred to as "the feature" in the x-ray intensity data. Because the feature can be correlated to the edge of the inside diameter, it is desirable to develop a repeatable and streamlined method for locating this feature in the intensity versus pixel graph. Note, as the inside diameter increases in the standard, the feature in the intensity data becomes wider and taller.

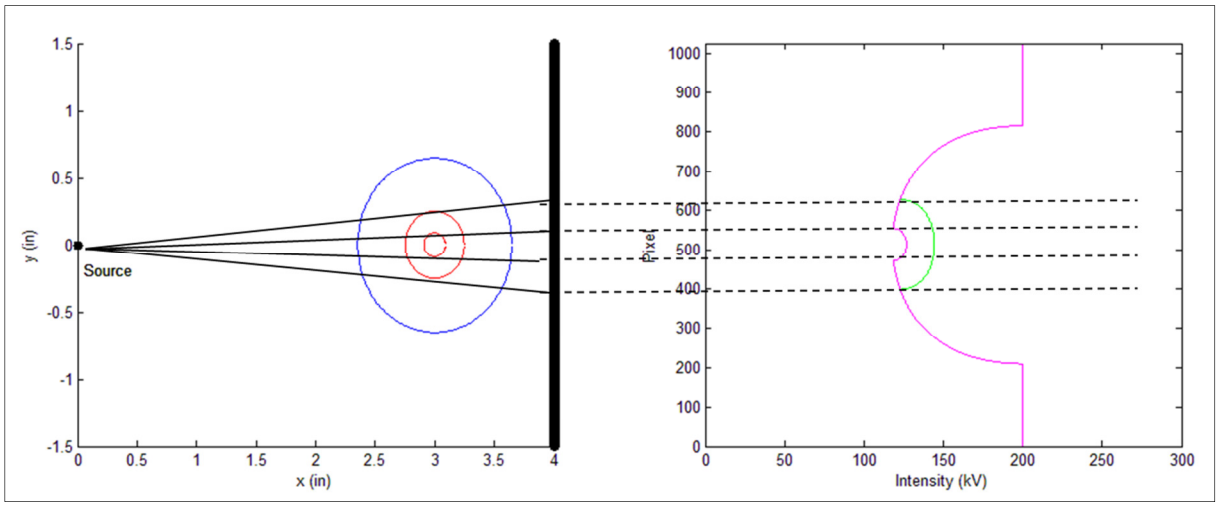

Figure 3-4 Inside Diameters in the Intensity versus Pixel Graph

Initially, a simple minimum-value approach was used in the simulation to calculate the diameter in the intensity data. The number of pixels between the discontinuities was calculated, then multiplied by the pixel height, and finally de-magnified. The values in Table 3-2 and Table 3-3 were input into the simulation. The final de-magnified diameter (calculated with the minimum-value approach) is shown in the Simulation Output in Table 3-3.

Table 3-2 X-ray Simulation Input Table for Input versus Output

Input Variable	Description	Value	Units
D2	Large diameter	1.3	inch
Region1_LAC	Region 1 material and LAC (dependent on kV value)	'Air'	-
Region2_LAC	Region 2 material and LAC (dependent on kV value)	'Plexiglass'	-
N_vert_pixels	Number of vertical pixels	1024	-
Pixel_area_height	Total pixel area height	4	inch

Table 3-3 X-ray Simulation Input versus Output

Case	*SOD* (in)	*ODD* (in)	kV	Simulation Input (in)	Simulation Output (in)	% Difference	Magnification Factor
1	10.5	27	50	0.1800	0.1805	0.28%	3.57
2	15	22.5	50	0.1800	0.1828	1.56%	2.50
3	22	15.5	50	0.1800	0.1810	0.56%	1.70
4	26.25	11.25	50	0.1800	0.1832	1.78%	1.43
5	26.25	11.25	25	0.1800	0.1832	1.78%	1.43
6	26.25	11.25	75	0.1800	0.1832	1.78%	1.43
7	26.25	11.25	100	0.1800	0.1832	1.78%	1.43
8	26.25	11.25	50	0.3440	0.3473	0.96%	1.43
9	26.25	11.25	50	0.5080	0.5113	0.65%	1.43
10	26.25	11.25	50	0.6720	0.6754	0.51%	1.43
11	26.25	11.25	50	0.8360	0.8395	0.42%	1.43

The engineer can deduce the following from the simulation outputs: 1) the magnification factor, which is a function of the source-to-object distance and the object-to-detector distance, affects the accuracy of the diameter measurement, 2) changing source intensity (that is, kV value) should have little to no effect on the diameter measurement, and 3)

accuracy should improve slightly as the diameter gets larger. To validate these statements, actual x-ray images were captured and the intensity data analyzed; results are provided in Section 3.3.4.

It is important to note that the minimum-value approach is only acceptable when analyzing simulated data. This realization occurred after obtaining some of the first x-ray images. To remedy the fact that the minimum-value approach alone was insufficient for finding the edge in the real x-ray data, a pixel-averaging step was added to the process, per the thesis committee's recommendation. In this new step, a set of pixels in the image background is selected and averaged. The entire x-ray image is then divided by the average pixel value. This new step normalizes the raw intensity data and nearly eliminates the noise.

Figure 3-5 illustrates the rationale behind adding the pixel-averaging step to the edge detection process. In the first cell, actual x-ray intensity data is shown. At this scale, the data appears smooth. In the second cell, the scale is adjusted to get a better look at the feature. It is clear that there could be some subjectivity to identifying the edge positions of the feature. To remedy the noise in the raw intensity data, a set of pixels in the image background is selected and averaged. The pixel area is shown by the black box in the third cell. This area was selected because it consisted of a combination of white space and lighter shades of gray that are not near the inside diameter of the standard. Every pixel in the x-ray image is then divided by the average pixel value, resulting in the normalized intensity, identified as the blue line in cell four. A distinct edge can now be

found in the normalized data manually or with computer assistance. It is important to note that the average pixel value has a major impact on the shape of the normalized intensity curve. The location chosen in Figure 3-5 produced a reasonable normalized curve; future work consists of optimizing the average pixel value location.

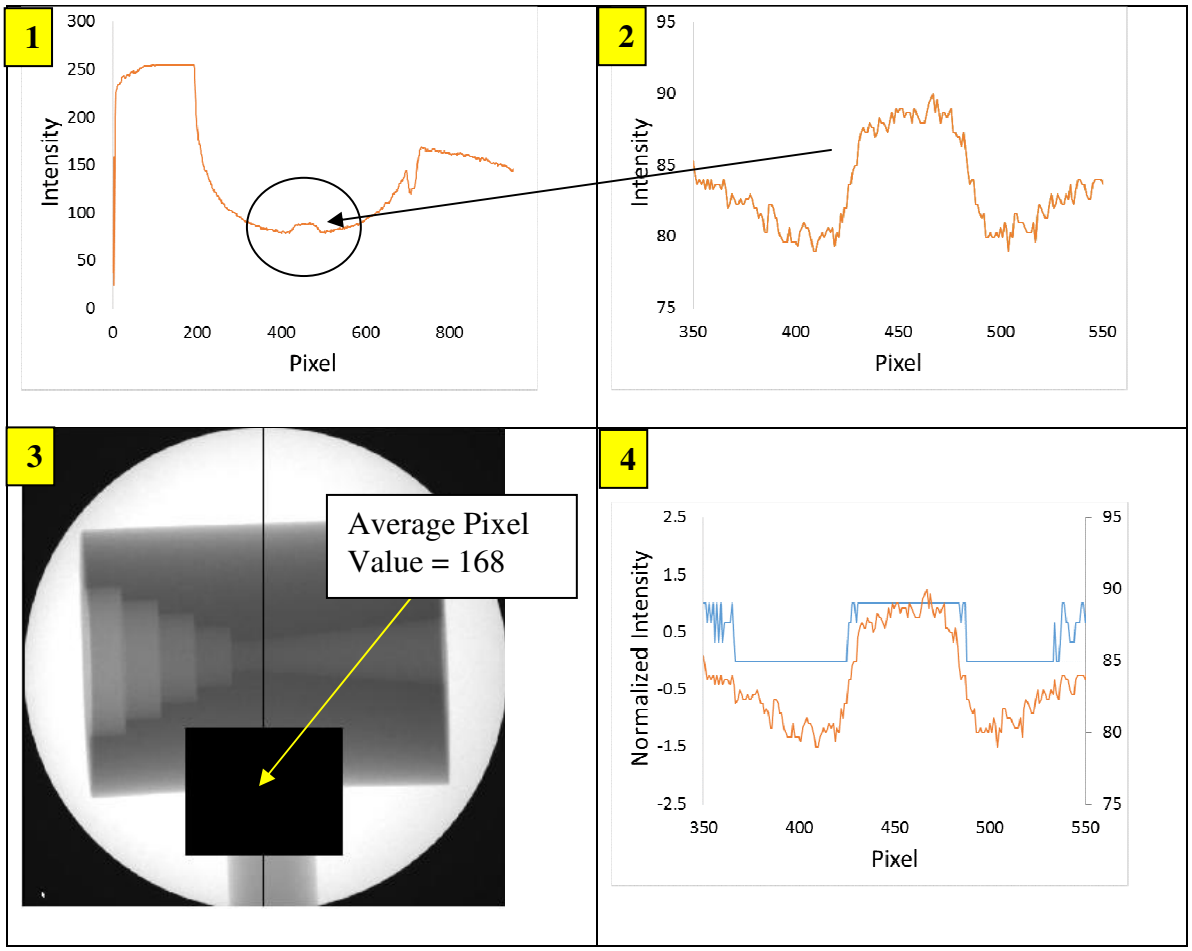

Figure 3-5 Pixel-Averaging Process (Dynamic Test 1, Frame 239)

With the pixel-averaging rationale in place, the following process was used to calculate the inside diameter of the calibration standard from a real x-ray image:

1. Calculate an average pixel value from a set of pixels in the x-ray image background.
2. Divide every pixel in the x-ray image by the average pixel value.
3. Plot the raw intensity and the normalized intensity.
4. Locate the discrete points on both sides of the feature. This is described further in the paragraph below.
5. Calculate the number of pixels between the discrete pixel locations and multiply the number of pixels by pixel height.
6. De-magnify the dimension from Step 5 using Equation (1-10). This is the calculated diameter, which is then compared to the actual diameter.

To locate the discrete points on both sides of the feature, the operator performs two tasks: first, the operator establishes two viewing windows in which the algorithm can search. One viewing window is for the left side of the feature and the other viewing window is for the right side of the feature. Second, the operator inputs a threshold value. The algorithm then searches for the threshold value along the normalized curve, within each viewing window. The discrete points at which the threshold is breached are considered the edge of the diameter. For example, in the bottom right plot in Figure 3-5, the operator establishes viewing windows from 400 to 450 pixels (for the left side of the feature) and from 450 to 525 pixels (for the right side of the feature). The operator sets the threshold on the normalized curve to 0.1. With this setup, the algorithm finds the vertical line on each side of the feature; these discrete points are considered the edge of the diameter.

3.3 Test Description

The test setup is shown in Figure 3-6. Three of the main components of the setup are labeled: x-ray tube (1), image intensifier (2), and test stand (3). These three components are discussed in the next section. The x-ray calibration standard (not shown) is discussed in Section 0.

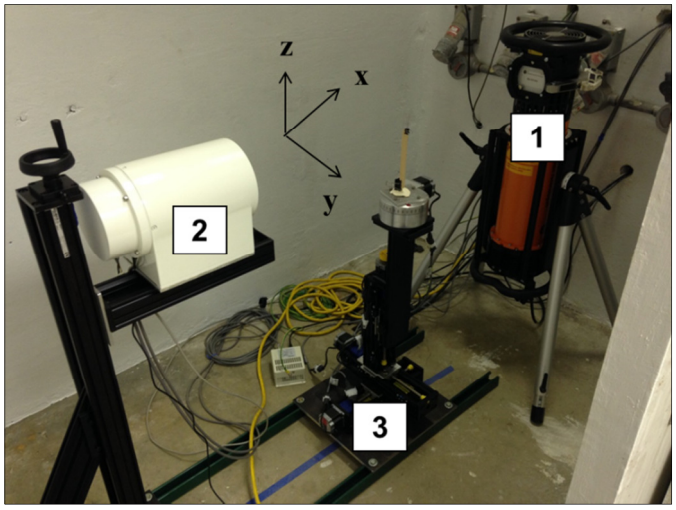

Figure 3-6 X-ray Test Setup; Tube (1), Detector (2), Test Stand (3)

3.3.1 Equipment

The x-ray tube is a 200 kV, 600 Watt unit. It has a 40 degree by 60 degree elliptical emergent beam, a tungsten anode, and a 1.0 mm focal spot size. The image intensifier is setup 36 inches from the x-ray tube. The image intensifier is mounted on a vertical rail so that its height is adjustable. This is convenient for warming up the x-ray tube; prior to warm-up, the image intensifier is lowered out of view of the x-ray tube. This extends the life of the image intensifier.

A Kappa CCD camera for x-ray imaging is installed on the back side of the image intensifier. It can take 30 frames per second (fps) and has 1024 by 1024 picture elements. Each element is 5.5 by 5.5 micrometers (μm). The camera software, called HiRes3, is used to capture images during static testing. Debut Video Capture Software is used to record the computer screen during dynamic testing. For the rest of this thesis the image capture method is referred to as "camera software" for static testing and "video capture software" for dynamic testing.

The test stand was assembled with motorized BiSlide technology from Velmex. It provides translation along the x, y, and z-axis, as well as rotation about the z-axis for objects mounted to the rotary table. Translation in the y-axis is used during static calibration (to investigate changes in accuracy by changing source-to-object distance in the y-direction). Translation in the x-axis is used during dynamic calibration (to investigate changes in accuracy by changing the throat diameter in real-time). Table 3-4 summarizes the x-ray test equipment. The calibration standard, which is mounted on the rotary table, is discussed in the next section.

Table 3-4 X-ray Test Equipment

Equipment	Manufacturer	Part Number	Technical Data
X-ray Tube	GE	ERESCO 200 MF4-R	200 kV, 600 W
Image Intensifier	Toshiba	E5877J-P1	4-inch field size
CCD Camera	Kappa	HiRes3-XR	30 fps, 1024x1024
Translating Table	Velmex	PK266-03A-P1	BiSlide, 5" travel

3.3.2 Calibration Standard

The x-ray calibration standard is shown in Figure 3-7. The circular base was designed to adapt directly to the test stand. It is made of acrylic and stands 9 inches tall. There are two sides of the calibration standard – a static side and a dynamic side. It was designed this way so that the method for calculating the inside diameter could be tested in a static environment and a dynamic environment.

Figure 3-7 Calibration Standard

The right side of the standard, shown in Figure 3-8 is for static calibration. Each step was bored to a known diameter with the smallest diameter equal to 0.18 inches (which is the initial throat diameter of the G138 nozzle). The static side was designed so that measurements of different diameters could be x-rayed in a static environment and compared to actual values. The results of static tests should give an indication of system

accuracy. The method of extracting throat diameter measurements from an x-ray image is discussed in Section 3.2.

The left side of the standard, shown in Figure 3-8 is for dynamic calibration. It was designed to simulate a G138 throat eroding with time. If one were to place the standard on a translating table and move the table at a controlled velocity (to the right in this case), it would appear that the inner diameter increases with time relative to a fixed vertical line in the image. This is how simulated throat erosion is achieved. The large, final diameter on the dynamic side is 0.375 inches. Thus, the G138 nozzle erosion tests (where the throat opened from 0.18 to 0.25 inches) can be simulated with this calibration standard. The velocity at which the table must translate to achieve a G138 erosion simulation is discussed further in the next section. A drawing of the top portion of the standard is provided in Appendix C.

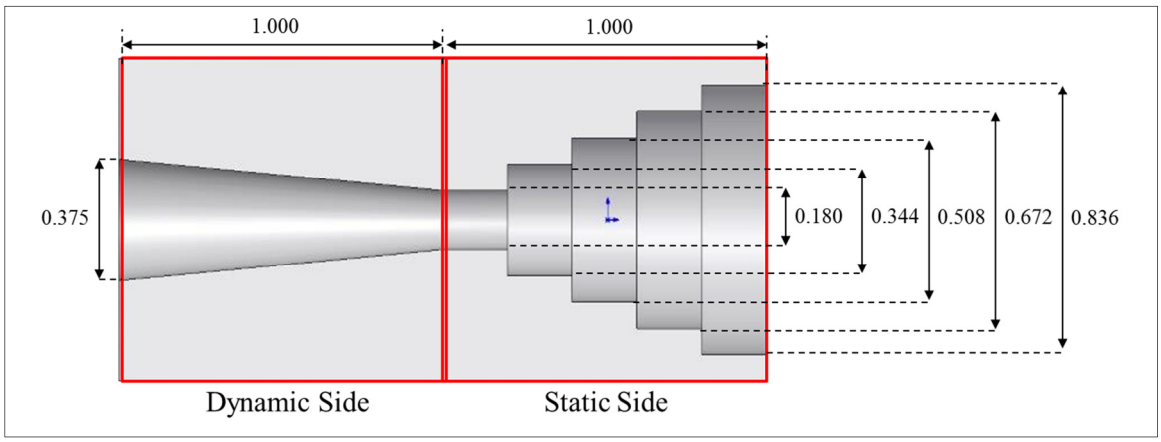

Figure 3-8 Dimensioned Calibration Standard

3.3.3 Test Matrix

The Static Calibration Test Matrix is shown in Table 3-5. Tests 1 thru 4 investigate how varying the x-ray source-to object distance (SOD) and the object-to-detector distance (ODD) affects the measured diameter results. The method of measuring the diameter from an x-ray image is discussed in Section 3.2. Notice that the total distance from the x-ray source to the detector remains constant (that is, 37.5 inches). The x-ray source kV value also remains constant to ensure it does not affect the results.

Tests 5 thru 7 investigate how varying kV value affects the measured diameter results. Recall that kV value is a measure of the x-ray source's penetrating capability. There is a balancing act between ensuring a sufficient amount of x-rays reach the detector and ensuring the detector is not saturated with an unnecessary amount of x-rays, which ultimately degrades the life of the image intensifier and the potential contrast of the features that reveal the throat diameter.

Finally, Tests 8 thru 11 investigate measurement repeatability. Notice that the diameters in the Actual Diameter column are the known diameters in the calibration standard.

Table 3-5 Static Calibration Test Matrix

Test	*SOD* (in)	*ODD* (in)	kV	Actual Diameter (in)	Calculated Magnification Factor
1	10.5	27	50	0.180	3.57
2	15	22.5	50	0.180	2.50
3	22	15.5	50	0.180	1.70
4	26.25	11.25	50	0.180	1.43
5	26.25	11.25	25	0.180	1.43
6	26.25	11.25	75	0.180	1.43
7	26.25	11.25	100	0.180	1.43
8	26.25	11.25	50	0.344	1.43
9	26.25	11.25	50	0.508	1.43
10	26.25	11.25	50	0.672	1.43
11	26.25	11.25	50	0.836	1.43

At the conclusion of the Static Calibration Test Matrix, the engineer should have 1) a good understanding of how varying the distances (that is, the magnification factor) affects the diameter measurement, 2) a good understanding of how kV value affects the diameter measurement, and 3) a good understanding of how repeatable the results are. The Static Calibration Matrix was designed to investigate the effects of varying these parameters.

The Dynamic Calibration Test Matrix is shown in Table 3-6. The purpose of these tests is to investigate the accuracy of the diameter measurement method in a controlled dynamic environment. The dynamic environment is simulated by translating the tapered side of the calibration standard across the x-ray source; multiple speeds are investigated to determine if accuracy is affected by table speed. Each speed is tested twice to measure method repeatability.

Table 3-6 Dynamic Calibration Test Matrix

Test	*SOD* (in)	*ODD* (in)	kV	Target Table Speed (in/s)
1	24.75	12.75	50	0.1
2	24.75	12.75	50	0.1
3	24.75	12.75	50	0.3
4	24.75	12.75	50	0.3
5	24.75	12.75	50	0.5
6	24.75	12.75	50	0.5

A quick assessment of the calibration standard dimensions revealed that a table velocity of 0.359 inch per second is required to simulate the G138 throat erosion. That is, if the table were to move laterally at 0.359 inch per second, the throat diameter would open up from 0.18 to 0.25 inches in 1 second, which is the G138 burn time. Notice in the test matrix that this speed (0.359 inch per second) is within the speeds tested. Thus, at the conclusion of the Dynamic Calibration Test Matrix, the engineer should have a good understanding whether burn time (which is represented by table speed) affects the accuracy of the throat diameter measurement.

3.3.4 Results and Discussion

3.3.4.1 Static Calibration

The tests in the Static Calibration Test Matrix were completed November 4, 2014 in the UAH X-Ray Facility. Results are shown in Table 3-7. The source-to-object distance and the object-to-detector distance were measured with a tape measure, from the front face of the x-ray tube to the mid-section of the calibration standard and from the mid-

section of the calibration standard to the from face of the image intensifier, respectively. The Calculated Magnification Factor (M.F.) was then calculated with these distances according to Equation (1-10).

The Actual M.F. was determined during post-test analysis for each test. The edge detection process with pixel-averaging (described in Section 3.2) was performed first. The error between the measured diameter and the actual diameter was then driven to zero by adjusting the magnification factor. The resulting magnification factor is shown as Actual M.F. in Table 3-7.

Table 3-7 Static Calibration Results

Test	Image Filename	*SOD** (in)	*ODD* (in)	kV	Actual Diameter (in)	Calculated M.F.	Actual M.F.	% Diff.
1	20141104_001.tif	10.5	27	50	0.180	3.57	2.99	19.4%
2	20141104_002.tif	15	22.5	50	0.180	2.50	2.15	16.3%
3	20141104_003.tif	22	15.5	50	0.180	1.70	1.61	5.9%
4	20141104_004.tif	26.25	11.25	50	0.180	1.43	1.32	8.2%
5	20141104_005.tif	26.25	11.25	25	0.180	1.43	-	-
6	20141104_006.tif	26.25	11.25	75	0.180	1.43	1.35	5.8%
7	20141104_007.tif	26.25	11.25	100	0.180	1.43	-	-
8	20141104_008.tif	26.25	11.25	50	0.344	1.43	1.44	0.8%
9	20141104_009.tif	26.25	11.25	50	0.508	1.43	1.44	0.8%
10	20141104_010.tif	26.25	11.25	50	0.672	1.43	1.44	0.8%
11	20141104_011.tif	26.25	11.25	50	0.836	1.43	1.42	0.6%

* Values include 1.5 inches for submerged point source location.

Notice the significant and changing percent difference between Calculated and Actual M.F. for Tests 1 thru 4. This information is also plotted in Figure 3-9 to support the following discussion. The results in Figure 3-9 indicate that the 1.5 inches included in the source-to-object distance (to account for the submerged point source in the tube head) is not sufficient. Further investigation revealed that the point source is submerged further than 1.5 inches from the face of the tube. Adjusting the submerged distance to 4.5 inches produced the results in Figure 3-10.

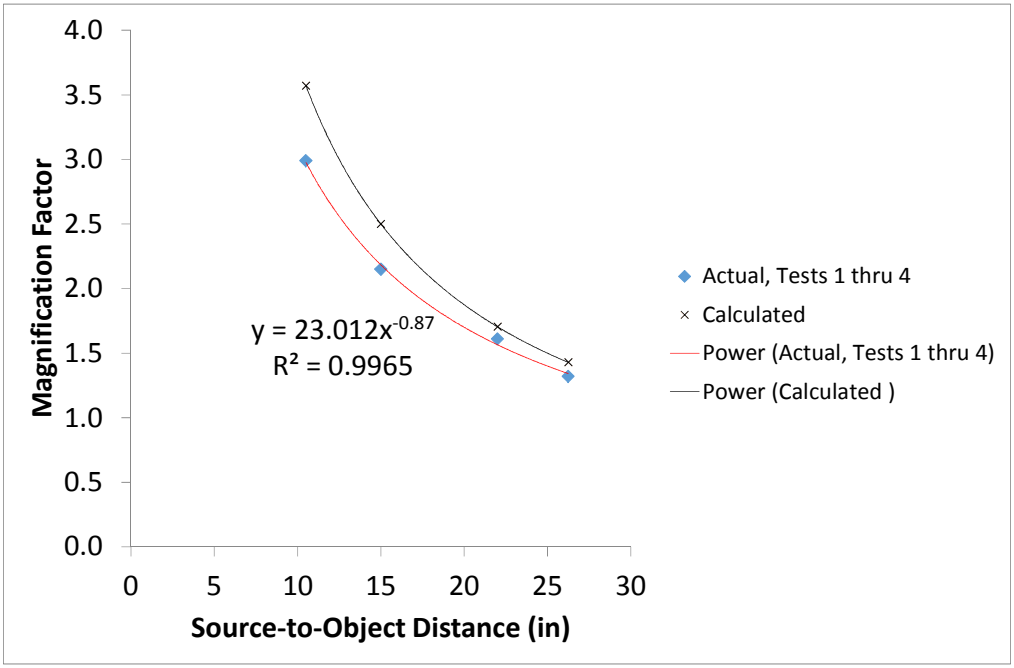

Figure 3-9 Calculated versus Actual, Point Source Submerged 1.5 inches

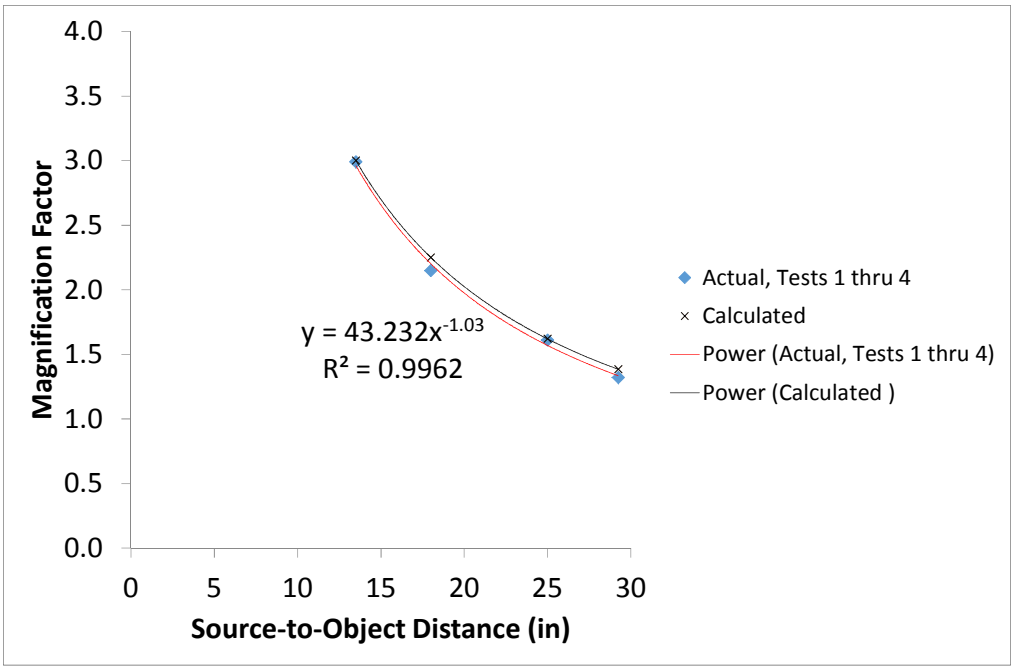

Figure 3-10 Calculated versus Actual, Point Source Submerged 4.5 inches

The detector consists of 256 pixels per inch (i.e. the detector has a 4-inch imaging area with 1024 by 1024 pixels). Pixel height is 0.0039 inches. This pixel height is considered a measure of accuracy, inherent to the system. Every pixel on the detector is assigned one value of gray, proportional to the amount of x-rays that reach that pixel. The edge of a magnified diameter on the detector could be anywhere within a single pixel, or a series of pixels depending on the quality of the intensity data. But at a minimum, a single pixel height is typically considered the best achievable accuracy. While pixel height is a finite value, accuracy is really a relative term – it depends on test setup and configuration, like that shown in Table 3-8. As the source-to-object distance increases, accuracy inherently gets worse because fewer pixels are being used to describe the same diameter (reference Tests 1 thru 4). It follows that at the same source-to-object distance, accuracy inherently

gets better as the diameter increases because more pixels are being used to describe the larger diameters (reference Tests 8 thru 11).

Table 3-8 Accuracy Relative to Test Setup

Test	*SOD** (in)	Actual Diameter (in)	Magnified Diameter (in)	Single Pixel Height (in)	Single Pixel Percentage of Magnified Diameter
1	10.5	0.180	0.539	0.0039	0.72%
2	15	0.180	0.387	0.0039	1.01%
3	22	0.180	0.289	0.0039	1.35%
4	26.25	0.180	0.238	0.0039	1.64%
5	26.25	0.180	-	0.0039	-
6	26.25	0.180	0.242	0.0039	1.61%
7	26.25	0.180	-	0.0039	-
8	26.25	0.344	0.496	0.0039	0.79%
9	26.25	0.508	0.730	0.0039	0.53%
10	26.25	0.672	0.965	0.0039	0.40%
11	26.25	0.836	1.188	0.0039	0.33%

* Values include 1.5 inches for submerged point source location.

Tests 1 thru 4 investigated how varying the x-ray source-to object distance (*SOD*) and the object-to-detector distance (*ODD*) affects the measured diameter results. When the object is closer to the source, the feature in the intensity data appears larger, like that shown on the right-hand side of Figure 3-11. Moving the object further from the source should reduce the number of pixels between the edges of the feature. Note that the left plot in Figure 3-11 is un-edited and shows the overlapping feature around the center of the frame. The intensity curves were shifted to show them clearly in the right plot.

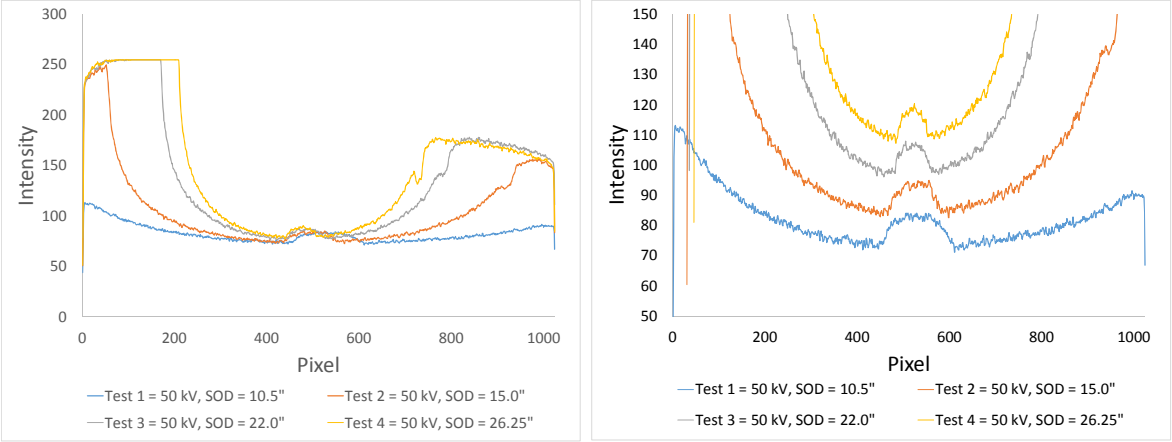

Figure 3-11 Increasing Source-to-Object Distance in Static Tests 1 thru 4

Tests 5 thru 7 investigate how varying kV value affects the measured diameter results. Figure 3-12 illustrates how too little power or too much power will both result in no contrast and thus no feature to measure. Note that Test 4 is included in this analysis because it was at the same test configuration as the other three tests.

The Actual Magnification Factor for Test 6 was plotted with the results from Tests 1 thru 4 in Figure 3-13. Because Test 6 is in good agreement with the results from Tests 1 thru 4, there is confidence that kV value does not have a significant impact on the diameter measurement method; this of course assumes that there is sufficient kV to penetrate the object but not so much as to saturate the detector.

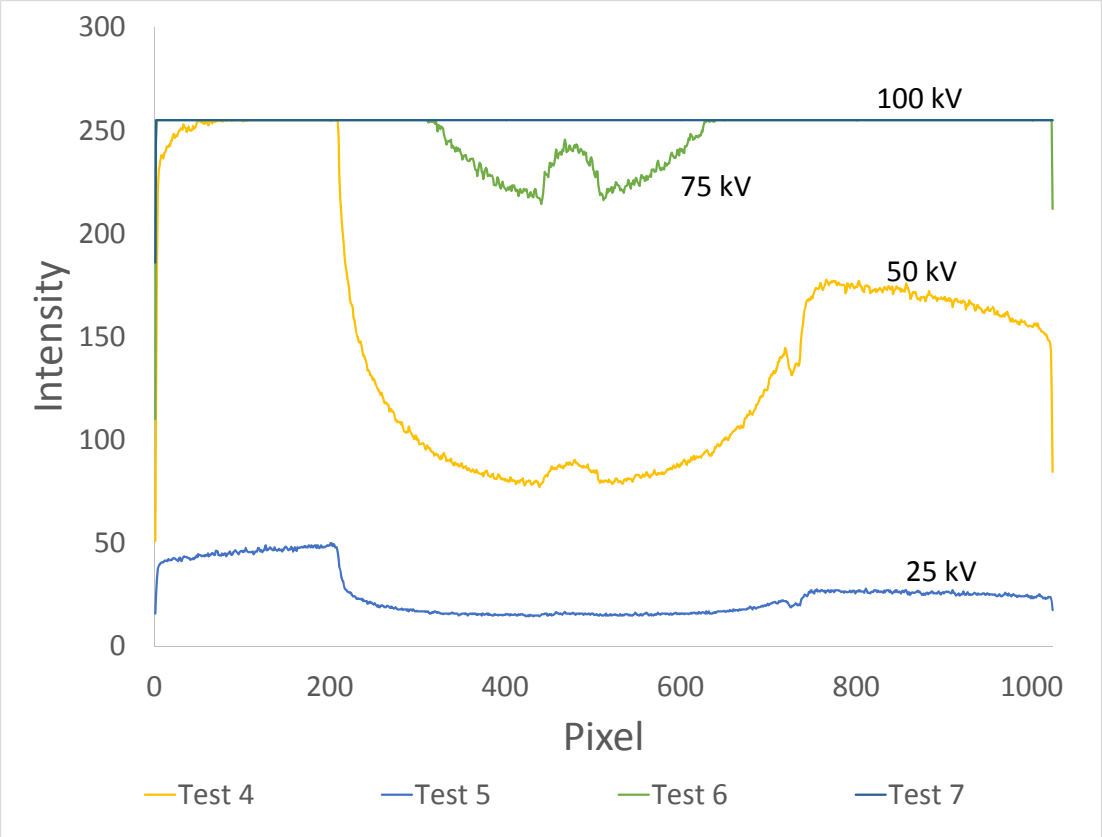

Figure 3-12 Changing kV Value for Static Tests 4 thru 7

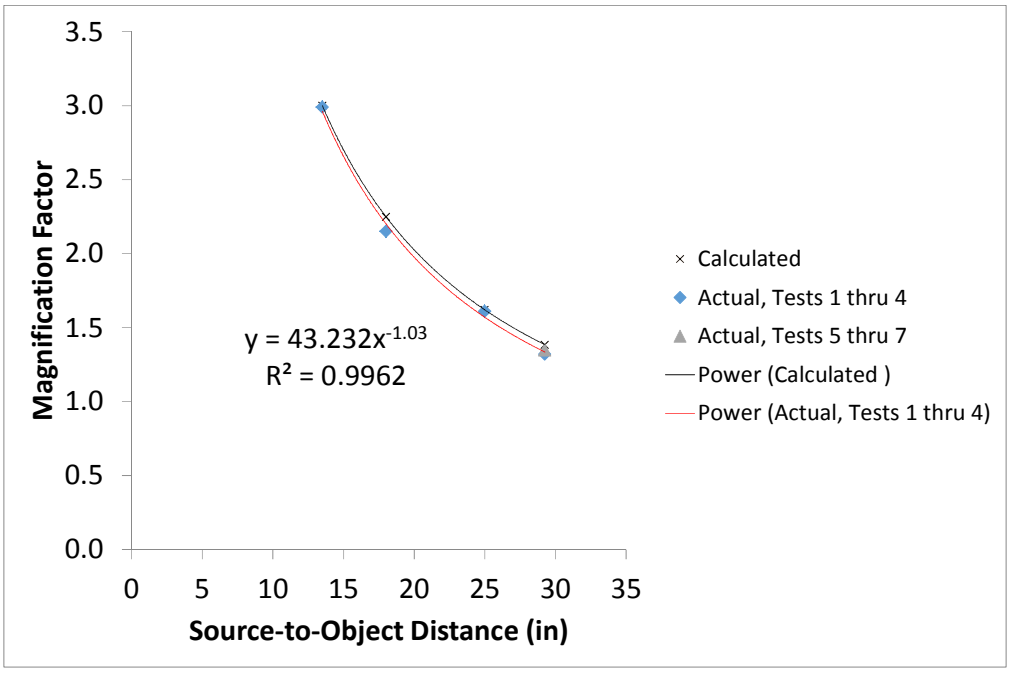

Figure 3-13 Calculated versus Actual Magnification Factor for Static Tests 1 thru 7

Finally, Tests 8 thru 11 were conducted to investigate if changing the diameter (in a static environment and at the same test configuration) affected the magnification factor. Figure 3-14 shows the four diameters that were measured for these tests. It makes sense that the intensity depth is the same for all tests because all were tested at 50 kV. The actual magnification factor was consistent from diameter to diameter; as shown in Figure 3-15.

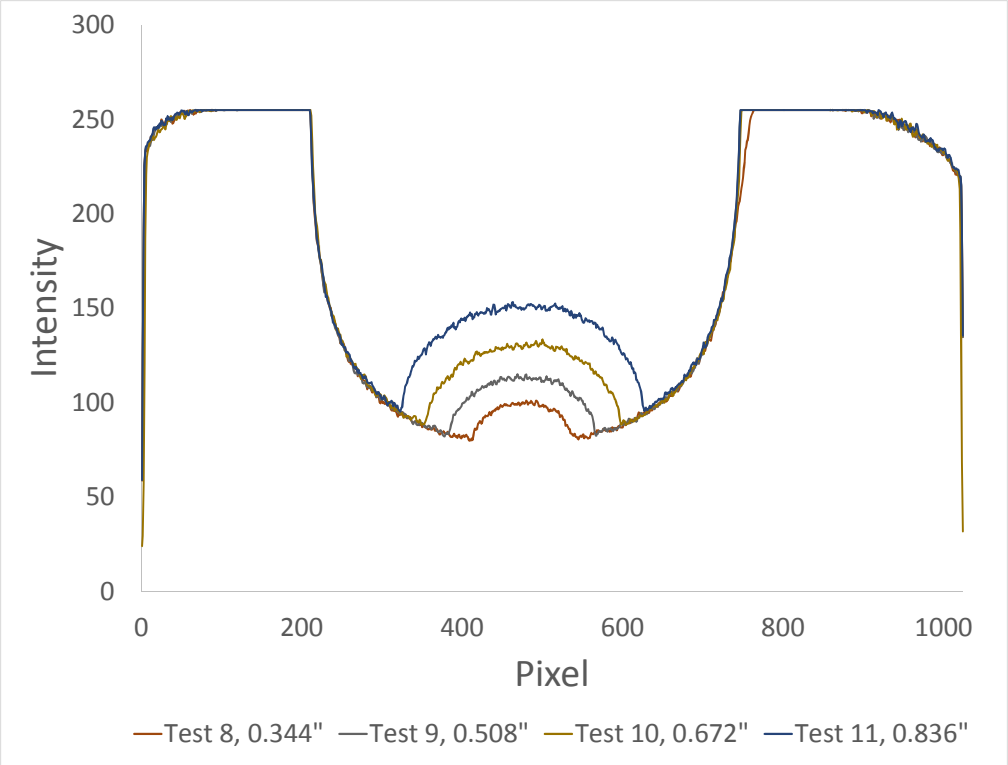

Figure 3-14 Increasing Diameter at the Same Source-to-Object Distance for Tests 8 thru 11

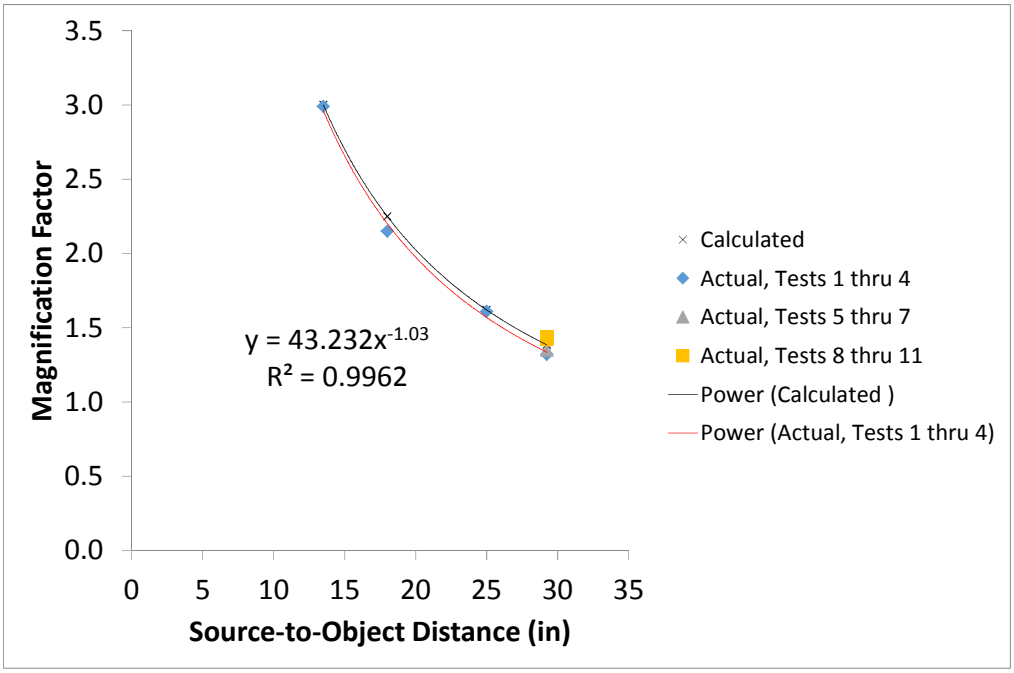

Figure 3-15 Calculated versus Actual Magnification Factor for Static Tests 1 thru 11

At the conclusion of static testing, the power curve shown in Figure 3-15 was used to estimate the actual magnification factor to be used in dynamic testing. Source-to-object distance for all dynamic tests is 23.25 inches (excluding the point source submerged distance). Accounting for the 4.5 inches of submerged distance, the predicted magnification factor for dynamic testing should be about 1.4.

Images were captured with the CCD camera software during static testing. The images and their corresponding intensity plots for each static test are provided in the following figures. In the x-ray image, the vertical black line indicates the location of the intensity data. In the intensity plots, the orange line is the raw intensity and the blue line is the normalized intensity. Normalized intensity is found by dividing every pixel in the frame by an average pixel value (APV). The APV was chosen manually for each static test. The vertical black lines in the intensity plots indicate the diameter edges, found per the process described in Section 3.2.

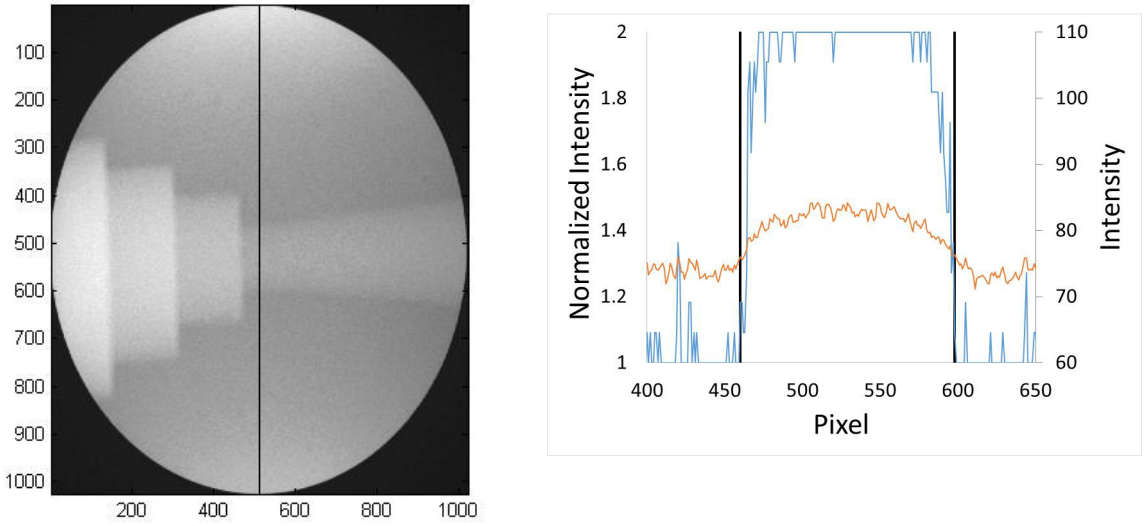

Figure 3-16 Static Test 1 (APV = 52)

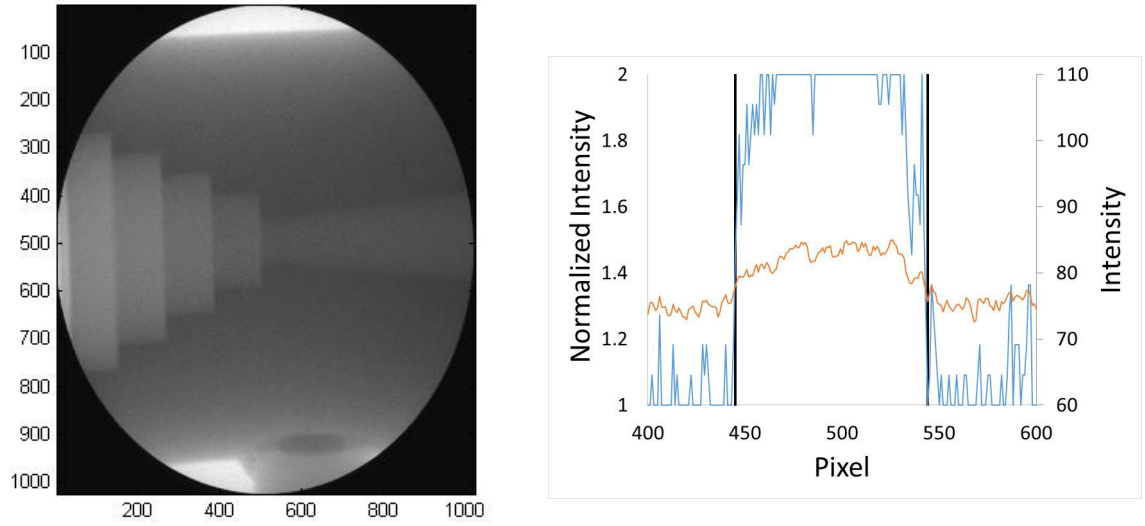

Figure 3-17 Static Test 2 (APV = 52)

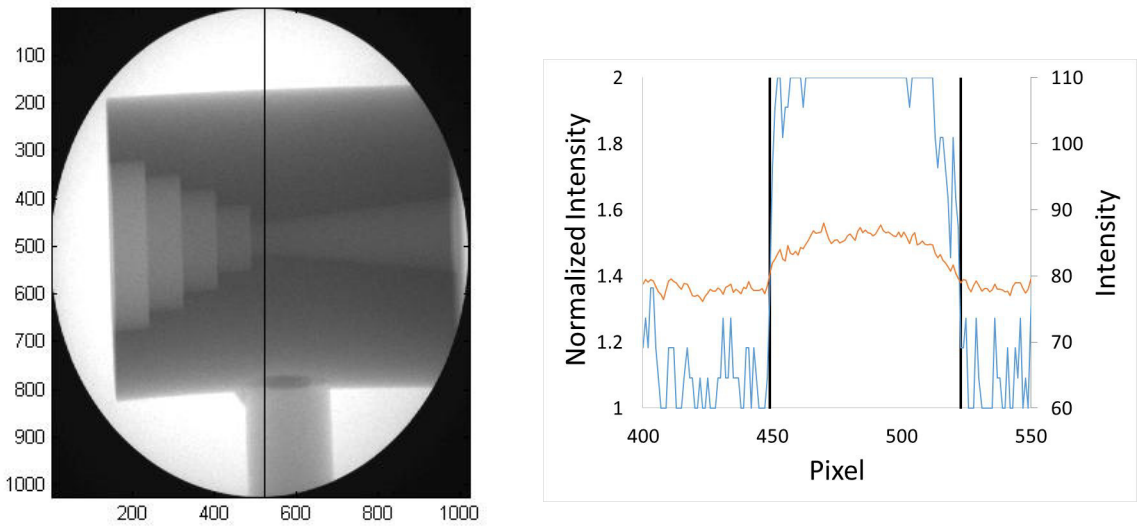

Figure 3-18 Static Test 3 (APV = 54)

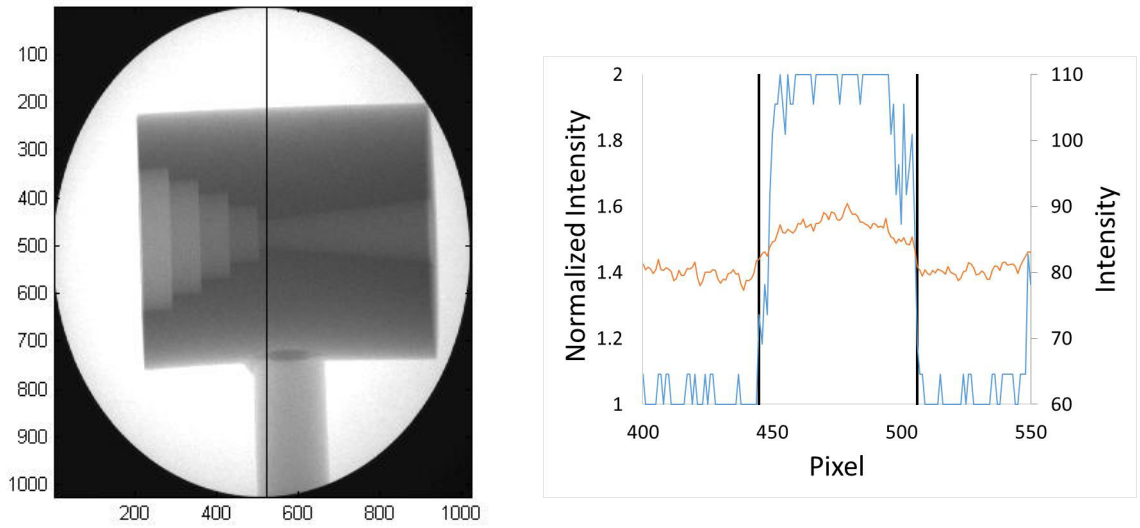

Figure 3-19 Static Test 4 (APV = 56)

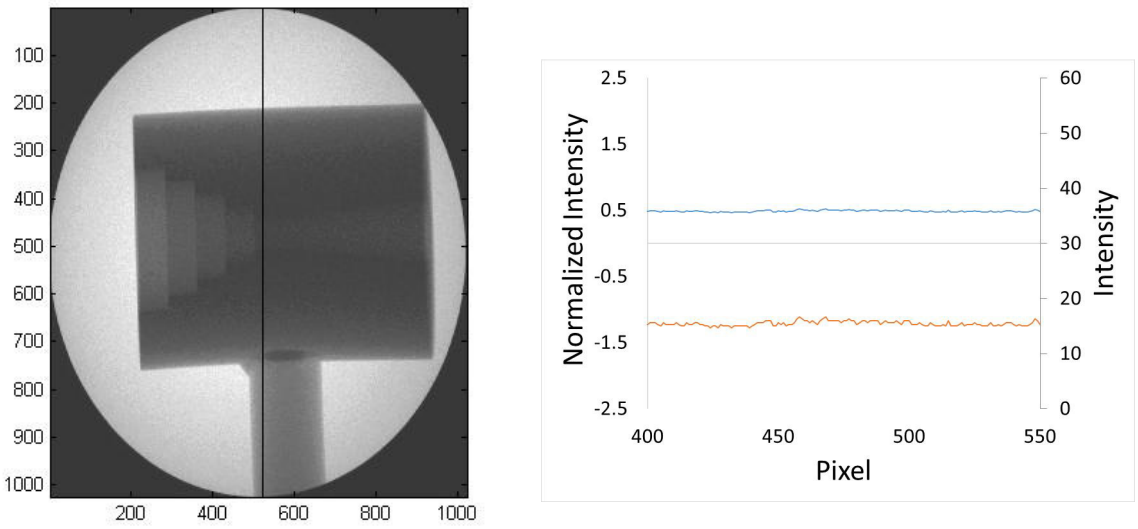

Figure 3-20 Static Test 5 (APV = 32)

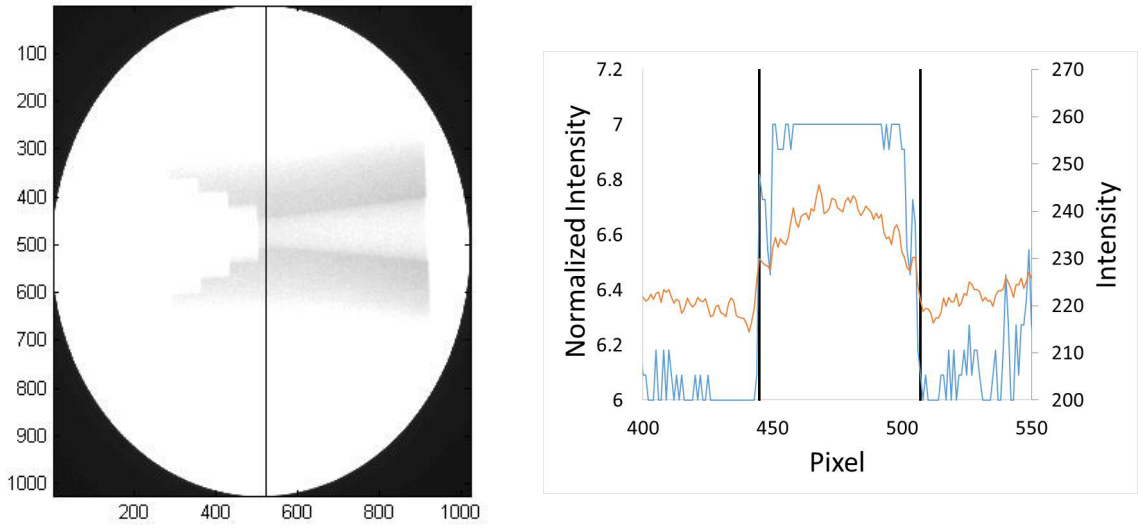

Figure 3-21 Static Test 6 (APV = 35)

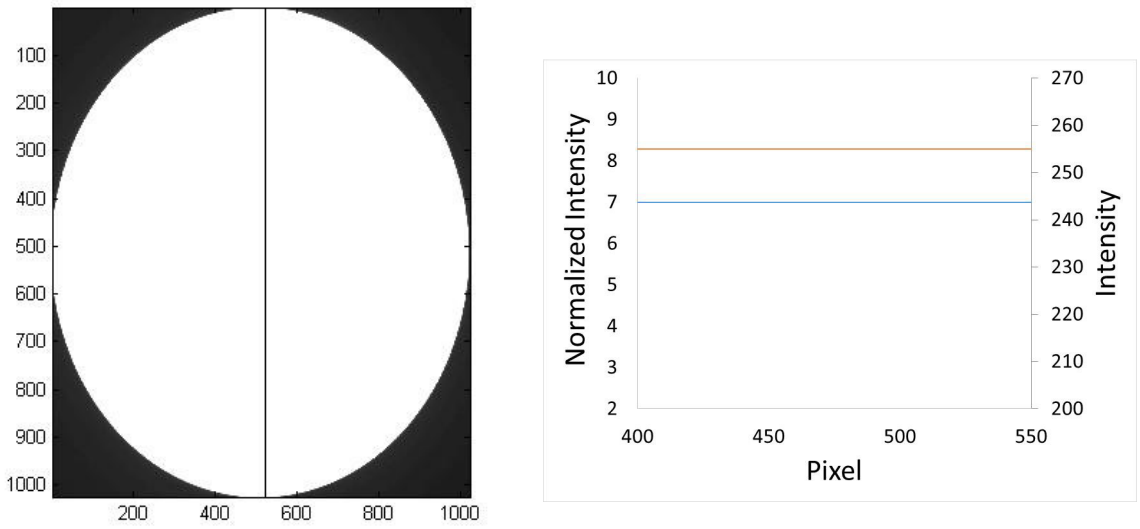

Figure 3-22 Static Test 7 (APV = 35)

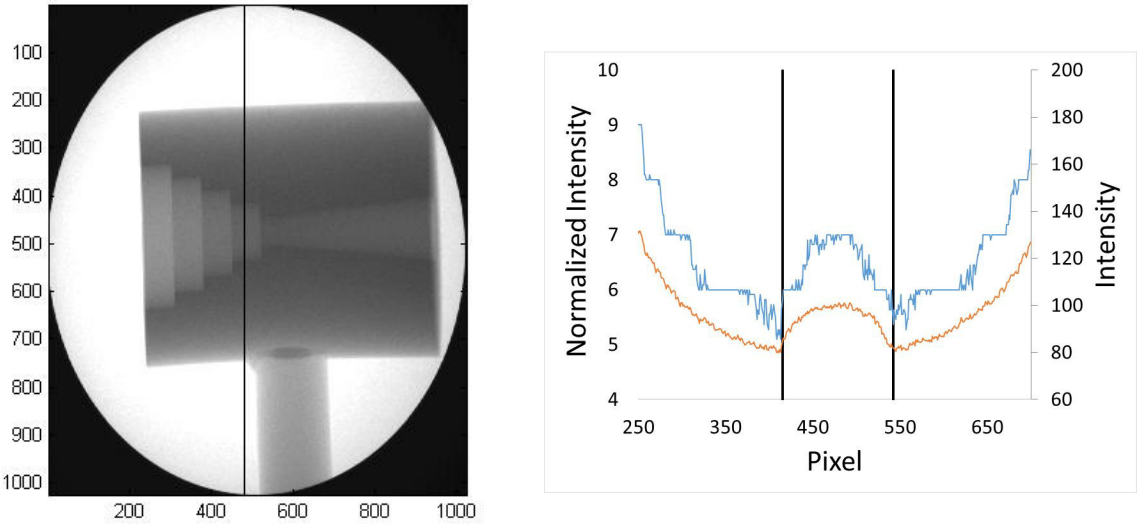

Figure 3-23 Static Test 8 (APV = 15)

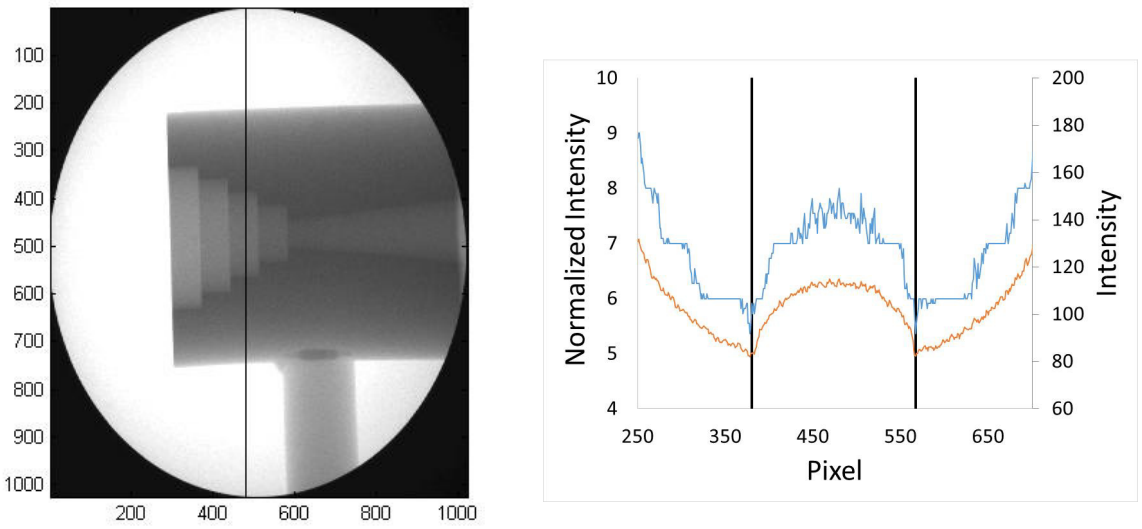

Figure 3-24 Static Test 9 (APV = 15)

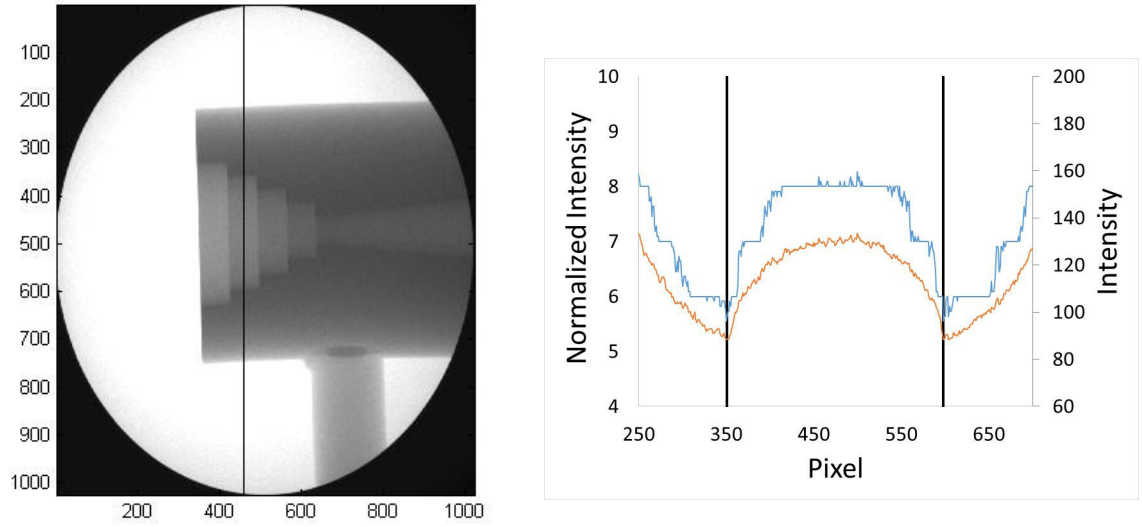

Figure 3-25 Static Test 10 (APV = 16)

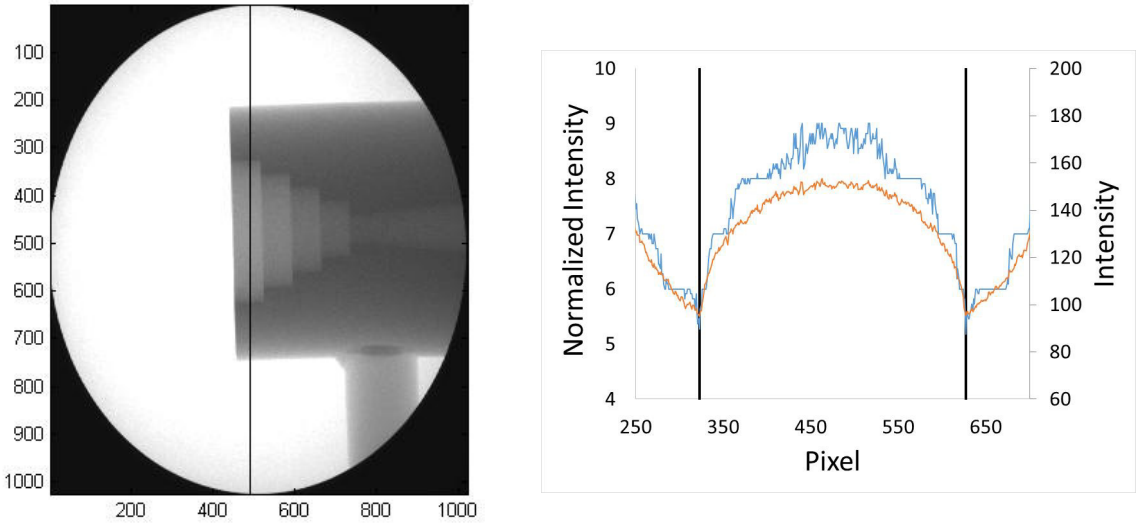

Figure 3-26 Static Test 11 (APV = 18)

3.3.4.2 Dynamic Calibration

The tests in the Dynamic Calibration Test Matrix were completed November 6, 2014 in the UAH X-Ray Facility. Results are shown in Table 3-9. The source-to-object distance and the object-to-detector distance were measured with a tape measure, from the front face of the x-ray tube to the mid-section of the calibration standard and from the mid-section of the calibration standard to the from face of the image intensifier, respectively. The calculated magnification factor (M.F.) was then calculated with these distances according to Equation (1-10).

The Actual M.F. was determined during post-test analysis for each test. Ten, equally spaced frames were extracted from each video file and the edge detection process (described in Section 3.2) was performed in each frame. The error between the measured

diameter and the actual diameter was then driven to zero by adjusting the magnification factor. The resulting magnification factor is shown as Actual M.F. column in Table 3-9.

Table 3-9 Dynamic Calibration Results

Test	Video Filename	*SOD** (in)	*ODD* (in)	kV	Target Table Speed (in/s)	Estimated M.F.**	Actual M.F.
1	20141106_002.avi	27.75	12.75	50	0.1	1.4	1.345
2	20141106_003.avi	27.75	12.75	50	0.1	1.4	1.388
3	20141106_004.avi	27.75	12.75	50	0.3	1.4	1.346
4	20141106_005.avi	27.75	12.75	50	0.3	1.4	1.280
5	20141106_006.avi	27.75	12.75	50	0.5	1.4	1.367
6	20141106_007.avi	27.75	12.75	50	0.5	1.4	1.368

* Values include 4.5 inches for submerged point source location
**Estimated Magnification Factor was estimated at the conclusion of Static Calibration Testing. Reference Section 3.3.4.1.

Actual magnification factors for all dynamic tests were just below the estimated value. Figure 3-27 shows the 10 captured frames from Test 1. These images were captured via the Debut Video Capture Software. They are provided to show the calibration standard moving past the center of each frame. The black, vertical line represents where the intensity data was extracted from for analysis. Intensity plots are shown in Table 3-10. There is also a black square in the first frame, just below center. This area represents the area of pixels that are averaged. The same area is averaged on all subsequent frames.

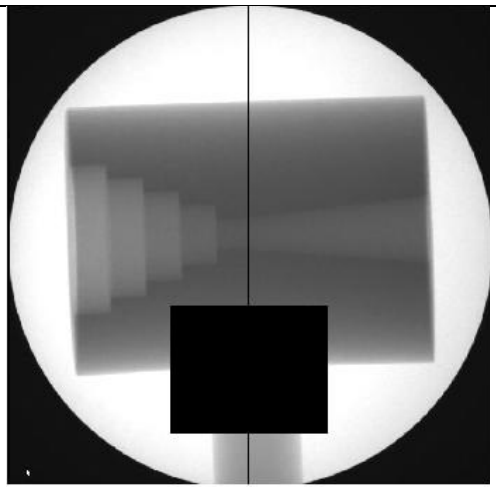

Frame 239

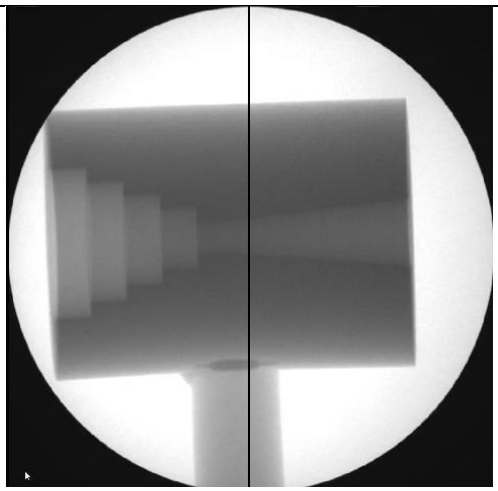

Frame 277

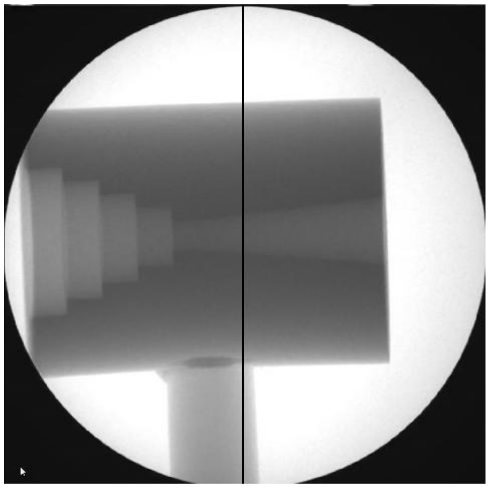

Frame 315

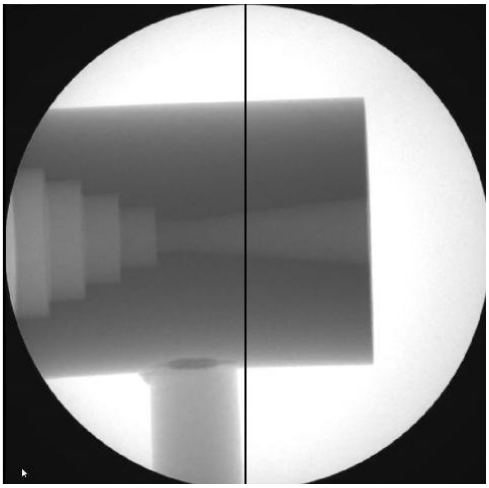

Frame 353

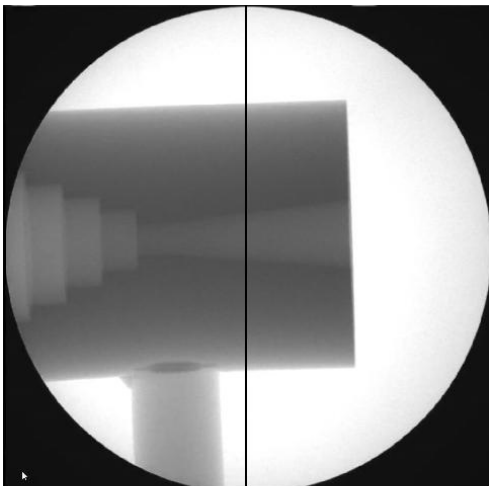

Frame 391

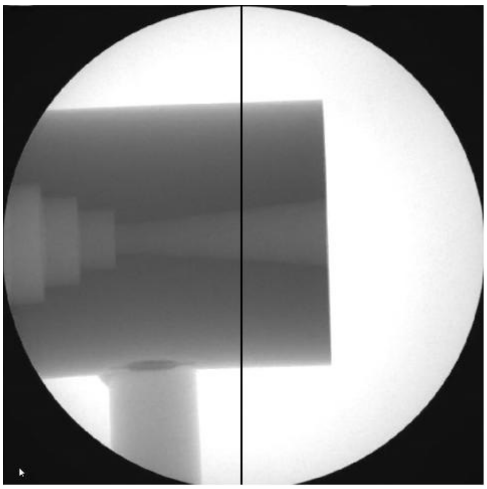

Frame 429

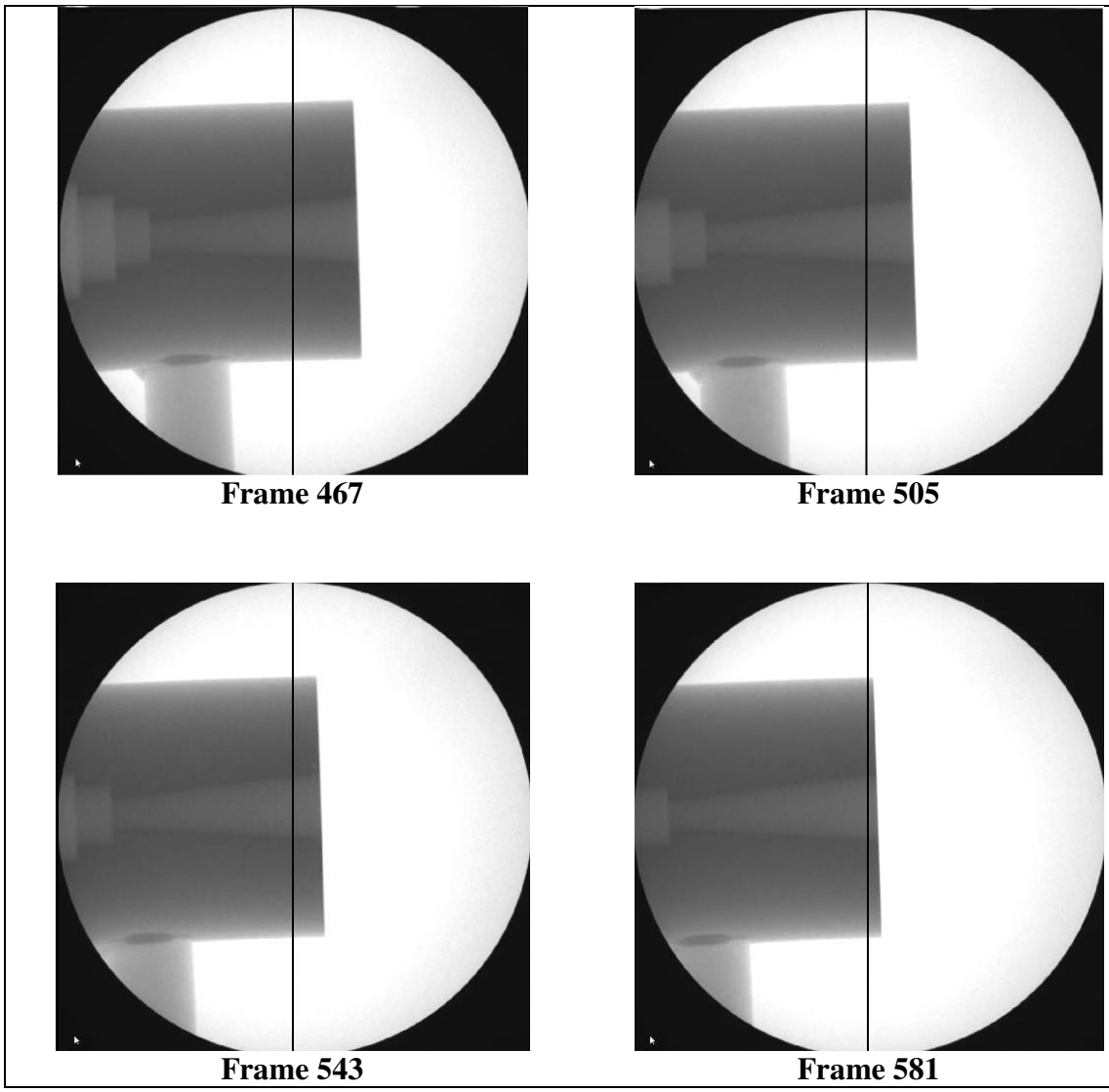

Figure 3-27 Dynamic Test 1 Screen Shots (10 Frames)

Intensity plots that correspond to the Test 1 screen shots are provided below. Note that the vertical, black lines were found using the edge detection method discussed in Section 3.2. The orange line is the raw intensity and the blue line is the normalized intensity. Normalized intensity is found by dividing every pixel in the frame by an average pixel value; frame number and corresponding APV is listed under each frame. Frame 239 in Figure 3-27 shows a black box just below the center of the picture; this is the pixel area

that was averaged for Frame 239 and all subsequent frames. Recall that this area was selected because it consisted of a combination of white space and lighter shades of gray that are not near the inside diameter of the standard. Notice that the average pixel value increases as the calibration standard moves out of view; this is because the rod that the calibration standard is attached to is also moving out of view of the pixel area, adding more white space to the area. This results in a net increase in intensity and thus a higher average pixel value for that frame.

Table 3-10 Dynamic Test 1 Intensity Plots

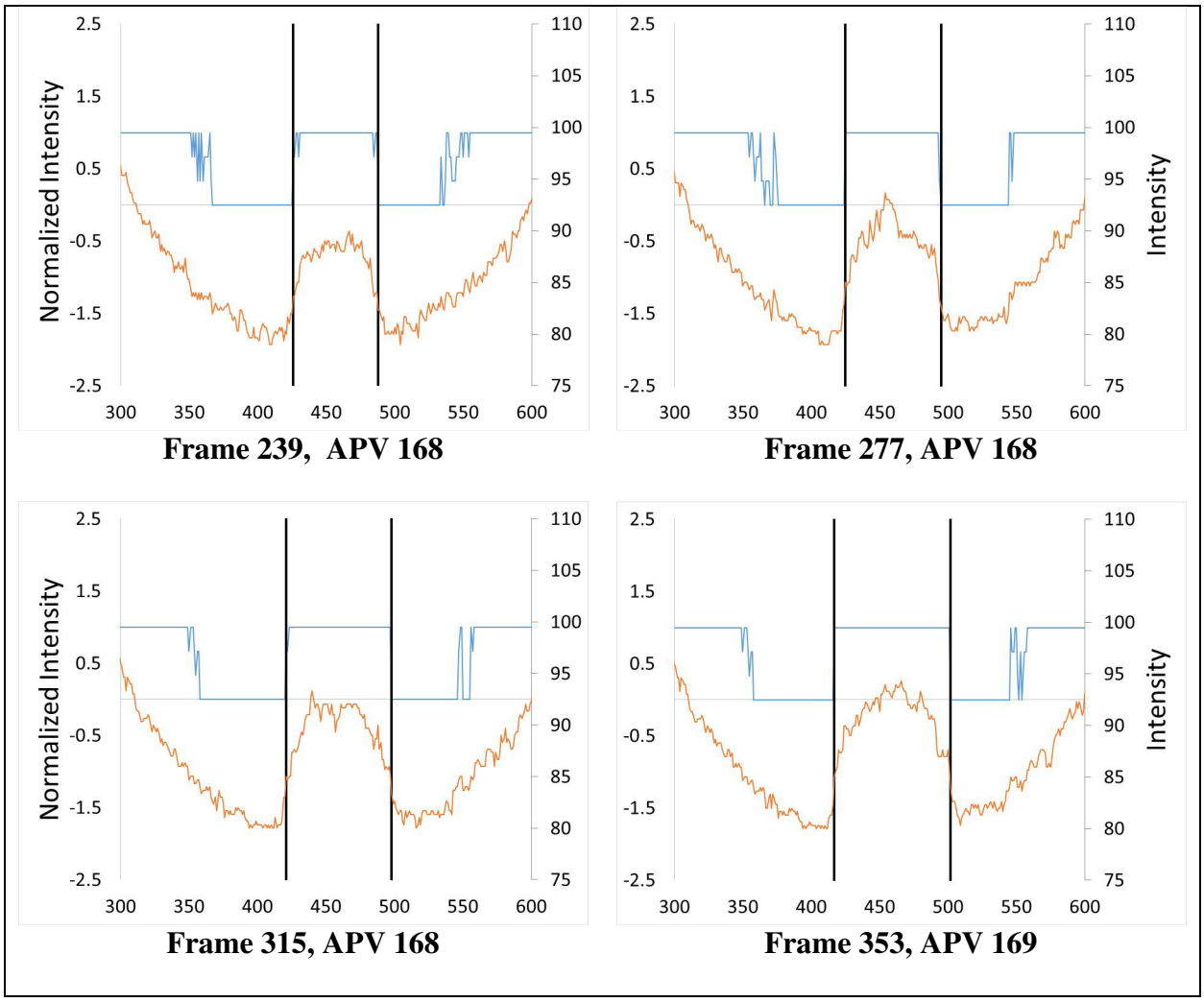

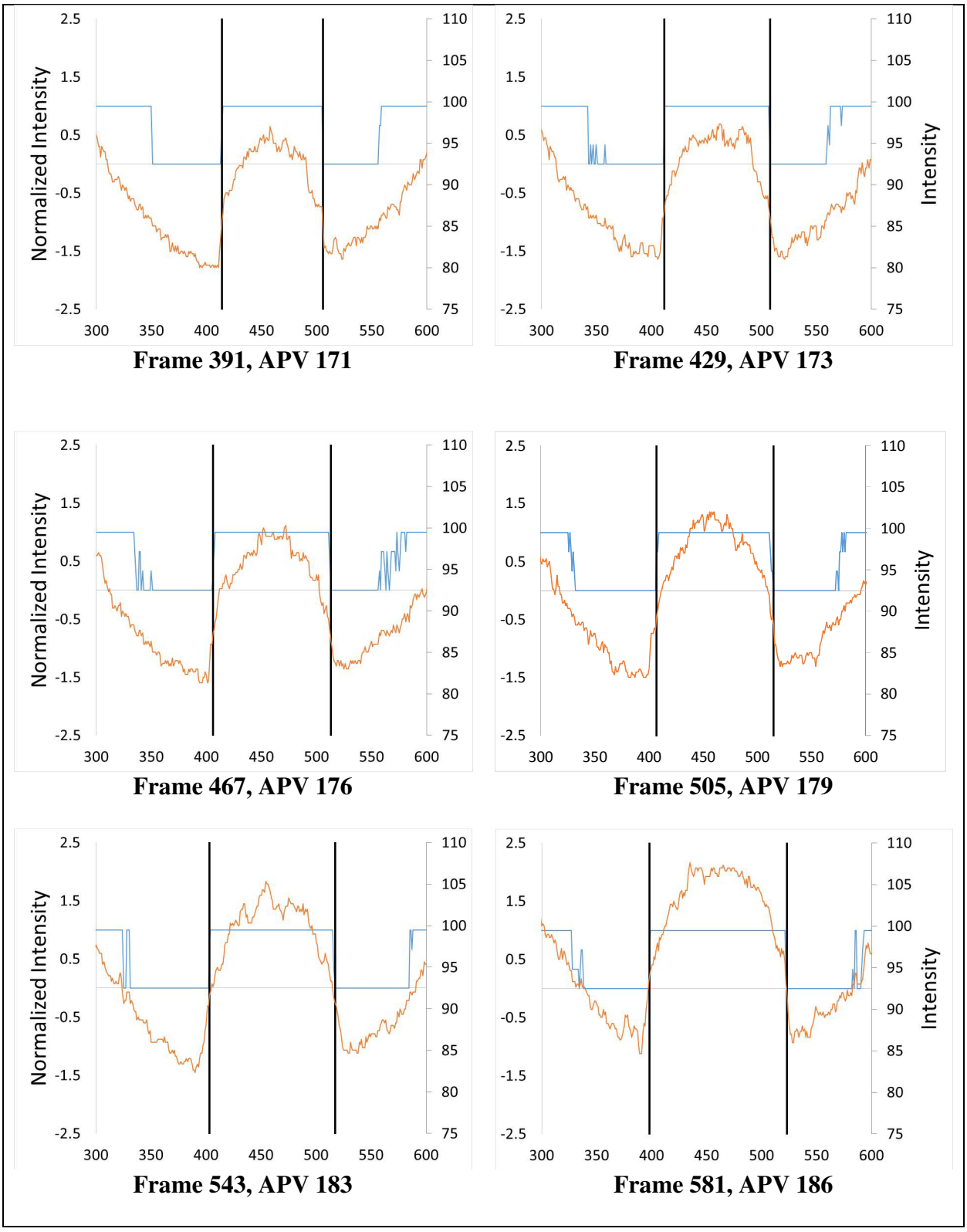

Frame 391, APV 171

Frame 429, APV 173

Frame 467, APV 176

Frame 505, APV 179

Frame 543, APV 183

Frame 581, APV 186

The following figures show the as-measured diameters versus the actual diameter for each series of tests. Ten frames from each video file were extracted and analyzed. The first frame was always used to determine the actual magnification factor, which was then applied to the diameter measurements in the rest of the frames. That is why the first data point is on the true position in each series of tests.

The data shows good correlation to the actual diameter for the 0.1 and 0.3 in/s tests. Notice in Figure 3-28 that the data points between both tests are very close to each other from frame to frame. This is an indication that table speed was consistent between the two tests (measured at about 0.08 in/s). The table speed between the 0.3 in/s tests was not as consistent – Test 3 obviously ran slower at 0.34 in/s while Test 4 ran at 0.37 in/s. Table speed was consistent in the 0.5 in/s tests. The minimum and maximum error for each table speed is shown. A +6% / -7% error encompasses all dynamic test results, as shown in Figure 3-31.

A bias is observed, which is most prominent in the 0.5 in/s tests. Notice in Figure 3-30 that the measured diameter results dip down below the actual diameter at 0.5 inches along the calibration standard. The data then runs parallel to the actual diameter. This required further investigation of the edge detection method. It was observed that the method tends to select edges narrower than what the human eye might select – this is more prevalent at the larger diameters in the calibration standard, which would explain the dip below the actual diameter. In Table 3-10 for example, in frames 505 and 543, the human eye would likely select edges wider than those selected by the edge detection method (noted by the

vertical black lines). This behavior can be attributed to the selection of the average pixel value area and the subsequent average pixel value. It was observed that small changes in the APV could have a significant effect on the shape of the normalized curve. This is important because the inside diameter edge is located on the normalized curve.

Frame 505 from dynamic Test 1 was selected for APV analysis where the frame was divided by multiple values of APV to see how the normalized curve changed. Refer to Appendix E for the intensity plots.

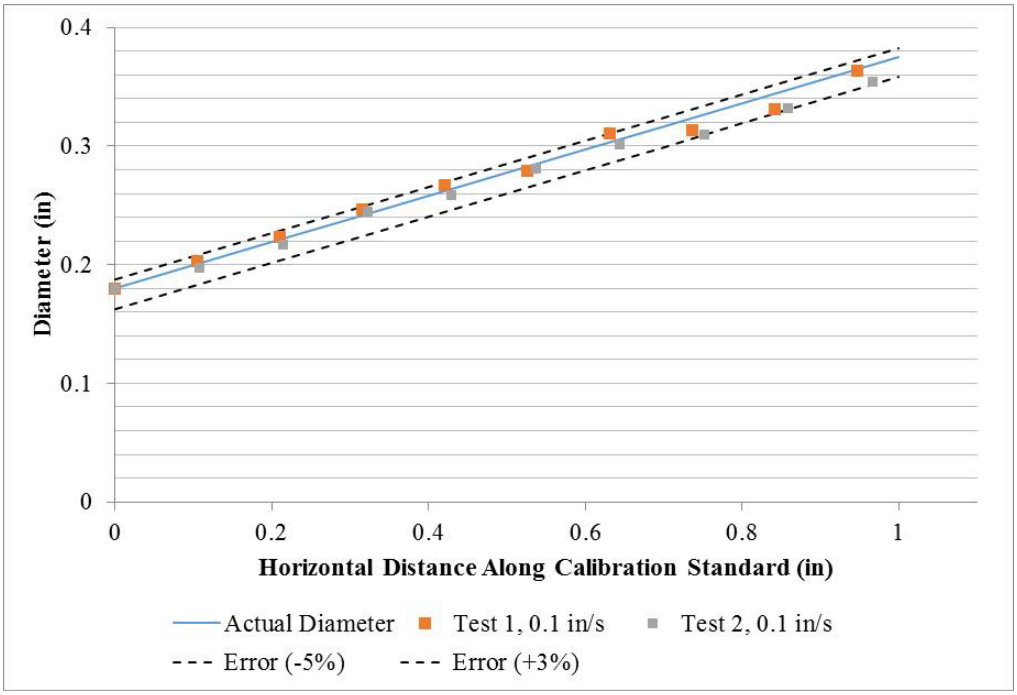

Figure 3-28 Dynamic Tests 1 and 2, 0.1 in/s

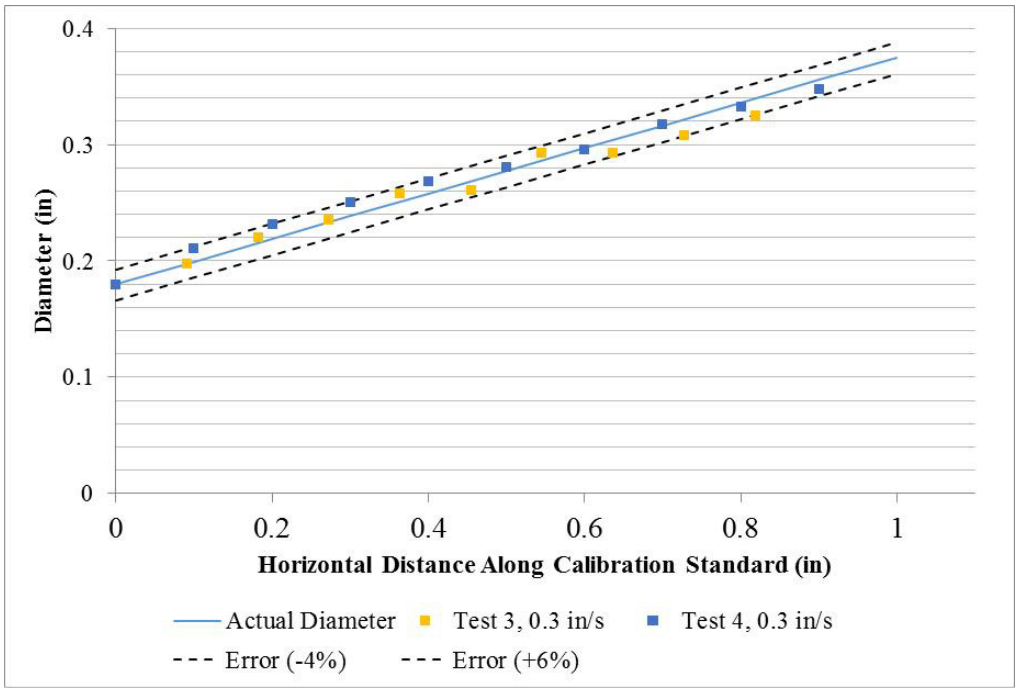

Figure 3-29 Dynamic Tests 3 and 4, 0.3 in/s

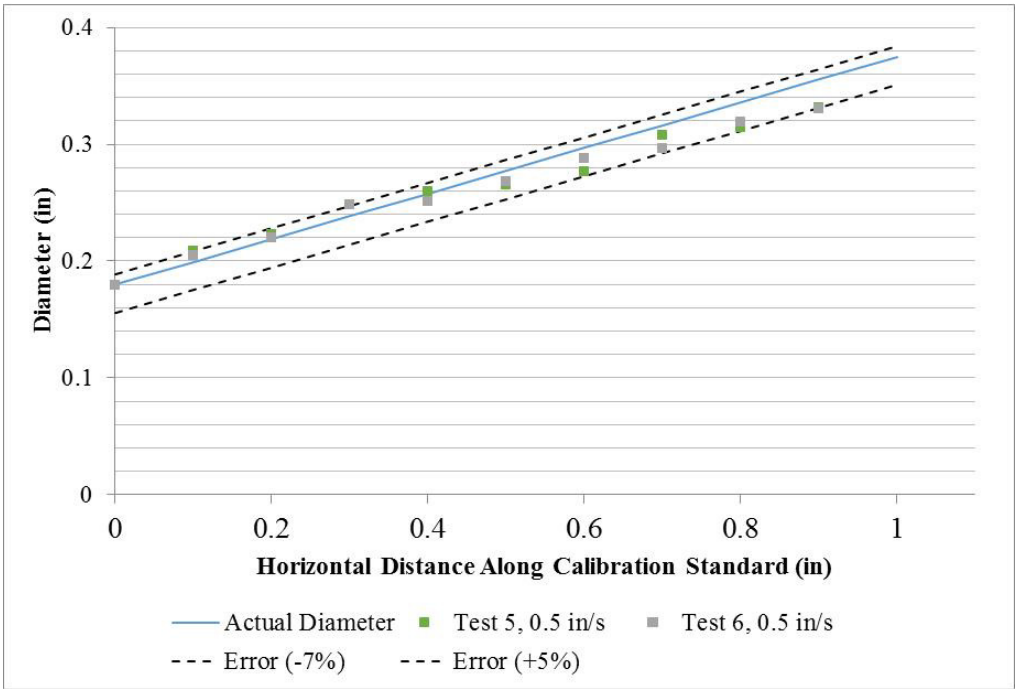

Figure 3-30 Dynamic Tests 5 and 6, 0.5 in/s

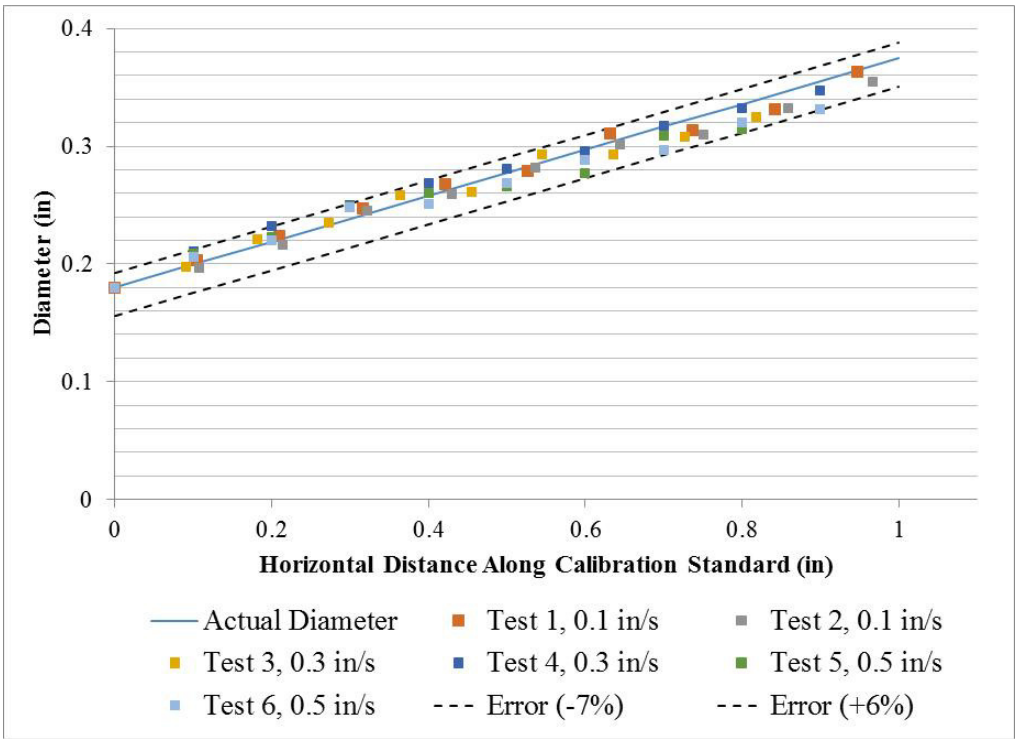

Figure 3-31 All Dynamic Tests

Figure 3-32 is provided to show how the dynamic magnification factors relate to the static magnification factors, discussed in Section 3.3.4.1. The static curve is useful for estimating dynamic magnification factors.

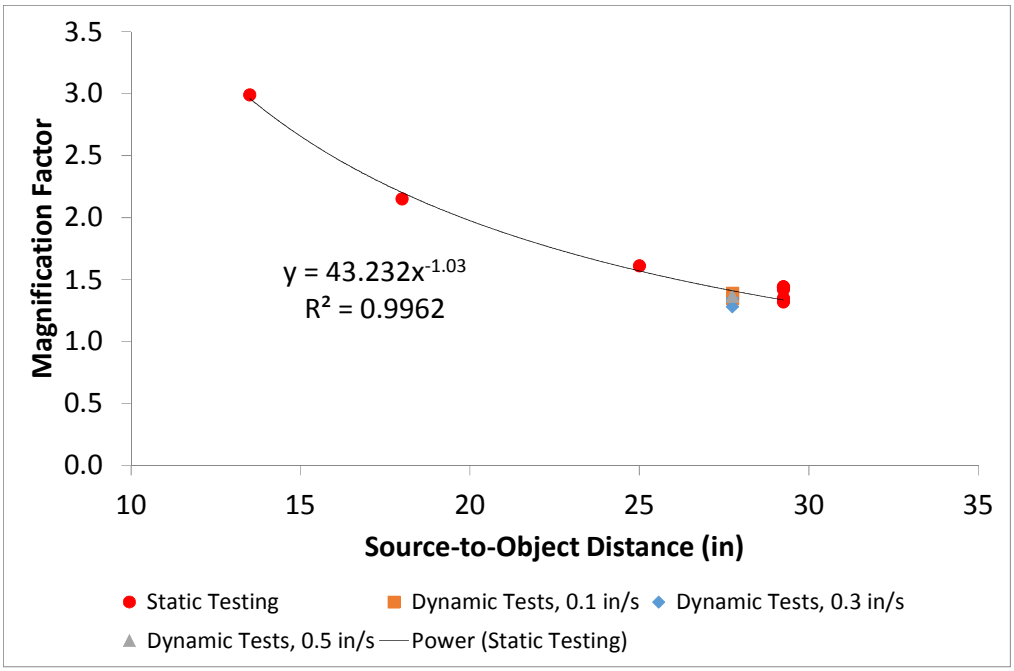

Figure 3-32 Static and Dynamic Magnification Factors

Throughout static and dynamic x-ray testing, several items were identified as factors that influence measurement accuracy. Most of these items were discussed throughout Chapter 3. A discussion of each is provided here in bullet form. They are listed in no particular order:

1. Magnification Factor
    a. The point source in the x-ray tube head is submerged 4.5 inches. This value should be added to the measured source-to-object distance.
    b. Depending on the application, a magnification factor measured in a static environment may be acceptable for use in a dynamic test.

2. Average pixel value (APV)
    a. The average pixel value is used in the edge detection method. Each frame is divided by the APV to normalize the data.
    b. It was observed that small changes in the APV could have a significant effect on the shape of the normalized curve (refer to Appendix E). This is important because the inside diameter edge is located on the normalized curve. Preliminary assessment of the APV analysis suggests the APV be held constant from frame to frame (analogous to the magnification factor). Also, instead of selecting a set of arbitrary pixels to average, it may be better if the APV is a user-defined input.
    c. Future work includes optimizing the selection of the APV.
3. CCD camera frame rate
    a. Frame rate was assumed to be 30 frames per second, per the CCD camera specification sheet. Analysis shows this is a good assumption.
    b. Frame rate is important because it affects the table speed measurement.
4. Table speed
    a. Table speed is measured from the x-ray data.
    b. Although there were no indications that an inaccurate table speed was used in the analysis, it is important that there is enough time before the test for the table to accelerate to a constant velocity. It follows that enough time must also be allowed for the table to decelerate to zero after the standard has completely passed the measurement point. Ensuring that

measurements are taken only when the table is moving at constant velocity is important to ensuring accurate measurements during calibration.

5. Difference in intensity noise between image capture softwares
    a. Camera software was used during static testing.
    b. Debut Video Capture software was used during dynamic testing.
    c. Image noise could affect the edge detection method and thus influence measurement accuracy.
    d. A quick assessment was performed to determine if there was a significant difference between the two image capture softwares. Static Test 4 and a frame from dynamic Test 1 were selected for comparison (both frames were taken at 50 kV and were looking at the 0.18" diameter in the standard.) Figure 3-33 reveals no significant difference in intensity noise between the two image capture softwares.

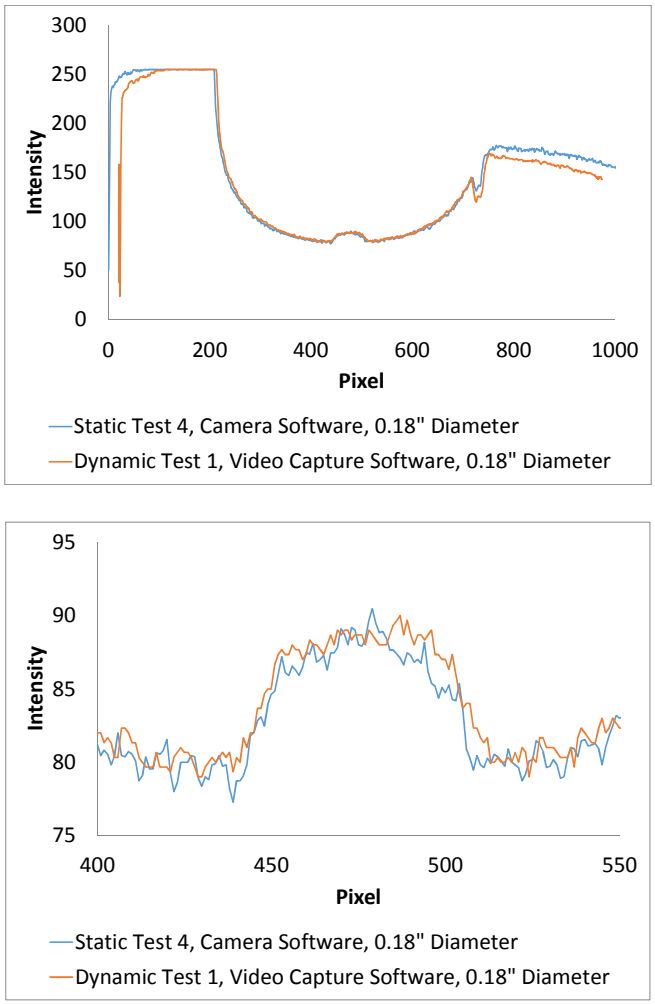

Figure 3-33 Noise Comparison between Camera Software and Video Capture Software

CHAPTER 4

Conclusions

Throat erosion in a solid rocket motor causes the nozzle throat diameter to increase during operation, resulting in reduced performance. In order to correlate throat erosion rate to other parameters, it is first necessary to know what the throat diameter is throughout a motor burn. Thus, an indirect method and a direct method for determining throat diameter in a solid rocket motor were investigated in this thesis. Both methods prove feasible.

The indirect method looked at the use of pressure and thrust data to solve for throat diameter as a function of time. Because the thrust coefficient is a function of the nozzle throat diameter, the throat diameter must be found iteratively. The results of the indirect method were used to correlate a ballistics model to G138 test data. The ballistics model was within 10% of all measured and calculated performance parameters (e.g. average pressure, specific impulse, maximum thrust, etc.) for tests with throat erosion and within 6% of all measured and calculated performance parameters for tests without throat erosion. It is important to note that the throat erosion rate equation developed in Chapter 2 is limited by the pressure range that the test data covered. The analyst must understand

that this limitation exists and must take it into account when generating pressure and thrust predictions. The indirect method's proof of concept was shown by the good agreement between the ballistics model and the test data.

The direct method involves the use of x-rays to directly observe a simulated nozzle throat erode in a dynamic environment. A process was developed for calibrating and extracting the diameter dimensions from the x-ray intensity data. Static tests were conducted first with calibrated internal diameter cylinders to determine if different features of the test setup affected measurement results. Source-to-object distance, kV value, and diameter size were investigated. The importance of the magnification factor was realized during static post-processing.

Following static tests, dynamic tests were conducted at three different horizontal translation speeds to determine if motion or the quickness of an event affected the accuracy. Although table speed has been identified as a factor that contributes to measurement accuracy, there were no indications that inaccurate table speeds were used in the analysis. It is therefore concluded that any measurement inaccuracy – that exists because of the motion or quickness of an event – is negligible. This only holds for the speeds tested in this thesis. Other factors that affect measurement accuracy are the magnification factor, average pixel value, and CCD camera frame rate. All dynamic test results were within +6% / -7% of the actual diameter. The reason for this level of inaccuracy is likely due to the bias in the edge detection method. It was observed that the method tends to select edges narrower than what the human eye might select on the

normalized intensity plot– this behavior is more prevalent at the larger diameters in the calibration standard. A preliminary assessment revealed that the shape of the normalized curve – which is where the edges are located – is very sensitive to the average pixel value. To mitigate the influence of average pixel value, it may be more appropriate to hold it constant from frame to frame (analogous to the magnification factor). Also, instead of selecting a set of arbitrary pixels to average, it may be better if the average pixel value is a user-defined input. Future work is to develop a correlation between average pixel value and actual diameter and to determine the effects of source-to-object distance, kV value, and other parameters on that correlation. Following that analysis, the dynamic tests would be analyzed again, holding the average pixel value constant from frame to frame to see if the accuracy of the edge detection method improves.

Appendix A

St. Robert's Law

Propellant burn rate is a function of chamber pressure and initial propellant bulk temperature. An increase in either of these parameters results in a faster burn rate and consequently a shorter burn duration. Propellant vendors typically provide burn rate information in the form of St. Roberts' Law:

$$\dot{r} = aP_c^{\,n} \tag{A-1}$$

In addition to the temperature coefficient and the burning rate exponent, the propellant vendor might also provide propellant temperature sensitivity coefficients. In the case of the G138 motor, a temperature sensitivity coefficient (σ_p) is provided in the motor specification sheet. According to Sutton [28], σ_p expresses the percent change of burning rate per degree change in propellant temperature at a particular value of chamber pressure. Equation (A-2) describes this relationship:

$$\boldsymbol{\sigma_p = \left(\frac{\delta \ln \dot{r}}{\delta T}\right)_p = \frac{1}{\dot{r}}\left(\frac{\delta \dot{r}}{\delta T}\right)_p} \quad \textbf{(A-2)}$$

Because of the burn rate's dependence on the propellant temperature, it is desirable to incorporate σ_p into Equation (A-1). The following derivation shows this process. First the variables in Equation (A-2) are separated.

$$\boldsymbol{\sigma_p \delta T = \frac{1}{\dot{r}}\, \delta \dot{r}} \quad \textbf{(A-3)}$$

Both sides are integrated and evaluated. Burn rate ($\dot{r}$) is re-written.

$$\boldsymbol{\int_{T_0}^{T_f} \sigma_p \delta T = \int_{\dot{r}_0}^{\dot{r}} \frac{1}{\dot{r}}\, \delta \dot{r}} \quad \textbf{(A-4)}$$

$$\boldsymbol{\sigma_p\left(T_f - T_0\right) = \ln \frac{a {P_c}^n}{a_0 {P_c}^n}} \quad \textbf{(A-5)}$$

Because the relationship in Equation (A-3) holds for a constant value of chamber pressure, the P_c^n terms in Equation (A-5) cancel, yielding:

$$\boldsymbol{a = a_0 e^{\sigma_p (T_f - T_0)}} \quad \textbf{(A-6)}$$

Substituting this new temperature coefficient (a) into Equation (A-1) yields:

$$\dot{r} = P_c^n a_0 e^{\sigma_p (T_f - T_0)} \quad \textbf{(A-7)}$$

Equation (A-7) is used in the ballistics model to calculate burn rate at each time step. The burn rate is integrated to determine burn distance at each time step. The burn distance is used to approximate propellant surface area at each time step. Once all of this information is known, chamber pressure is calculated at each time step.

Appendix B

Web versus Area Relationship

Understanding how much propellant surface area is exposed throughout a motor burn is essential to a good chamber pressure and thrust prediction. It can be seen from Equation (B-1), that chamber pressure is proportional to surface area:

$$P_c \propto (A_b)^{\frac{1}{1-n}} \tag{B-1}$$

Figure B-1 illustrates chamber pressure dependence on surface area for several values of n. For example, for n equal to 0.50, a 10% increase in surface area results in a 21% increase in chamber pressure.

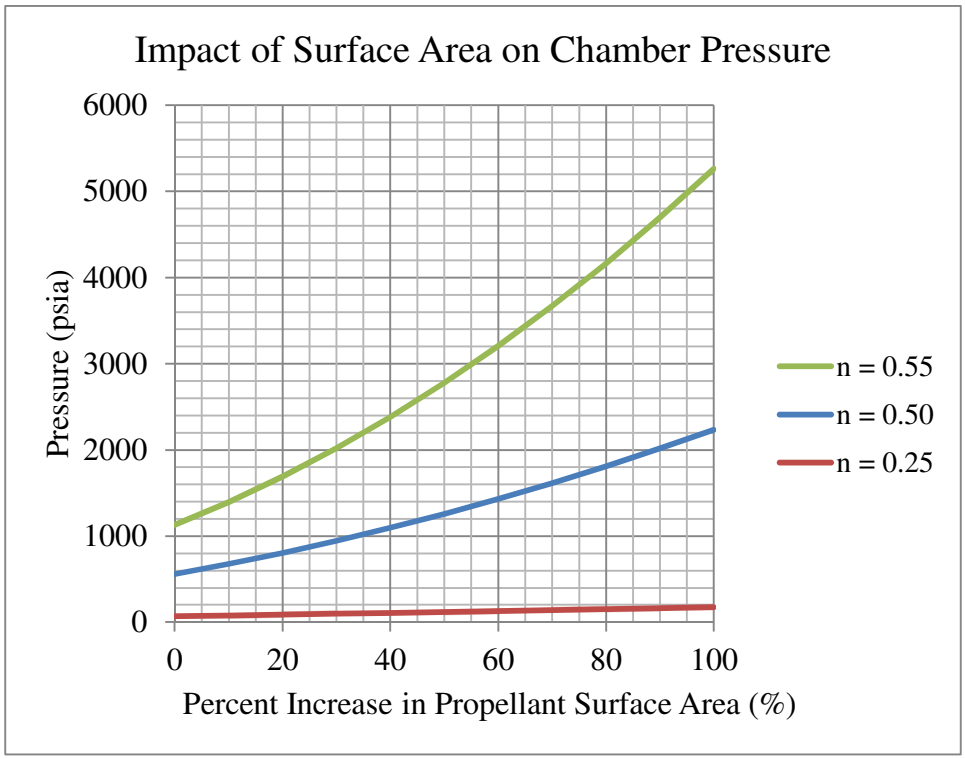

Figure B-1 Impact of Surface Area on Chamber Pressure

Due to the significant impact of surface area on chamber pressure, it is desirable to accurately model surface area in the ballistics model. The analyst initially assumes the propellant surface burns back perpendicularly from all faces, which is a good assumption; it also simplifies the area calculations. Given some initial propellant grain geometry, surface area can then be plotted as a function of web thickness. Sutton [28] best defines web thickness for this application as the minimum thickness of the grain from the initial burning surface (that is, the inner bore diameter) to the case wall. Mathematically, web thickness is given by the following equation:

$$\boldsymbol{r = \frac{D_{OD} - D_{ID}}{2}} \quad \textbf{(B-2)}$$

The propellant grain geometry for the G138 motor is provided in Table B-1.

Table B-1 G138 Grain Geometry

Grain Geometry	Value
Outside Diameter	1.000”
Inside Diameter	0.275”
Length	3.902”
Web (r)	0.363”

Given the assumption that the propellant surface burns back perpendicularly from all faces and given the grain geometry in Table B-1, an ideal web versus surface area is finally plotted in Figure B-2. The shape of this curve is described as progressive; a progressive curve results in an increase in surface area as the propellant web is consumed. Due to the proportional relationship between surface area and chamber pressure, one can rightly expect the chamber pressure prediction to also be progressive (for cases with no throat erosion).

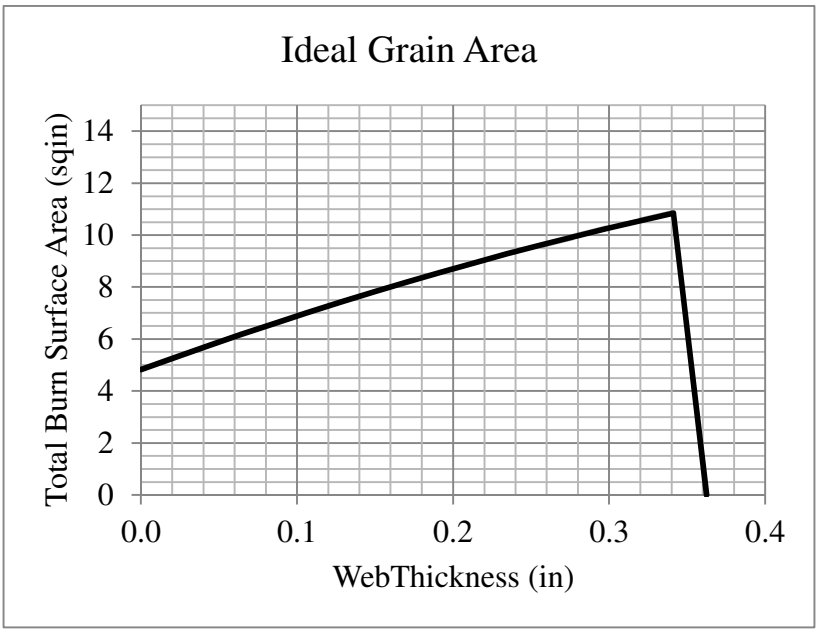

Figure B-2 Ideal Web versus Surface Area for a G138 Propellant Grain

Although ideal web versus area is initially a good assumption in a ballistics model, there are occasions when this relationship can actually be derived from test data. Coincidentally, a G138 motor was tested in Spring 2014 with a copper nozzle. The thrust divided by pressure plot revealed there was no throat erosion. Because the throat area is constant during operation, the copper nozzle test is a good candidate for backing out surface area as a function of web thickness. Recall the steady state chamber pressure equation:

$$\frac{A_b}{A_t} = \frac{P_c^{(1-n)}}{c^* \rho a_0 e^{\sigma_p (T_f - T_0)}} \qquad \textbf{(B-3)}$$

Given a set of test data with no throat erosion, the throat area (A_t) in Equation (B-3) can simply be moved to the right-hand side with the other known quantities in this problem. The propellant burn rate is integrated over time (from 10% of maximum pressure to the end of burn) to calculate the web thickness. There are a couple of ways to define the end of burn. For this analysis, a mass balance method was used: the end of burn is defined as the point at which accumulated propellant mass is within 1% of actual mass. This is sufficient because the effluent mass flow out of the motor after burnout is quite small. Figure B-3 shows the results for the empirically-derived web versus area relationship. The ideal relationship is also provided for reference. The ballistics model is updated with the empirical web versus area lookup table.

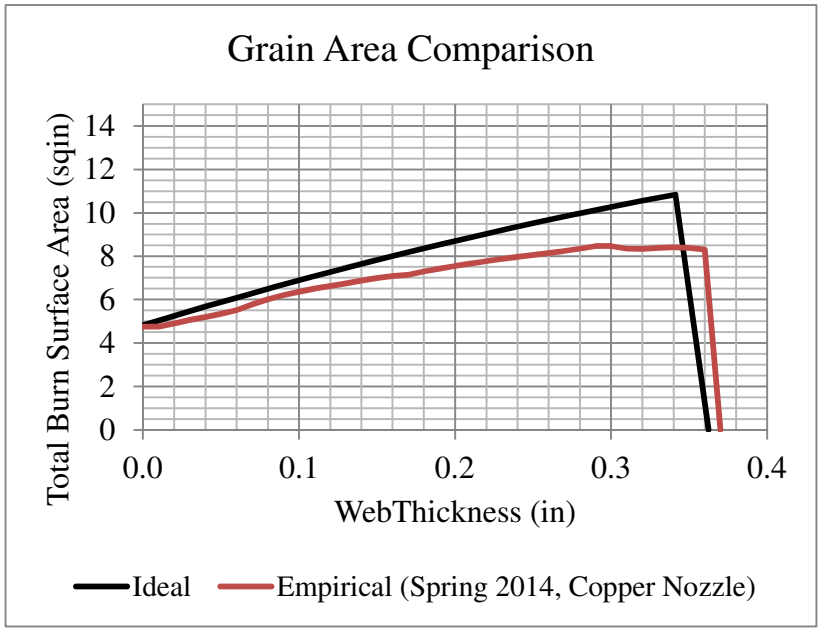

Figure B-3 Compare Ideal and Empirical Web versus Area

Appendix C

Calibration Standard

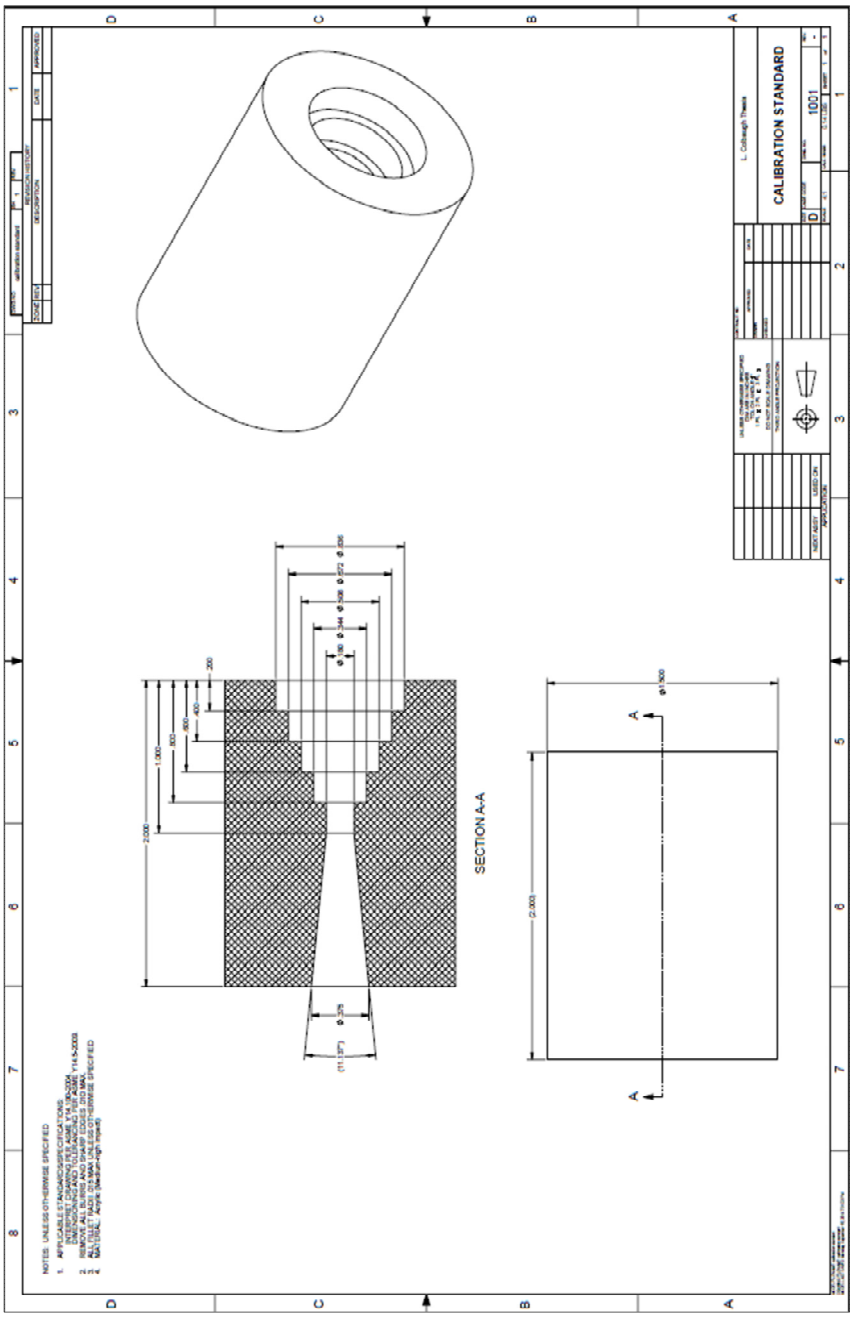
CALIBRATION STANDARD
1001
SECTION A-A

Appendix D

Linear Attenuation Coefficients

References for linear attenuation coefficients can be found in [29] for air and [30] for acrylic.

Air	LAC
(kV)	(1/in)
10	1.57E-02
15	4.94E-03
20	2.38E-03
30	1.08E-03
40	7.60E-04
50	6.36E-04
60	5.73E-04
80	5.08E-04
100	4.71E-04
150	4.15E-04
200	3.77E-04
300	3.26E-04

Plexiglass (Acrylic)	LAC
(kV)	(1/in)
150	4.32E-01
200	4.06E-01
300	3.56E-01
400	3.17E-01
500	2.79E-01
600	2.67E-01
800	2.29E-01
1000	2.03E-01

Appendix E

Average Pixel Value

Frame 505 from dynamic Test 1, taken at 50 kV, was selected for APV analysis. It corresponds to an actual diameter of 0.324 inches in the calibration standard. Refer to Figure 3-27 for a screen shot of Frame 505. It was selected because the edge detection method selected a narrower edge than what the human eye might select in this frame (refer to Table 3-10). For the analysis, Frame 505 was divided by multiple values of APV to see how the normalized curve changed. Figure E-5 is provided here for reference (APV of 179 was used in the analysis in Chapter 3.) It is important to note that as APV increases the intensity or gray value becomes more white (e.g. white has AVP = 256). Figure E-10 clearly illustrates the sensitivity of measured diameter as a function of average pixel value.

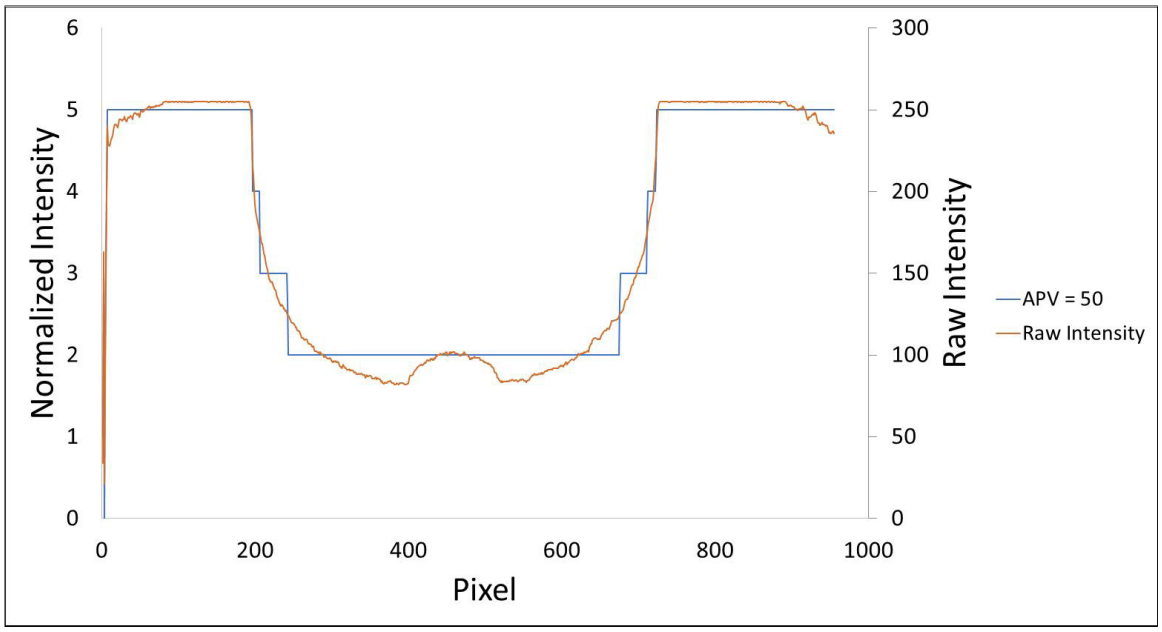

Figure E-1 Dynamic Test 1, Frame 505, APV = 50

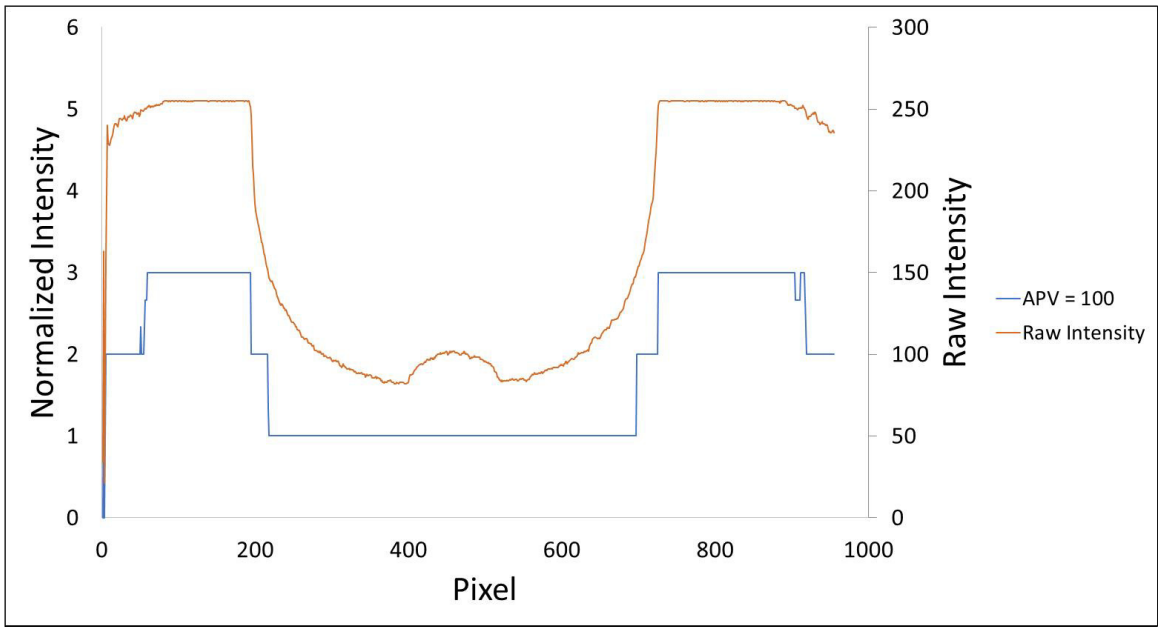

Figure E-2 Dynamic Test 1, Frame 505, APV = 100

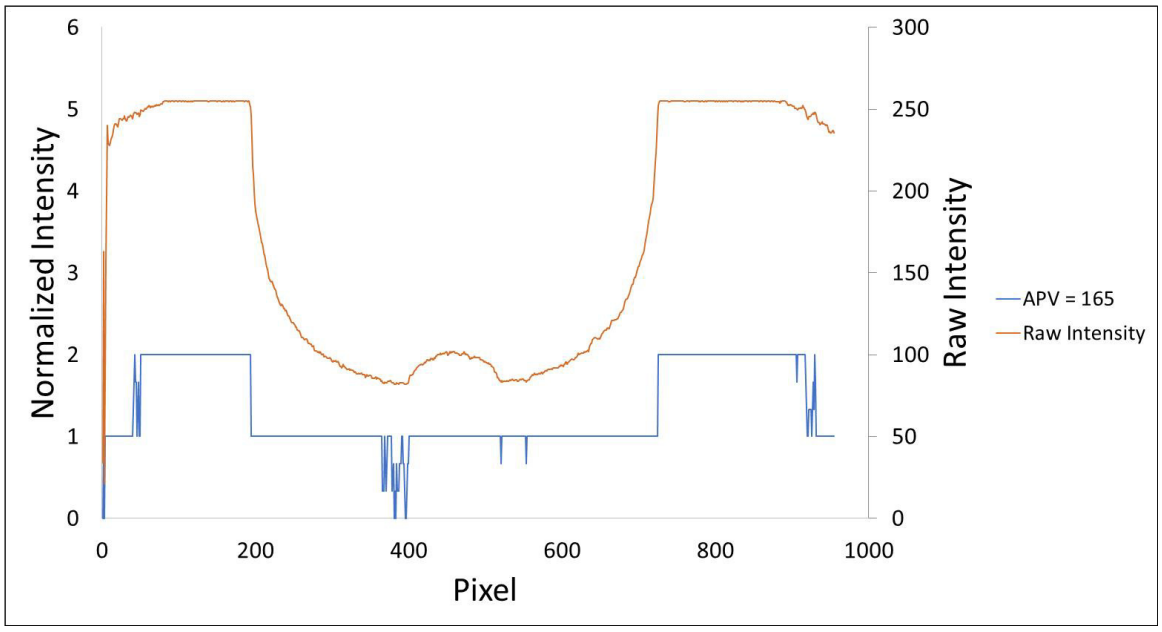

Figure E-3 Dynamic Test 1, Frame 505, APV = 165

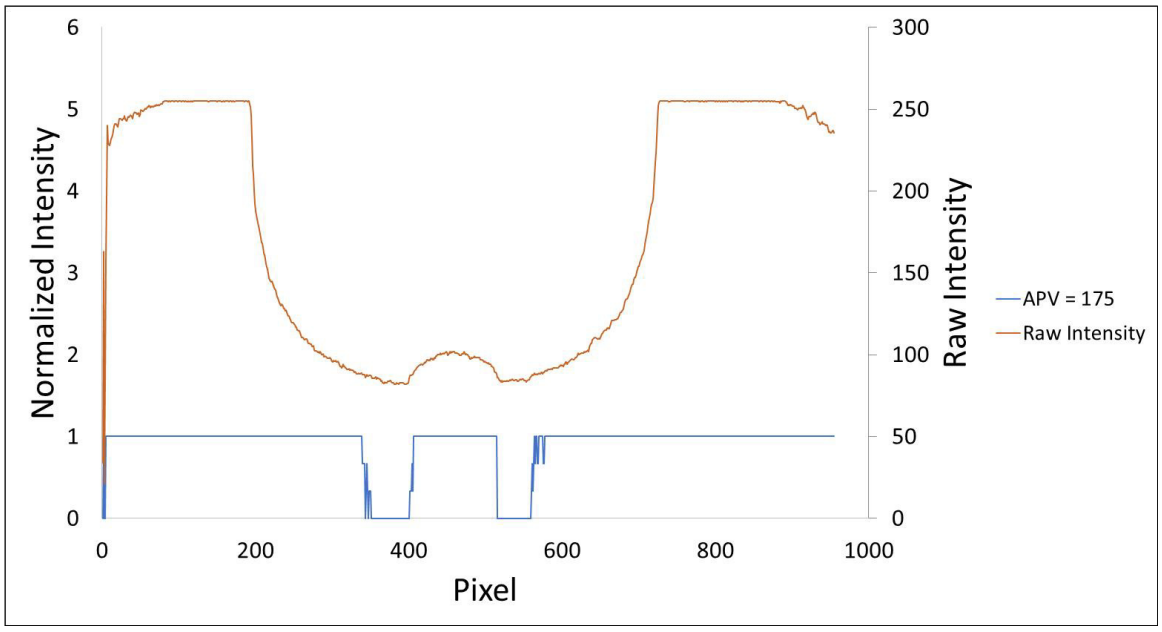

Figure E-4 Dynamic Test 1, Frame 505, APV = 175

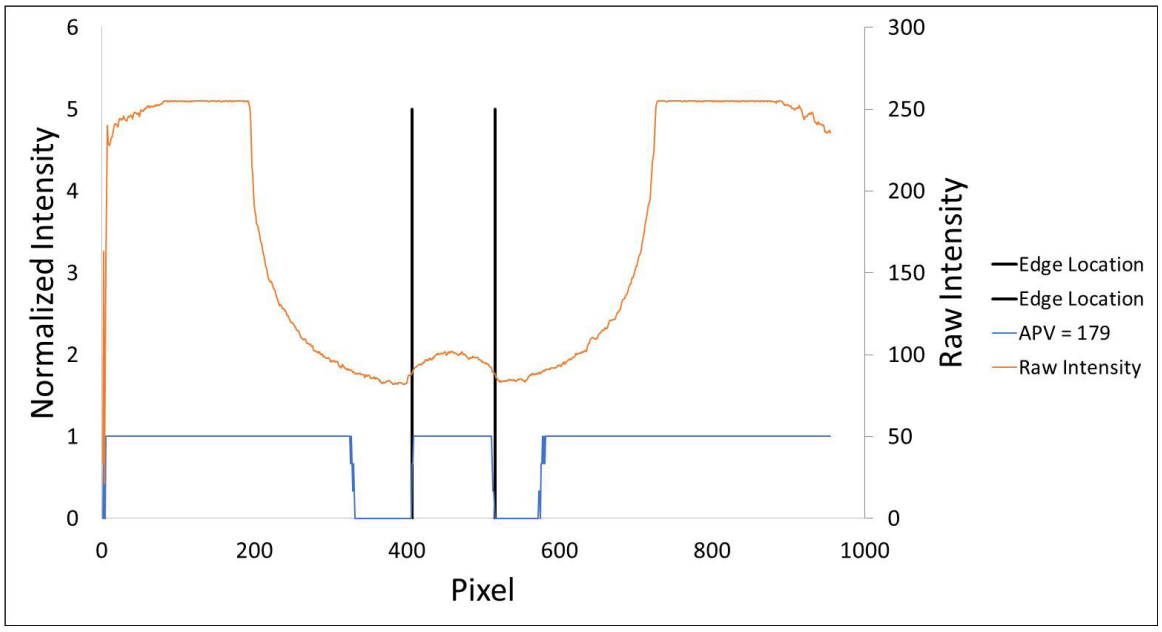

Figure E-5 Dynamic Test 1, Frame 505, APV = 179

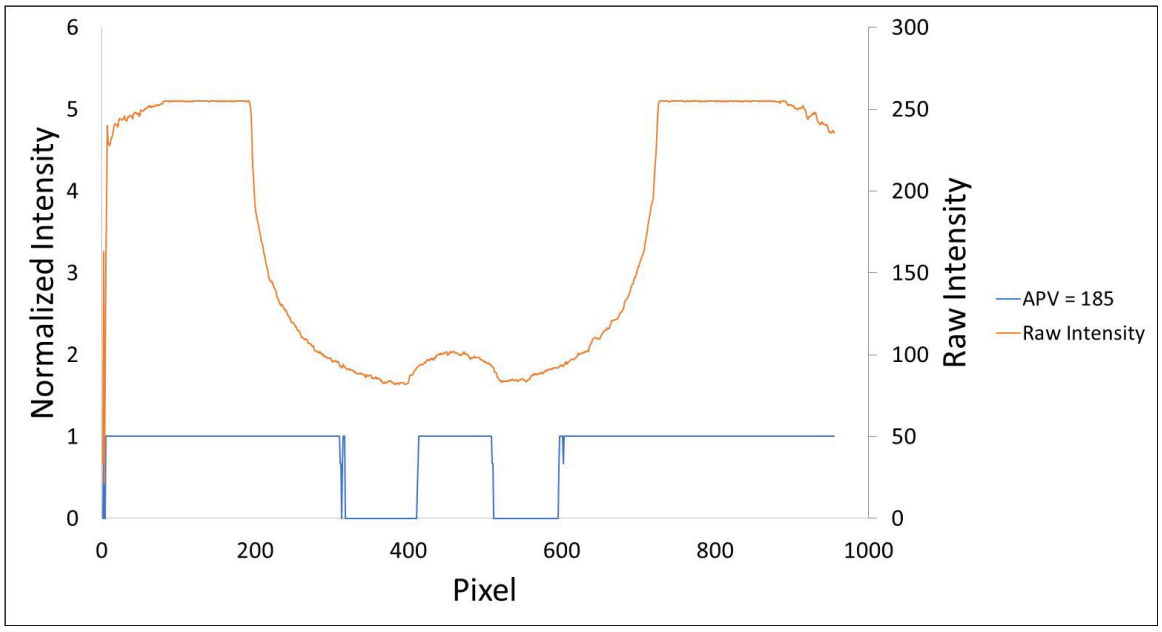

Figure E-6 Dynamic Test 1, Frame 505, APV = 185

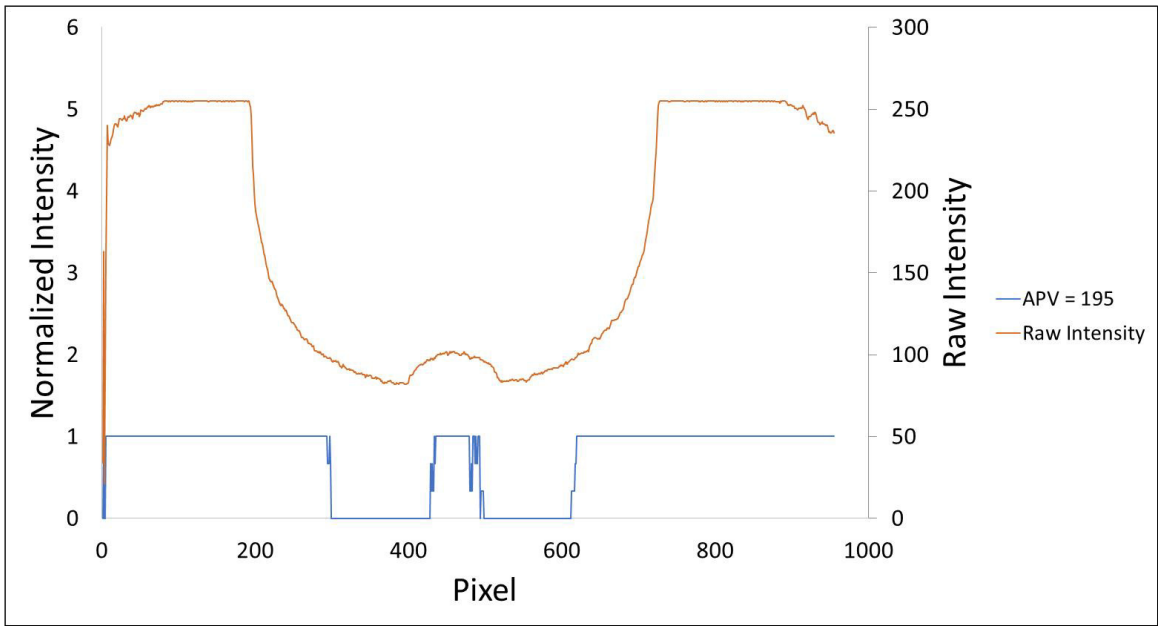

Figure E-7 Dynamic Test 1, Frame 505, APV = 195

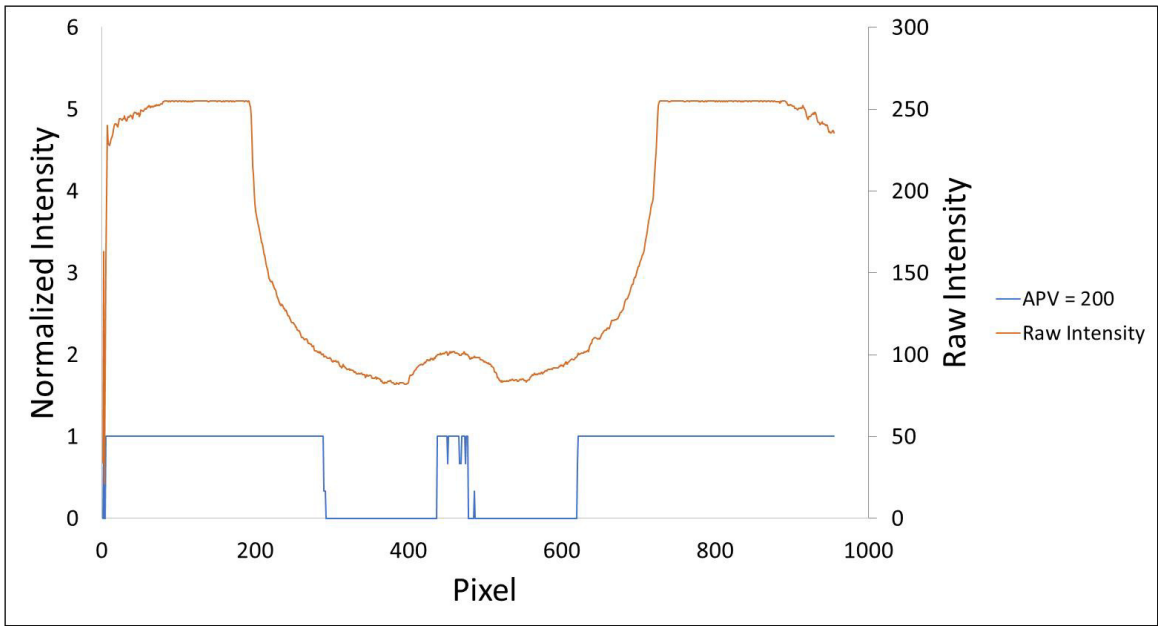

Figure E-8 Dynamic Test 1, Frame 505, APV = 200

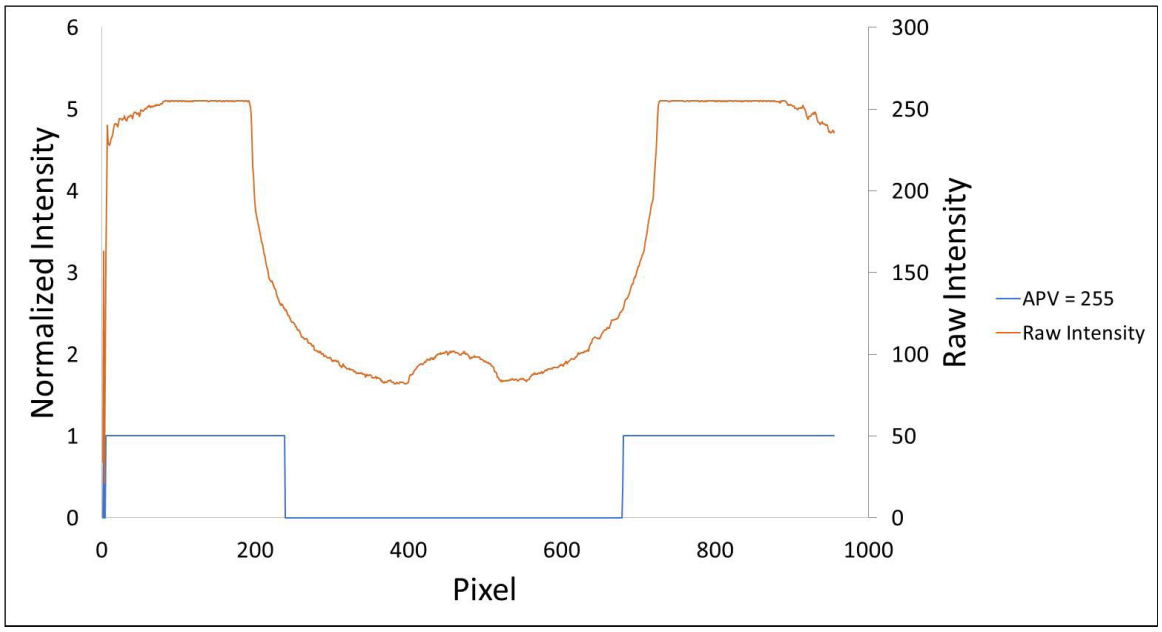

Figure E-9 Dynamic Test 1, Frame 505, APV = 255

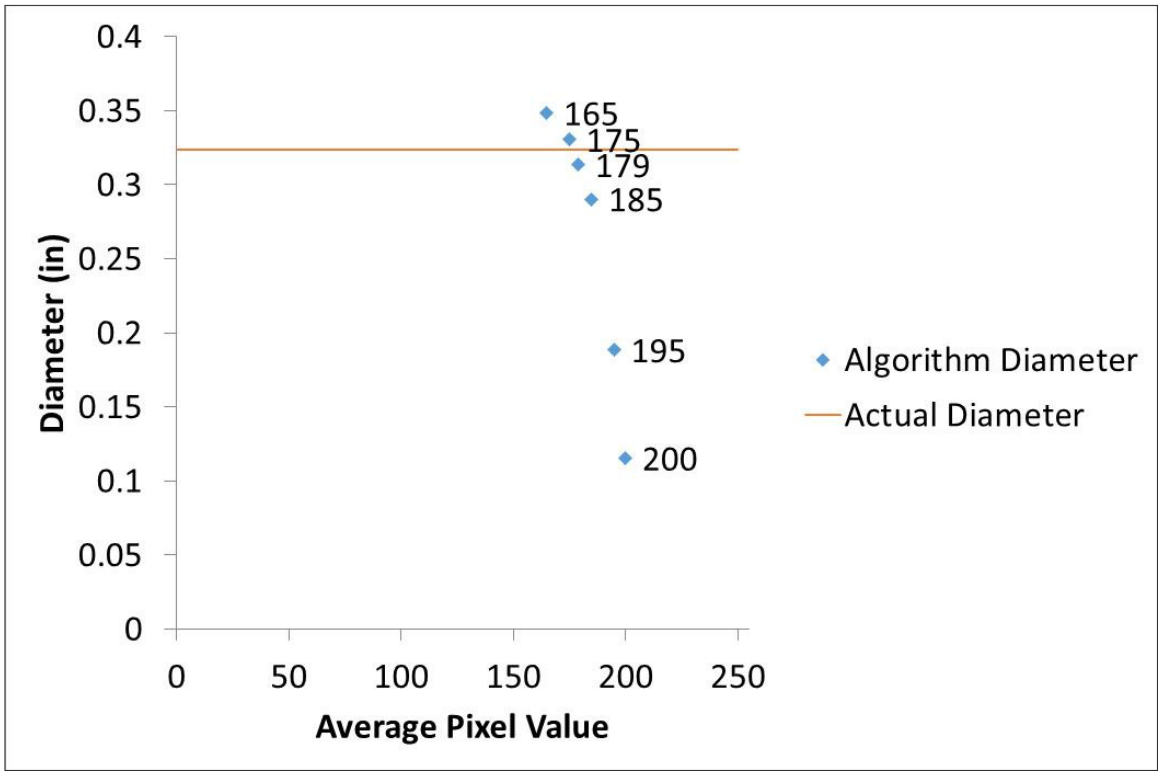

Figure E-10 Diameter as a Function of Average Pixel Value

REFERENCES

[1] Klager, K. "The Interaction of the Efflux of Solid Propellants with Nozzle Materials." *Propellants, Explosives, Pyrotechnics* 2.3 (1977): 55-63. Web.

[2] Thakre, Piyush, and Vigor Yang. "Chemical Erosion of Carbon–Carbon/Graphite Nozzles in Solid-Propellant Rocket Motors." *Journal of Propulsion and Power* 24.4 (2008): 822-33. Web.

[3] Evans, Brian, and Kenneth Kuo. "Nozzle Erosion Characterization in a Non-Metallized Solid-Propellant Rocket Motor Simulator." *International Journal of Energetic Materials and Chemical Propulsion* 7.3 (2008): 209-22. Web. 18 Sept. 2014.

[4] Fitzer, Erich, and L. M. Manocha. *Carbon Reinforcements and Carbon /carbon Composites*. Berlin: Springer-Verlag, 1998. Print.

[5] Nasuti, Francesco, and Daniele Bianchi. "Carbon-Carbon Nozzle Erosion and Shape-Change Effects in Full-Scale Solid-Rocket Motors." *Journal of Propulsion and Power* 28.4 (2012): 820-30. Web.

[6] Chankapoe, Suwicha, Nattawat Winya, and Narupon Pittayaprasertkul. "Performance Investigation of Solid-Rocket Motor with Nozzle Throat Erosion." *World Academy of Science, Engineering and Technology* 81 (2013). Web. 18 Sept. 2014.

[7] Jensen, Mikael, and Jens Wilhjelm. *X-ray Imaging: Fundamentals and Planar Imaging*. PDF.

[8] Menke, Doug. "Properties of X-rays." California, Stanford. 30 Oct. 2013. Web. <http://web.stanford.edu/group/glam/xlab/MatSci162_172/LectureNotes/01_Properties%20&%20Safety.pdf>.

[9] Ravindran, V. R., C. Sreelakshmi, and S. Vibinkumar. "Digital Radiography-based 3D-CT Imaging for the NDE of Solid Rocket Propellant Systems." *Insight - Non-Destructive Testing and Condition Monitoring* 50.10 (2008): 564-68. Web.

[10] Abdullah, J., and S.M. Sipaun. "Development of an X-ray Computed Tomography System for Non-Invasive Imaging of I." American Institute of Physics. Web. 19 Nov. 2014.

[11] Duliu, Octavian. "How Sensitive Is CAT to Porosity?" Journal of Trace and Microprobe Techniques, Vol. 21, No. 4, Pp. 609-614, 2003. Web. 19 Nov. 2014.

[12] Zamora, David. "Basic Concepts in Radiography: Geometry, Contrast, Scatter." *UW Imaging Physics Course*. Web. 18 Sept. 2014. <http://courses.washington.edu/radxphys/r2.html>.

[13] Ghose, Bikash, and D.k. Kankane. "Estimation of Location of Defects in Propellant Grain by X-ray Radiography." *NDT & E International* 41.2 (2008): 125-28. Web.

[14] Ravindran, V.R. *Development of CT and 3D-CT Using Flat Panel Detector Based Real-Time Digital Radiography System*. American Institute of Physics, 2008.

[15] Püskülcü, G., and A. Ulas. "3-D Grain Burnback Analysis of Solid Propellant Rocket Motors: Part 1 – Ballistic Motor Tests." *Aerospace Science and Technology* 12.8 (2008): 579-84. Web.

[16] Perceptics Corporation. *High-Resolution Three-Dimensional Computed Tomography*. Rep. no. WL-TR-96-4117. 1996. Wright-Patterson Air Force Base. Web. 29 Aug. 2013.

[17] Ghose, B., and S. N. Singh. "Digital Imaging System for Linac X-rays for NDE of Case Bonded Solid Rocket Motors." *Insight - Non-Destructive Testing and Condition Monitoring* 50.3 (2008): 124-26. Web. 20 Nov. 2014.

[18] Rogerson, D.J. "Dynamic Real-time Radiography of Solid-propellant Rocket Motors during Static Firing." *NDT International* 22.2 (1989). Web.

[19] Frederick, R. A., S. B. Farmer, and B. M. Williams. "Predicting and Analyzing X-rays to Measure Propellant Crack Propagation Speed." *Journal of Propulsion and Power* 12.2 (1996): 310-14. Web.

[20] Xiao, Yumin, R. S. Amano, Timin Cai, and Jiang Li. "New Method to Determine the Velocities of Particles on a Solid Propellant Surface in a Solid Rocket Motor." *Journal of Heat Transfer* 127.9 (2005): 1057-061. Web.

[21] Frederick, Robert A., Jr., James A. Nichols, and Jon Rogerson. "Slag Accumulation and Slosh Measurements with Real-Time Radioscopy." Journal of Flow Visualization & Image Processing 3 (1996): 165-76. Web.

[22] Evans, Brian, Kenneth Kuo, Eric Boyd, and Andrew Cortopassi. *Comparison of Nozzle Throat Erosion Behavior in a Solid-Propellant Rocket Motor and a Simulator*. Proc. of 45th AIAA/ASME/SAE/ASEE Joint Propulsion Conference & Exhibit, Colorado, Denver. Vol. AIAA 2009-5421. Print.

[23] Frederick, R. A., B. M. Williams, J. C. Bain, and J. A. Nichols. "Predicting X-ray Images for Burning Solid-Propellant Rocket Motors." *AIAA* (1991). Web.

[24] Ravindran, V.R., C. Sreelekshmi, and V.P. Mahadevan Pillai. "Mathematical Modelling of the X-ray Image of Solid Rocket Motor for Quantitative Analysis." Insight Vol 48 No 1 January 2006. Web. 20 Nov. 2014.

[25] P. Karthikeyan, V.k. Ravindran, Abilash, S. Hari Krishna, N. Narayanankutty, K.m. Usha, S. Rakesh. "Prediction Of Erosion Characteristics For Ablative Throat Insert Liners Using Ultrasonic Velocity Measurements." *Proceedings of the National Seminar & Exhibition on Non-Destructive Evaluation* (2011): 167-70. Web. 20 Nov. 2014.

[26] Jones, Dan, Jason Budinoff, and Robert Sorrell. *Appendix A - G-138 Motor Description and Test Data*. Rep. Huntsville: University of Alabama in Huntsville, 2014. Print.

[27] Aerotech Division. *HP-G138T-14A Assembly Drawing and Instructions*. PDF.

[28] Sutton, George Paul., and Oscar Biblarz. *Rocket Propulsion Elements*. New York: John Wiley & Sons, 2001. Print.

[29] Hubbell, J.H., and S.M. Seltzer. "Tables of X-Ray Mass Attenuation Coefficients and Mass Energy-Absorption Coefficients (version 1.4)." NISTIR 5632. National Institute of Standards and Technology, 12 July 2004. Web. 24 Aug. 2014.

[30] Cesareo, Roberto, and Antonio Brunetti. *X and Gamma Ray Tomography for Non Destructive Material Testing*. Proc. of SPIE Conference on Developments in X-Ray Tomography II, Colorado, Denver. Vol. 3772. 292-303. Print.